

Fabrication of Low-Absorption Diamond Lenses for Focusing Hard X-Rays at Synchrotron Sources

S. R. Whittaker

Chemical Physics MSci Final Year Thesis

Academic Year: 2011/2012

Supervisor: Professor Paul May

Number of Words: 25,641



University of
BRISTOL

Acknowledgements

I would like to thank my supervisor, Professor Paul May, along with my primary assessor Dr. Neil Fox and second assessor Professor Michael Ashfold.

Special thanks are given to Dr. Oliver Fox for all the valuable advice, guidance and for making the project so enjoyable.

Thank you to the entire Bristol Diamond Group for being such a supportive group with which to work.

Declaration

The work in this thesis is in conjunction with a post doctorate, Dr. Oliver Fox. I am fully trained on the micro-wave assisted chemical vapour deposition reactor, and carried out most of the depositions. However due to each deposition running over at least two days, monitoring of the reactor was often shared between the two of us. I took all the Raman spectra for each sample and fitted them using the *fityk* graph-fitting program. To work out the growth rates of the diamond films and assess the filling of the lens moulds, cross-sectional scanning electron microscope (SEM) images were taken, and the thickness of each region measured. I prepared the cross-sections by using a laser micromachining system (Oxford Lasers Alpha 532 System). There are two SEMs in the School of Chemistry, a JEOL JSM 5600 LV instrument and a JEOL JSM 6330 F instrument, of which I am trained on the former. When the 5600 LV was available I would take the SEM images, and in the cases where only the 6330 F was available Oliver would take the images. I made up the solutions for the polymeric self-assembly method in **Section 6.2.4**.

Table of Contents

Abstract.....	v
1. Hard X-Rays.....	1
1.1. Synchrotron Sources.....	1
1.2. Focusing using Reflective of Diffraction.....	2
1.3. Focusing using Refraction.....	3
1.3.1. Compound Refractive Lenses.....	4
1.3.2. Kinoform Lenses.....	4
2. Diamond.....	7
2.1. High Pressure High Temperature Diamond.....	8
3. Chemical Vapour Deposition.....	9
3.1. Types of CVD Reactor.....	9
3.1.1. Hot Filament Reactor.....	10
3.1.2. Micro Plasma-assisted Reactor.....	11
3.1.3. Other Types of CVD Reactor.....	11
3.2. Chemistry of CVD Diamond.....	12
3.2.1. The Role of Atomic Hydrogen.....	12
3.2.2. The Mechanism.....	13
3.3. Types of Synthetic Diamond.....	14
3.3.1. Microcrystalline Diamond.....	14
3.3.2. Nanocrystalline Diamond.....	15
3.3.3. Ultrananocrystalline Diamond.....	16
3.4. Nanocrystalline Diamond by CVD.....	16
3.4.1. Methane Concentration.....	17
3.4.2. Argon-Rich Plasma.....	17
3.4.3. Nitrogen Addition.....	17
4. Fabrication of Diamond Refractive Lenses.....	19
4.1. Etching Polycrystalline Diamond.....	19
4.2. Using MWCVD.....	21
5. Experimental Method.....	25
5.1. MWCVD Reactor.....	25
5.2. Controlling the Gas-Flow.....	26
5.3. Nucleation of the Sample.....	26
5.3.1. Ultrasonic Probe Nucleation.....	27
5.3.2. Electrospray Method.....	27
5.4. Spectroscopic Analysis of the Plasma.....	28

5.4.1. Optical Emission Spectroscopy.....	28
5.5. Characterisation of Diamond Films.....	29
5.5.1. Raman Spectroscopy.....	29
5.5.2. Optical Microscopy.....	33
5.5.3. Scanning Electron Microscopy.....	33
6. Results and Discussion.....	35
6.1. Nitrogen Addition and an Argon-Rich Plasma.....	36
6.1.1. Laser Raman Spectra.....	38
6.1.2. Growth Rate and Electron Microscopy.....	50
6.1.3. Optical Emission Studies of the Plasma.....	58
6.1.3.1. CN.....	59
6.1.3.2. C ₂	61
6.1.3.3. CH.....	63
6.1.3.4. H.....	64
6.2. Preferential Nucleation.....	65
6.2.1. Manual Removal of Nucleation Layer.....	65
6.2.2. Polymer Resist Coated Silicon Moulds.....	67
6.2.3. Oxide Coated Silicon Moulds.....	78
6.2.4. Electrostatic Self-Assembly Nucleation.....	84
6.2.5. Comparison of Successful Nucleation Methods.....	88
7. Future and Outlook.....	91
8. Conclusions.....	93
References.....	94
Certificate of Ownership.....	97

Abstract

Silicon reflective mirrors are currently used to focus hard x-rays produced at the Diamond Light Source (DLS) synchrotron facility. While these are able to focus the beam to ~ 200 nm, the advances in science now demand hard x-rays to be focused to < 100 nm focal spot size. The experimental setup for silicon reflective mirrors is very sensitive and the equipment is both large and expensive to run.

A solution is to replace the silicon reflective mirrors with refractive lenses made of diamond. By using refractive optics the focusing apparatus is of a more practical size and using diamond makes for a more efficient lens due to lower x-ray absorption.

The collaboration between DLS, Micro- and Nanotechnology Centre (MNTC) and the School of Chemistry, University of Bristol has created a method for fabricating low-absorption diamond refractive lenses. Nanocrystalline diamond is deposited onto a silicon lens mould using microwave plasma-assisted chemical vapour deposition. The silicon mould is then etched away from the deposited diamond to leave a free-standing diamond lens.

The practical work of this thesis is based around optimising the diamond deposition procedure and falls into two sections. Firstly the effect of nitrogen addition to the process gas mixture on both the morphology of the diamond film and the filling of the lens moulds is investigated. Secondly, novel nucleation methods are trialled in order to encourage diamond deposition into the lower regions of the lens moulds, and reduce the deposition rate on to the top surface. The preferential deposition onto the lower surface of the lens moulds is crucial for reducing the focal-width and increasing the lens efficiency.

1. Hard X-Rays

X-rays form a high energy (E) region within the electromagnetic radiation spectrum spanning $\sim 1 - 120$ keV (corresponding to wavelengths, $\lambda = 12.4 - 0.1$ Å).^[1] They were discovered in 1895 by Röntgen,^[2] and have since been exploited and used in a wide range of applications spanning medical imaging, crystallography, and a variety of spectroscopic techniques. Of particular interest to the condensed matter physics and materials science community are hard x-rays, where $E > 4$ keV. This is because hard x-rays are extremely penetrating and as such can be used to probe the internal structure of materials. Hard x-rays could be used as a probe in scanning microscopy,^[3] and in combination with tomography, allow construction of an image of the internal structure of a material in 3-dimensions. Hard x-rays also have uses in microscopic imaging in, for example, fluorescence analysis and absorption spectroscopy. This would enable structural knowledge to be determined down to the atomic scale as well as chemical information of specific elements within it.^[3]

In order to use hard x-rays in this manner, it is essential to generate a beam that is diametrically small and very intense. The high intensity of the x-rays is achieved by producing them at synchrotron sources (**Section 1.1**). In order to produce a diametrically small beam, these synchrotron x-rays require focusing, of which a range of optical techniques are currently available (**Sections 1.2 and 1.3**).

1.1 Synchrotron Sources

A synchrotron (**Figure 1**) is a large machine that uses a series of particle accelerators to produce high-intensity electromagnetic radiation ranging from x-rays through ultra-violet to far infra-red. Electrons are generated at the electron gun *via* thermionic emission and subsequently accelerated up to speeds nearing the speed of light by passing through a series of three particle accelerators; a linear accelerator (linac), the booster synchrotron, and finally, the large storage ring. After entering the booster synchrotron the electrons will complete a series of circuits until they reach an appropriate energy whereby they are fed out into the large storage ring. The large storage ring is comprised of a series of straight sections that are angled together to form a continuous circuit. Bending magnets are used to guide the electrons around the circuit. Upon passing through a bending magnet, an electron will lose energy in the form of electromagnetic radiation. It is this electromagnetic radiation that is channelled out of the large storage ring into “experimental beamlines”. After exiting the large storage ring, the beamline passes into an “optics hutch”, where the beam is collimated, focused and made monochromatic before becoming incident onto the investigated sample which is situated in the “experimental station”.

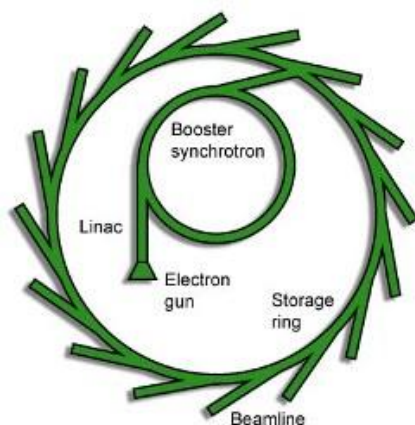


Figure 1: Schematic of a synchrotron with the three particle accelerators labelled (www.diamond.ac.uk).

Currently at DLS, and other synchrotron facilities, the x-rays are focused by bimorph, bent silicon mirrors using a grazing angle of incidence. These mirrors have to be extremely high quality, are ~ 1 m in length and need to be kept under constant vacuum. Therefore, they are expensive to run, need incredibly precise apertures and are not very space-efficient. One of the motives for producing refractive (or diffractive-refractive) lenses comes from replacing the current reflective silicon optics with smaller, cheaper lenses that have simpler setup and apertures that do not have to be so precise.

One of the current aims in synchrotron optics is to be able to focus the x-ray beams down to nanometre focal-spot sizes. Advances in science and technology drive the desire for high spatial resolution on the atomic scale. In order to allow for this, the focal-spot needs to be of similar order to that which is being probed. Thus another motive for producing the refractive lenses is not to replace the current silicon optics, but to work in conjunction with them to reduce the focal-spot beyond what is currently capable when using the mirrors alone.

1.2 Focusing using Reflection of Diffraction

Technologies which use x-ray radiation have traditionally relied upon reflection and diffraction, as opposed to refraction, for focusing the radiation. This is because the refractive index of x-rays in most materials is exceedingly close to unity (see **Section 1.3**) and, hence, the resulting refraction on passing through these materials is minimal.^[4]

Reflective mirror pairs^[5, 6] and diffractive Fresnel zone plates^[7] (**Figure 2**) have been able to achieve sub-micron resolution of x-rays. The benefit of reflective mirror pairs is that the optics are free of chromatic aberrations and maintain efficiency close to one for a wide range of energies, however the drawback is that they are not practical for use in the laboratory because very large distances are required to focus the x-ray beam.^[8] The setup is

very sensitive because the shape of mirror-surface determines the focusing quality and an adjustment of one mirror by only a micron can result in the beam losing focus.^[6]

Fresnel zone plates focus directly to a point and have achieved the smallest focal point to date, however this is when using soft x-rays, as opposed to hard x-rays as required in this project.^[9] The focal spot size is determined by the smallest fabricated feature of the lens resulting in diffraction-limited focusing. The lens performance is highly affected by the aspect ratio (= length/width) of the lens. In order to focus an x-ray beam down to 50 nm, an aspect ratio of 20 would be necessary which is extremely challenging to realise.^[10]

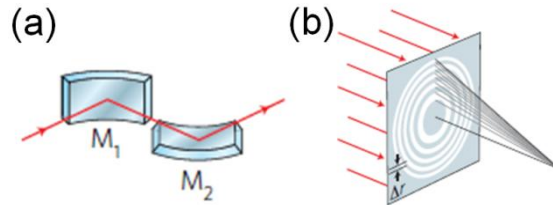


Figure 2: (a) Reflective mirror pair (b) Diffractive Fresnel zone plate. Images reproduced from 11.

1.3 Focusing using Refraction

As mentioned previously, the refractive index of x-rays is incredibly close to unity and this poses complications when using refractive optics to focus an x-ray beam. The complex refractive index of an arbitrary material is given by

$$n = 1 - \delta - i\beta \quad \text{Equation 1}$$

where δ and β are the refractive index decrement and the absorption index, respectively.^[12] They are both optical constants specific to a material and are dependent on the energy of incident radiation.^[12] For hard x-rays in all matter δ is very small ($\sim 10^{-6}$), explaining why n is ~ 1 , and it is also positive resulting in $n < 1$. The significance of having $n < 1$ is that a concave lens is required in order to focus x-rays, unlike visible light where $n > 1$ (**Figure 3**).

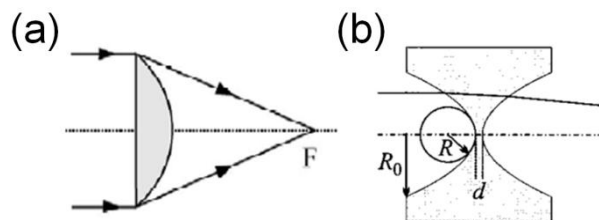


Figure 3: Diagram of two different types of a refractive single lens (a) Convex refractive lens, used when $n > 1$; image reproduced from reference 4 (b) Concave refractive lens, used when $n < 1$; image reproduced from reference 13.

As $n \sim 1$, a single lens is not sufficient to focus the x-ray beam within a practical focal length for laboratory use. By using the expression for the focal length (**Equation 2**) it

is clear that for a single lens the focal length, f , would be extremely large. R is the radius of curvature.

$$f = \frac{R}{2\delta} \quad \text{Equation 2}$$

In order to overcome this issue of minimal refraction, two refractive lens designs have been proposed for study as part of this project: a compound refractive lens (CRL) (**Section 1.3.1**) and a kinoform lens (**Section 1.3.2**).

1.3.1 Compound Refractive Lenses

A CRL consists of a series of convex lenses in an array where all the individual lens optical axes are coincident (**Figure 4**).^[14] While the refraction of x-rays from one single lens is small, by aligning a number of lenses, N , in series the focusing of the x-ray beam becomes practical. The focal length is decreased compared to that of a single lens, by a factor N , as shown by **Equation 3**:

$$f_{CRL} = \frac{R}{2N\delta} = \frac{f}{N} \quad \text{Equation 3}$$

Ideally, CRLs are comprised of parabolic or elliptical surfaces, to avoid spherical aberrations.^[13] The CRL design is comparatively simple making it advantageous in terms of fabrication and manufacture. However, the x-rays pass through a lot of material and thus the absorption can be quite high, resulting in a less efficient lens. This effect can be reduced by using materials known to have low atomic number and, therefore, absorption coefficients.

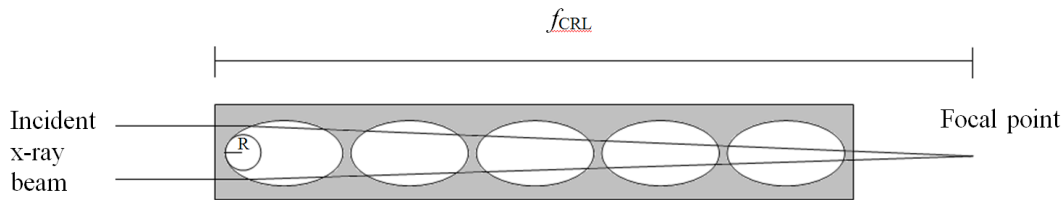


Figure 4: Schematic diagram showing the basic concept of a CRL lens ($N = 5$).

1.3.2 Kinoform Lenses

In a kinoform lens the x-ray radiation passes through a smaller amount of material resulting in less absorption and a greater beam intensity exiting the lens compared with the CRL structure. A kinoform structure comprises a parabolic or elliptical three-dimensional surface in which pairs of segments have been cut out (**Figure 5**).

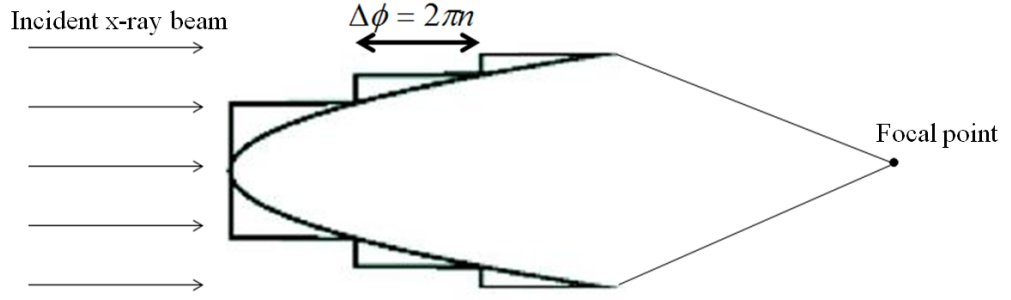


Figure 5: Schematic diagram of a kinoform lens with the passive material removed.

Fresnel's equations^[15] lead to the observation that as the wavelength tends to zero ($\lambda \rightarrow 0$), only the lens curvature is responsible for focusing an incident beam.^[12] Since hard x-rays are of such high energy, they fit this criterion. When x-rays travel a distance, x , through the lens material a phase difference arises:

$$\text{phase difference} = \frac{2\pi\delta x}{\lambda} \quad \text{Equation 4}$$

If material responsible for causing a 2π phase shift is removed, while maintaining the parabolic lens surface shape, the lens performance should not be compromised. This material is termed "passive" and corresponds to a cut-out segment length that is proportional to λ/δ .^[12] When this extraneous material is removed the absorption of radiation within the lens structure can be significantly reduced.

As well as the lens design, the choice of material is of importance. X-rays are highly absorbed in most materials, due to their strong interaction with electrons. The absorption of an x-ray is proportional to $Z^4\rho$, where Z is the atomic number and ρ the material density.^[16] As such, the lenses are ideally constructed from materials with a low atomic number in order to reduce absorption and enable formation of a high-intensity focused beam. Due to the high energy associated with hard x-rays, it is also important that the lens-material is thermally stable so that it does not deteriorate during its lifetime while exposed to the radiation. Not only does diamond have a low atomic number ($Z = 6$) but it is also thermally very stable. Diamond is an impressive material that has a plethora of further properties and as such will be the material of choice in this project. The following two sections (**Sections 2 and 3**) are devoted to the properties and methods for producing synthetic diamond.

2. Diamond

Diamond is a material that has attracted keen interest and has been widely studied for centuries. Despite being most well known for its exceptional gemmological beauty and value, diamond has such an impressive array of properties that it has found its way into many technological applications. Diamond is the hardest known material, it has the highest room temperature thermal conductivity, a low thermal expansion coefficient, and an optical transparency band that is wider than any other solid.^[17] The remarkable properties extend further; diamond has the highest sound propagation velocity, is resistant to corrosion, is a good electrical insulator yet can behave as a semiconductor when doped appropriately, and is extremely rare in that its electron affinity is negative. Diamond is also wear resistant, has the highest bulk modulus yet the lowest compressibility.^[17, 18] Despite such diverse properties, for a long while it was very difficult to actually exploit these properties and realise the potential applications using diamond. This was not only due to the required fabrication techniques, but actually sourcing natural diamonds was challenging due to their rarity and value. The majority of natural diamonds are flawed meaning that even if diamond was successfully sourced, it was often not of high enough quality to make practical use of the stone.

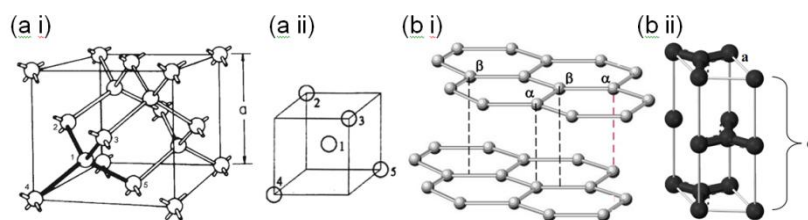


Figure 6: (a i) Cubic unit cell of diamond lattice showing the tetrahedral arrangement of carbon atoms (a ii) Mapping the tetrahedral arrangement of carbon atoms 1-5 onto a cube. Images reproduced from reference 19. (b i) 3-dimensional perspective of graphite. α atoms occur on every plane, β atoms occur on alternate planes (b ii) Graphite unit cell. 'a' and 'c' are lattice constants. Images reproduced from reference 20.

Diamond is solely made up of carbon atoms in a tetrahedrally arranged lattice (**Figure 6a**), such that each carbon atom is sp^3 -hybridised and covalently bonded to four neighbouring carbon atoms. Other than diamond, the most common material based solely on carbon is graphite (**Figure 6b**). Under standard room temperature and pressure, graphite is the thermodynamically stable allotrope. Despite only a small difference in their standard enthalpies of formation, the large activation barrier between the two allotropes means that conversion between diamond and graphite does not spontaneously occur without application of a large amount of energy.^[21] Diamond is *metastable* under these standard conditions, meaning that it is kinetically stable but thermodynamically unstable.^[18] Consequently, if

diamond is to be formed synthetically, a situation must be created whereby it is thermodynamically favoured over graphite. It was this observation that resulted in the development of the “high pressure, high temperature” (HPHT) method for synthesising diamond (**Section 2.1**). More recently, synthetic diamond has been produced controllably and successfully using chemical vapour deposition (CVD) (**Section 3**). CVD was used in this project to fabricate the diamond refractive lenses.

2.1 High Pressure High Temperature Diamond

In nature, diamonds are formed deep within the Earth’s mantle under extremely high pressures and temperatures. In 1892, Henri Moissan first raised the possibility of producing synthetic diamonds by re-creating the conditions in which natural diamonds are formed.^[22] This method has been refined and laboratory-grown diamonds are readily available for use in many industrial applications. The most commonly used HPHT method comprises a large hydraulic press which is either a four-anvil ‘tetrahedral press’ or a six anvil ‘cubic press’ responsible for creating the high pressure. A graphite ‘seed’ is placed within the growth chamber and converted into diamond by applying controlled heat and pressure in the presence of a catalyst. The phase diagram for carbon (**Figure 7**) shows that the conversion from graphite to diamond could hypothetically take place under less extreme conditions, however the time scales involved would be impractical. HPHT grown diamonds are frequently used in tools, drills and other industrial applications but are too flawed for use in gemmology and not pure enough for use in optics or electronics.^[23]

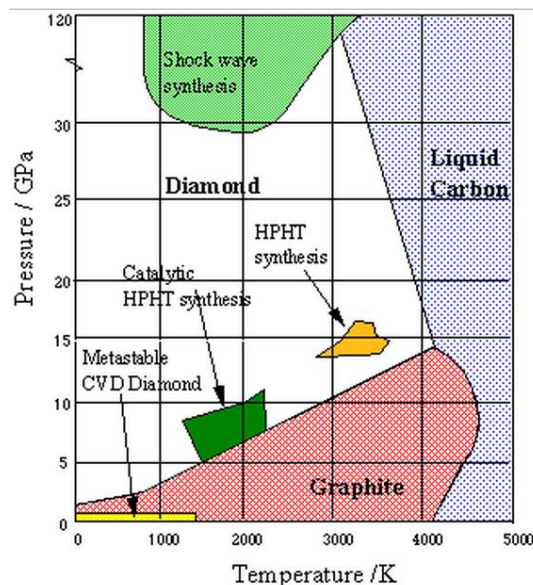


Figure 7: Phase Diagram for carbon. Reproduced from reference 21.

3. Chemical Vapour Deposition

If diamond were to be used in optics and electronics, much higher purity diamond was needed and a natural transition away from HPHT occurred. It should be noted that HPHT diamond remained a major source of industrial diamond for which lower purity diamond was acceptable (*cf.* **Section 2.1**). It was suggested that diamond could be synthesised in a controlled manner by building up a sp^3 -bonded tetrahedral network adding carbon atom-by-atom. The first attempt using this idea was by Eversole at the Union Carbide Corporation in 1958 when carbon-containing gases, under reduced pressure and at 900°C , were allowed to thermally decompose onto a crystal of natural diamond.^[24] This demonstration founded a renewed interest in synthetic diamond, although the method was far from perfect. It was extremely slow and the deposited material was composed of both diamond and graphite. An improvement to this method arose about a decade later by Angus *et al.* at Case Western Reserve University in who discovered that when atomic hydrogen was present during the deposition, graphite was preferentially etched over diamond, enabling the deposition of much purer diamond samples.^[25, 26] The first deposition on non-diamond substrates was demonstrated shortly after this in late 1970.^[27] The true birth of CVD was in 1982 when a hot-filament (HF) reactor was constructed by Matsumoto *et al.* at the National Institute for Research in Inorganic Materials (NIRIM) in Japan.^[28, 29] This CVD reactor was able to grow high purity diamond at relatively high growth rates onto non-diamond substrates. A year later, this same team developed the first microwave (MW) activated reactor.^[30, 31] The successes of this research team initiated worldwide interest and showed great promise for formation of synthetic diamonds. Diamond grown by CVD is now found in wide range of applications, and is still a very active area of research.^[32]

3.1 Types of CVD Reactor

CVD involves a gas-phase chemical reaction taking place above a solid surface resulting in deposition of material onto that surface. In order for these surface-reactions to occur, the gas-phase needs to be activated. This activation breaks the input gas into a mixture of molecules, ions and reactive radical species. In the CVD of diamond films, there are four main ways to activate the gas phase:^[18]

- i. Thermally, using a hot filament reactor (**Section 3.1.1**)
- ii. By electronic discharge, using a microwave plasma-assisted reactor (**Section 3.1.2**)
- iii. By a direct current or radio frequency plasma reactor (**Section 3.1.3**)
- iv. By a combustion flame, using an oxyacetylene torch (**Section 3.1.3**).

Of these activating methods, the hot filament and microwave-plasma methods are used most commonly due to them being reliable, reproducible and successful.

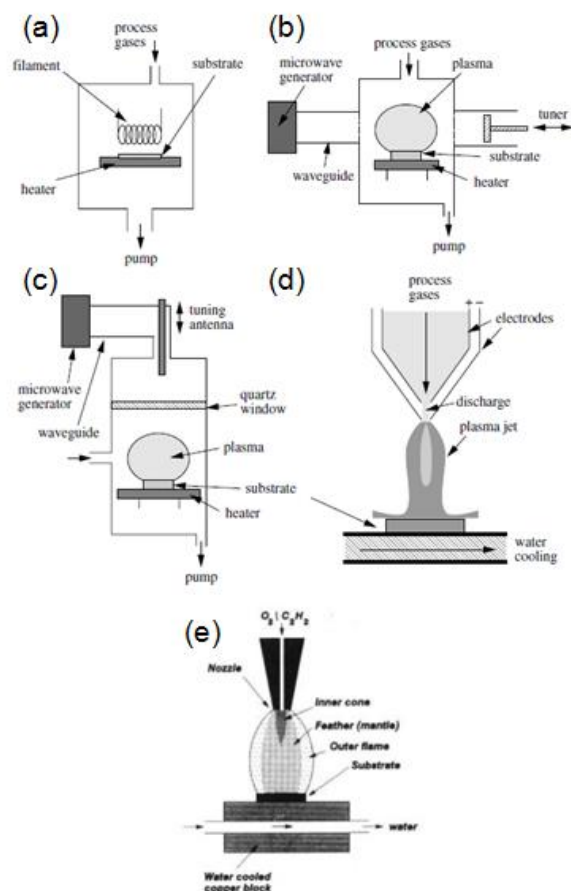


Figure 8: Common CVD reactors: (a) HF reactor (b) MW plasma reactor (NIRIM-type) (c) MW plasma reactor (ASTEX-type) (d) DC arc jet reactor (e) oxyacetylene torch. (a)-(d) are reproduced from reference 18, (e) is reproduced from reference 33.

3.1.1 Hot Filament Reactor

A HF reactor (**Figure 8a**) activates the gas-phase by resistively heating a filament to ~ 2200 °C. The substrate itself is heated to 700 - 900 °C within a vacuum chamber. Process gases are fed into the reactor at predetermined flow-rates. The pressure inside the reactor is maintained at 20 - 30 Torr. Depending on the deposition conditions, growth rates of 1 - 10 $\mu\text{m h}^{-1}$ can be achieved. The deposited diamond is typically polycrystalline and of reasonably high quality, however single crystal diamond can be obtained if diamond substrates are used (**Section 3.3**). The HF method is advantageous in that it is relatively inexpensive and its operation is straightforward. However, there are a few drawbacks including a limitation in the types of process gases that can be used, due to the filament being sensitive to oxidising or corrosive reagents, and that the diamond film often contains traces of the filament material. As a result the diamond produced is often not pure enough for use in some electronic applications.^[18]

3.1.2 Microwave Plasma-Assisted Reactor

Microwave plasma-assisted CVD reactors (MWCVD) have become the leading CVD method, despite the additional cost compared with the HF reactor setup. The principle of operation is not dissimilar to that of the HF reactor. Process gases are fed into a reaction chamber and a discharge is created by coupling microwave radiation with the gas *via* a dielectric window. Microwaves, emitted from an antenna at the top of the reactor cavity, couple energy into gas-phase electrons and subsequent collisions between these excited electrons and the gas molecules result in energy being transferred into the gas-phase. This differs to HF whereby the transfer of energy occurs due to thermally heating the process gas mixture. The collisions cause the gas molecules to gain energy and leads to dissociative pathways which form reactive species crucial to the diamond-depositing mechanism. **Figure 8b** and **Figure 8c** show schematics of the two most common MWCVD reactor setups.

The MWCVD method has some advantages over HF reactors including higher growth rates, resulting from a larger flux of growth species incident on the substrate, and higher quality, purer diamond due to the absence of a filament. The system is insensitive to oxidising or corrosive gases and thus diamond can be grown in a wide variety of process gas mixtures.

3.1.3 Other Types of CVD Reactor

Plasma jet reactors were developed in the 1980s. They function in a different manner to those using HF- or MW-systems and typically have higher flow rates. The jet of gas is passed through a high-power electrical discharge converting it into a mixture of ionised particles, molecules and radical species. The substrate is situated in a secondary chamber and the stream passes into this chamber at high velocity, striking the substrate surface. The most common type of plasma jet reactor is the direct current (DC) arc jet (**Figure 8d**). Plasma jets can also use radio frequency (RF) and MW plasma sources. The main advantage of these reactors is their ability to achieve growth rates in excess of $100 \mu\text{m h}^{-1}$.^[34, 35] This method does suffer some drawbacks: the growth area is limited to a very small region, and both the ignition and extinguishing of the jet thermally shocks the substrate. The latter is an issue if adherent coating of the substrate is desired, however if free-standing diamond films are ultimately required then this methods provides an easy, although not particularly controlled, way to disengage the diamond film from the substrate.

A simple version of the plasma jet method is the oxyacetylene torch or combustion flame method.^[36, 37] This method has advantages in that it is cheap and can be operated at atmospheric pressure, however it suffers the same disadvantages as any plasma jet setup.

3.2 Chemistry of Diamond CVD

In the following section the chemistry that underpins the complex mechanisms involved in the formation of diamond thin films by CVD is introduced.

The process gases are fed into the reaction chamber and diffuse towards the substrate surface. Before reaching the substrate, the gases pass through an activation region (*e.g.* the HF or the MW plasma). This region supplies energy to the gaseous species resulting in fragmentation into radicals, ions and electrons and heats the gases to ~ 3000 K.^[18] A large range of chemical reactions occur in the gas phase leading to a flux of carbon-containing growth species colliding with the substrate surface. Upon collision with the substrate surface, three possible outcomes arise:

- i. Immediate desorption or etching returning the species to the gas-phase;
- ii. Absorption and reaction between the colliding species and surface;
- iii. Diffusion in close proximity to the surface until a reactive site becomes available.

If either **(ii)** or **(iii)** occurs, providing other ambient conditions are suitable, diamond deposition can result. Recent research into diamond CVD has identified the specific conditions required for these gas-surface reactions to occur.^[38]

3.2.1 The role of Atomic Hydrogen

Atomic hydrogen is believed to be one of the most important species involved in diamond CVD. Most CVD of diamond is carried out with an excess of hydrogen gas to provide atomic H in a higher concentration than carbon-containing species. There are four main areas in which atomic hydrogen is influential:

- i. As mentioned in **Section 2**, the diamond lattice comprises sp^3 -bonded carbon atoms. However the lattice is finite with the surface terminated with a dangling bond. As the diamond is deposited, this dangling bond must be terminated in order to conserve the sp^3 arrangement and prevent formation of sp^2 -bonded structures. Atomic hydrogen acts to terminate the surface and maintain a stable lattice.
- ii. sp^2 -bonded carbon is etched by atomic hydrogen at a rate faster than the sp^3 -bonded carbon. The atomic hydrogen is thus able to remove any graphitic clusters from the growing surface and return them to the gas-phase environment.
- iii. A build up of long-chain or aromatic hydrocarbons in the gas-phase, would inhibit diamond growth by depositing onto the substrate surface and blocking any reactive sites. Atomic hydrogen reacts with these species, breaking up larger hydrocarbon molecules into smaller species.

- iv. By reacting with neutral species (*e.g.* CH₄), atomic hydrogen initiates the creation of the reactive radicals essential for diamond growth.

3.2.2 The Mechanism

The growth of diamond by CVD can be thought of as an atomic-hydrogen-catalysed reaction comprising of a step-wise addition of carbon atoms to a diamond lattice. While the exact process for diamond growth consists of other reactions, including direct insertion into bonds and surface migration, which can differ for each process condition, a simplified mechanism is shown in **Figure 9** and the following explanation describes the basic chemistry involved.

- i. The number of sites available for hydrocarbon absorption is limited due to the diamond surface being almost fully saturated with hydrogen. Atomic hydrogen diffuses to the surface and abstracts a surface-hydrogen creating a reactive site (**Figure 9a**).
- ii. In most cases this reactive site will react with another gas-phase atomic hydrogen and return to the situation in **i**. However, it is possible that a CH₃ radical from the gas-phase can strike the reactive site instead, resulting in a carbon atom being added to the surface (**Figure 9b**).
- iii. If the process described in **i** and **ii** occurs on an adjacent site (**Figure 9c,d**) and one of the dangling methyl groups undergoes a hydrogen-abstraction (**Figure 9e**) then a ring structure can form between the radicals securing the two carbon atoms into the lattice (**Figure 9f, 8g**).

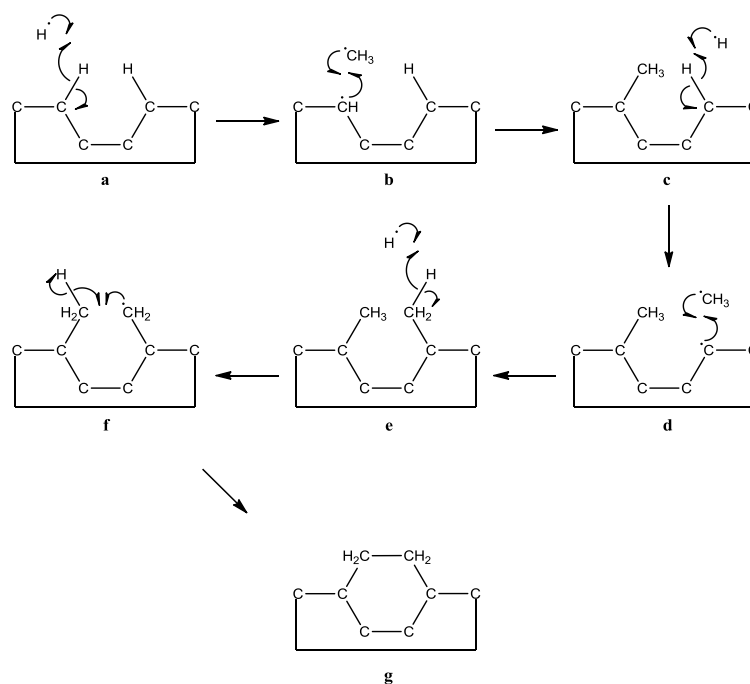


Figure 9: Mechanism demonstrating how diamond deposition occurs by step-wise reactions occurring at the growth surface.

3.3 Types of Synthetic Diamond

There are many morphologies of synthetic diamond available as varying the deposition conditions can alter the ratio of sp^2 - to sp^3 -bonded carbon, and the defect concentration of the material. The diamond morphology obtained from CVD will depend on the type of substrate, the process parameters, and the process gases. By placing a diamond seed crystal in the CVD reactor, single crystal diamond can be formed due to the deposition extending the existing lattice. When depositing thin films on non-diamond substrates, the diamond grown is comprised of many small crystallites (grains) of diamond, in which the boundaries between crystallites contain non- sp^3 -bonded carbon. The two most common morphologies are categorised by crystallite-size and are called microcrystalline (**Section 3.3.1**) and nanocrystalline diamond (**Section 3.3.2**).

3.3.1 Microcrystalline Diamond

In microcrystalline diamond (MCD) materials the grain sizes range from 0.1 - 10 μm . A single grain in an MCD film gets larger with increased deposition time, and accompanying film thickness, resulting in a columnar structure when viewed in cross-section (**Figure 10**).

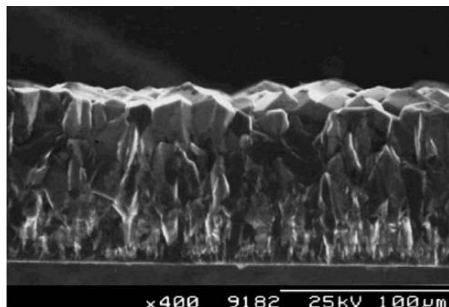


Figure 10: Scanning electron microscope (SEM) image of the cross-section of a MCD film showing columnar structure. Image reproduced from reference 39.

When growing MCD films, it is common for one diamond crystal plane to take precedence and influence the morphology of the deposited film. Miller indices^[40] are used to describe these planes with the three most dominant being the $\langle 111 \rangle$, $\langle 110 \rangle$ and $\langle 100 \rangle$ planes. **Figure 11** shows the three MCD morphologies that occur depending on which plane is dominant during growth. The $\langle 111 \rangle$ dominated morphology displays a pyramidal structure with triangular facets, the $\langle 100 \rangle$ is comprised of square facets^[41] and the $\langle 110 \rangle$ has a stepped-face appearance.^[42]

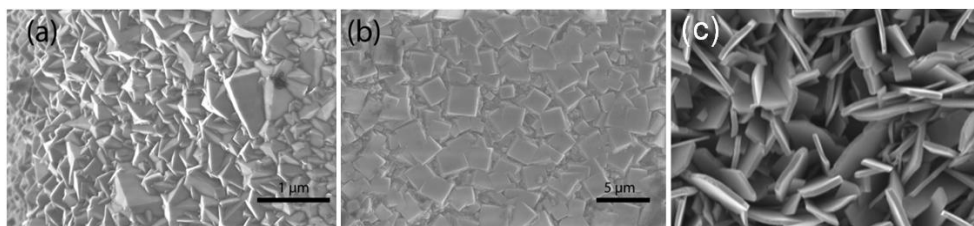


Figure 11: SEM images of three main MCD morphologies: (a) $\langle 111 \rangle$ (b) $\langle 100 \rangle$ (c) $\langle 110 \rangle$. Images reproduced from reference 41.

When using MWCVD to grow MCD films a plasma comprising methane in excess hydrogen is used and the methane concentration is fundamental in determining the resultant morphology. For methane concentrations less than 0.4 % of the inlet gas mixture, the films obtained are predominantly the (111) triangular facets, with some (100) facets present. By increasing the input concentration to between 0.4 and 1.2 %, the morphology becomes almost entirely (100) orientated. Higher concentrations of methane lead to a gradual reduction in the (100)-dominated morphology, until eventually the films are no longer microcrystalline.^[43]

3.3.2 Nanocrystalline Diamond

For nanocrystalline diamond (NCD) the grain sizes are < 100 nm, with those films exhibiting grains of < 10 nm often termed ultrananocrystalline diamond (UNCD) (**Section 3.3.3**). It is not only the grain size that distinguishes MCD from NCD; they also display distinctly different properties. NCD films have smoother surfaces than MCD due to the decrease in crystallite size (**Figure 12a**). However, this decrease in crystallite size is accompanied by a larger crystallite surface area for the entire film. Each crystallite has a termination layer of sp^2 -bonded carbon, thus the smaller the crystallites the higher the sp^2 -content of the film, and the lower the sp^3 -diamond content. Although this implies that NCD films are of lower quality than MCD, there are cases when the properties of NCD are superior to other diamond morphologies.^[44, 45] The cross-section of a NCD film does not show the columnar structure that is characteristic of MCD, and hence the surface roughness of an NCD film is independent of the deposition time or film thickness.^[46] This is due to a combination of relative changes in the concentration of growth species at the substrate surface, and chemical pathways arising resulting in a higher rate of renucleation which prevents the formation of larger crystals. These two points are covered in more detailed in **Section 3.4**. A common type of NCD morphology is called *ballas* (**Figure 12b**), these *ballas* structures originate from the same seeding point, however a MCD-type morphology is not obtained because renucleation will occur on the surface of these structures.^[47]

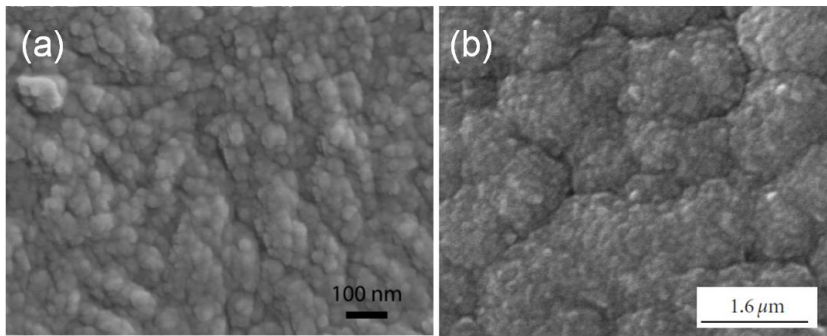


Figure 12: SEM images of NCD: (a) The NCD surface; image reproduced from reference 41 (b) *ballas* morphology; image reproduced from reference 48.

3.3.3 Ultrananocrystalline Diamond

UNCD (**Figure 13**) covers the lower limit of NCD morphologies but it is often characterised in its own right due to a few distinguishing features. The grain sizes in UNCD are so small that the film surface is incredibly smooth, such that it almost resembles the surface of a single crystal, and surprisingly the grain boundaries have a lower sp^2 -carbon content.^[47] These two key features makes UNCD an appealing material as it is suited to a wide range of applications, and may display single crystal properties while being a lot easier to fabricate over large areas.

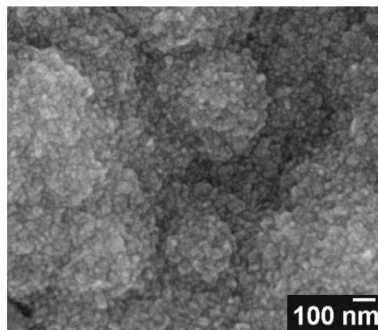


Figure 13: SEM image of UNCD diamond. Image reproduced from reference 47.

3.4 Nanocrystalline Diamond by MWCVD

When growing diamond using MWCVD, a variety of different process conditions can be adjusted in order to produce a nanocrystalline film. The main methods are summarised below with the addition of nitrogen gas to the process gas mixture being of particular relevance to this project.

3.4.1 Methane Concentration

The standard process gas mixture used for diamond-growth using MWCVD entails methane in an excess of hydrogen. As mentioned in **Section 3.3.1**, for input methane concentrations below 1.2 % the resultant morphology is microcrystalline. As the input methane concentration is increased beyond this value, the average size of crystallites decreases until for concentrations > 1.6 % the crystallite sizes have decreased below 100 nm and the films are declared nanocrystalline.^[43] This transition to NCD occurs due to the increased methane concentration altering the gas-phase composition and initiating re-nucleation processes on the diamond surface preventing large crystallites from being formed.^[49]

3.4.2 Argon-Rich Plasma

Nanocrystalline films can be produced by using a plasma in which argon makes up the majority of the gas mixture instead of hydrogen. The most common gas composition used in MWCVD to induce NCD in this way comprises a low concentration of CH₄ (< 1 %) in excess Ar, with an addition of only 1-2 % hydrogen to maintain a stable plasma.^[50, 51]

Other inert gases, such as He, Ne and Kr can be used in place of Ar, however much higher power densities are needed for the lighter gases while use of Kr is limited by its inherent cost.^[41]

3.4.3 Nitrogen Addition

An alternative method to inducing nanocrystalline morphology consists of addition of a low concentration of nitrogen to the standard MWCVD process gas mixture. The addition of nitrogen also increases the growth rate significantly: the presence of a low concentration of nitrogen (N:C < 0.4) in the input gas mixture is able to increase the growth rate up to a factor of eight with only negligible quantities of nitrogen incorporated into the film.^[52] This increase in growth rate is only seen in MWCVD.

In the plasma, the nitrogen reacts with hydrogen and carbon species to form HCN and CN radicals. When a CN radical adds to a reactive site on the carbon lattice, it does not have a terminal hydrogen, unlike the surface CH and CH₂ groups. It is this feature that is likely to be key to both the enhanced growth rate and inducing the nanocrystalline morphology. The lack of terminal hydrogen means that beta-scission is not possible for the CN adduct. Beta scission is the mechanism responsible for removing carbon from the surface; hydrogen abstraction forms a pendant CH₂-CH₂' radical which dissociates from the surface. This mechanism also prevents the formation of long-chained hydrocarbons.^[53] Since CN cannot take part in this mechanism it has a longer surface-lifetime than the

corresponding carbon-containing groups. As a result, the rate at which four-atom clusters are formed is higher and the growth of the surrounding carbon layer can occur faster. The CN adduct effectively acts to enhance the nucleation rate of the new carbon layer. It is this renucleation mechanism that prevents large diamond crystals from forming and, thus, induces a NCD morphology.

It should be noted that the positive effects of nitrogen addition are only applicable at very low concentrations. Increasing the nitrogen concentration decreases the crystallite sizes and increases deposition rate only up to a point. For N_2 input concentrations, $\chi_0(N_2)$, of 5 - 15 % the quantity of deposited diamond starts to decrease until the films begin to be non-continuous. By increasing the concentration beyond 15 %, the deposition of diamond is completely suppressed.^[41]

Due to the nitrogen addition enhancing the growth rate, it is this method that will be used in this project as a diamond thickness of at least 50 μm is desired for fabricating the lens chips.

4. Fabrication of Diamond Refractive Lenses

Due to the inherent difficulty in refracting x-rays, it was almost a century after the discovery of x-rays that the first refractive lens was fabricated. In 1996, Snigerev *et al.* constructed a CRL by drilling thirty 0.3 mm holes into a block of aluminium.^[14] The focal spot size achieved, using 14 keV energy x-rays, was 8 μm . Aristov *et al.* in 2000 realised the first refractive lens using silicon, achieving a focal width of 1.8 μm using x-rays at 15.6 keV.^[54] There is an advantage to using silicon for fabricating refractive lenses in that engineering and micro-technology of the material is so established and widely used in many industrial and electronics applications. As a result, silicon refractive lenses are currently the most successful and are able to focus to $< 200 \text{ nm}$.^[55] Lenses have also been fabricated using other materials such as beryllium^[56] and germanium.^[57, 58] Beryllium was of interest due it having a low atomic number, and germanium was investigated for focusing x-rays of $E > 20 \text{ keV}$, because the required radius of curvature is larger than in other materials being studied and so easier to manufacture.

Despite the manufacturing advantages of silicon, diamond contains a wide range of properties that make it a suitable candidate for creating x-ray refracting lenses. X-rays are highly absorbed in all materials due to x-ray waves interacting strongly with the electron cloud.^[16] As mentioned previously, this absorption varies as $Z^4\rho$, where Z is the atomic number and ρ the density. Diamond has a lower atomic number ($Z = 6$) and a lower absorption coefficient compared to silicon ($Z = 14$) making for a more efficient lens. In order to focus the hard x-rays, a material is required that will not deteriorate over long exposure times. Diamond is thermally very stable and so will not be affected by the intense radiation load. It also has an extremely low thermal expansion coefficient and high thermal conductivity which will prevent it from retaining the thermal energy from the radiation and will not expand on exposure which would reduce the focusing capability. Despite these advantages, the one drawback with using diamond is that the manufacturing techniques are less developed than with silicon.

Two approaches for fabricating low absorption diamond refractive lenses are summarised in the following two sections.

4.1 Etching Polycrystalline Diamond

It was not until 2003 that an x-ray lens was fabricated using diamond.^[4, 59] The engineering procedures previously used to fabricate lenses from materials such as aluminium^[13, 14] and beryllium^[56] were not suitable for use on diamond due to its extreme hardness.^[60] Methods

already well-established for use on diamond, such as laser ablation and ion beam milling, were not sensitive enough to create refractive lenses able to focus synchrotron radiation.^[61] Nöhammer *et al.* were the first to fabricate a diamond refractive x-ray lens by creating a kinoform lens from a polycrystalline diamond substrate grown by CVD using a procedure comprising of electron-beam lithography followed by deep reactive ion etching (**Figure 14**).^[4] Focusing efficiencies of up to 78 % and a line focal width of 3 μm were obtained. This line focus was considerably larger than that obtained with other materials, where resolution down to a few 100 nm was possible, yet it was believed that a smaller focal width could be achieved and theoretical efficiencies exceeding 95 % had been calculated.^[3,62,63]

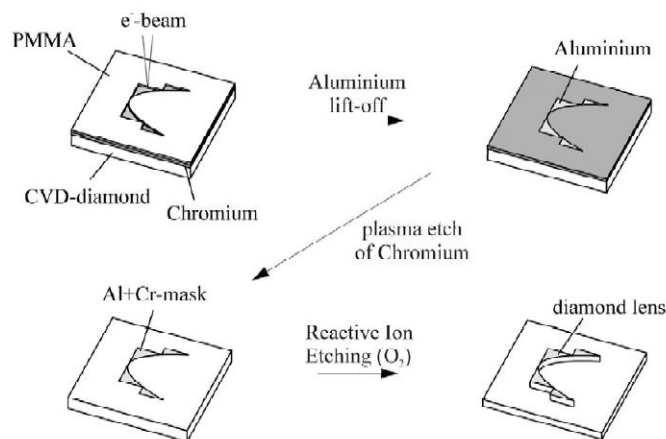


Figure 14: Fabrication process used by Nöhammer *et al.* for creating diamond refractive x-ray lenses. Reproduced from reference 4.

Although the successful use of diamond in refractive x-ray lenses was a great breakthrough this method has some limitations. When etching the lens, under-cutting occurs forming a lens shape which deviates from the ideal parabolic design where the lens sidewalls are not perfectly vertical. It can be seen from **Figure 15a** that the lens structure obtained is not perfect, there is a difference in quality between the top and bottom sections of the kinoform lens walls where the non-uniform etching of the diamond has created external defects. These can hinder the performance of the lens due to the distortions and roughness causing unwanted scattering.

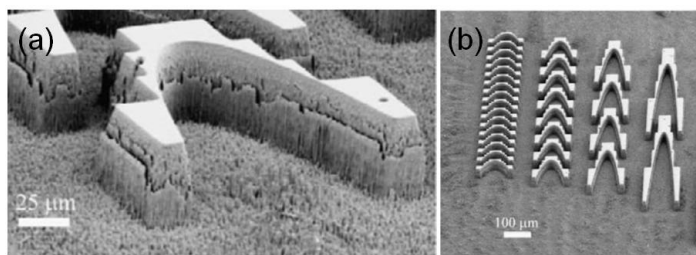


Figure 15: SEM image of diamond refractive lenses made by Nöhammer *et al.* Images reproduced from reference 4.

It has been hypothesised that a refractive lens made from single crystal diamond would be better as there would be no grain boundaries to cause x-ray scattering. However, working with single crystal diamond is not feasible as the largest substrates currently available are only 8×8 mm and are too small to accommodate the kinoform lens design which requires at least 10 mm in length.^[64] The best alternative is believed to be NCD, it has a smooth surface that will reduce x-ray scattering but also has sufficient sp^3 -bonded carbon to maintain the properties associated with diamond.

4.2 Using MWCVD

The next significant achievement in realising diamond refractive x-ray lenses came in 2010 when Alianelli *et al.* developed a microfocusing diamond CRL using a completely novel approach.^[61] The difficulties in attempting to etch diamond were circumvented by combining the already-existing micro-technology of silicon with advanced CVD of NCD, undertaken by the Micro- and Nanotechnology Centre (MNTC) and the University of Bristol Diamond Group, respectively.

In this method, a CRL lens array was patterned onto a silicon wafer using a polymer resist and UV-lithography which was then etched into the silicon creating a lens mould. This mould was seeded to produce a nucleation layer of diamond particles and NCD was deposited uniformly over the mould using MWCVD. The silicon was then etched away from the diamond leaving a free-standing diamond CRL structure (**Figure 16**). The lens performance on the x-ray beam showed an improvement on those tested by Nöhhammer *et al.*,^[4, 59, 65] by achieving a minimum focal line width of 1.6 and 2.2 μm (**Figure 18**), depending on the incident x-ray energy.^[61] There is uniformity to the lens efficiency throughout the structure, in contrast to Nöhhammer *et al.*, where non-uniform etching causes the efficiency to vary across the structure.

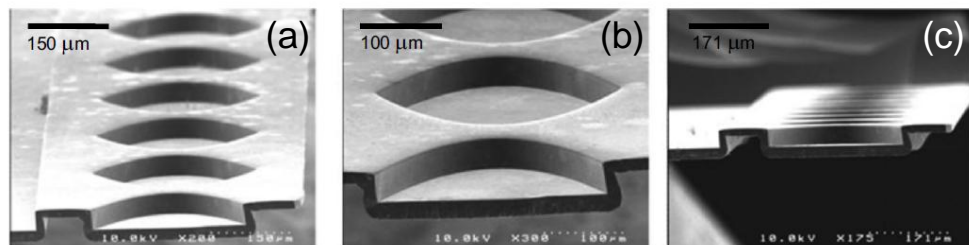


Figure 16: SEM images of the free-standing diamond CRL fabricated by Alianelli *et al.* Images reproduced from reference 61.

Scanning electron microscope (SEM) images have shown that the NCD layer deposited has extremely high fidelity to the substrate shape and highlighted a problem with the etch cycle causing nanometre-scale scalloping of the silicon surface. If the amount of scalloping can be reduced a much smoother diamond surface should be possible. The

focused line width from this study had some additional features resulting from unwanted scattering (**Figure 18a**). One possible reason for this is that the free standing lens bowed slightly although, with only a minor alteration to the MWCVD parameters, it should be possible to construct a thicker and more robust lens. Despite the focal line width here being the most successful published result using diamond, improvement is required in order for diamond lenses to be competitive with other materials, such as silicon. Optimisation of the diamond morphology is necessary in order to determine the most suitable morphology for reducing the scattering and absorption while improving the narrow focal line width. This method is extremely promising as fine adjustment of the diamond morphology is possible by tuning the deposition conditions, such as gas composition and plasma power density, to achieve the desired diamond crystal size, growth rate and quality.

In order to assess the quality of the lenses high resolution x-ray images were used before using a wire-scan to determine the focal width. The orientation of the x-ray beam with respect to the CRL is shown in **Figure 17** where it should be noted that the SEM image here shows three CRLs, each with the same focal width but designed for focusing a different beam energy. The initial x-ray images from the lenses are shown in **Figure 18**, the bright regions show the focused beam-width and the associated scattering. The full width half maximum (FWHM) from a wire-scan plot is used in order quantify the focal width achieved, as shown by the example in **Figure 19**.

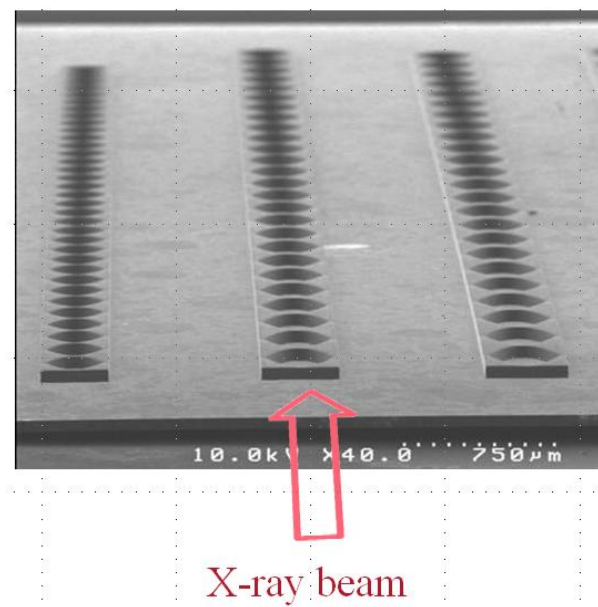


Figure 17: SEM image of three CRL trains showing where the x-ray beam enters the lens. Image courtesy of Lucia Alianelli, DLS.

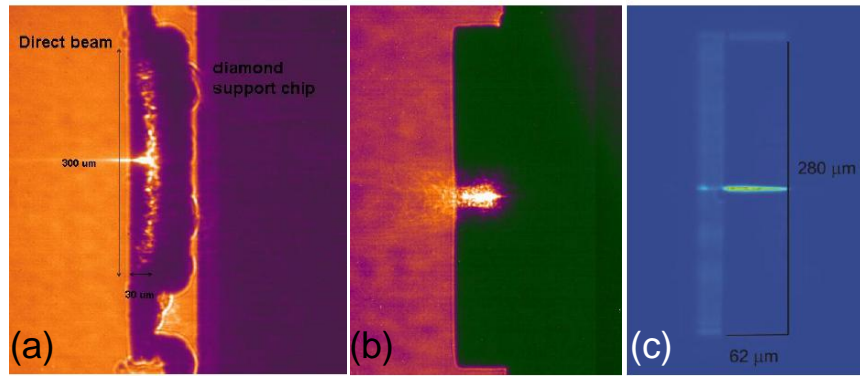


Figure 18: High resolution x-ray images ($E = 11\text{-}12$ keV) showing the x-ray lens performance of (a) the lens published by Alianelli *et al.* in 2010, $f = 1.6$ μm (b) optimised diamond lens fabricated in 2011, $f = 0.65$ μm (c) silicon lens currently used at the synchrotron (for progress comparison). Images courtesy of Lucia Alianelli, DLS.

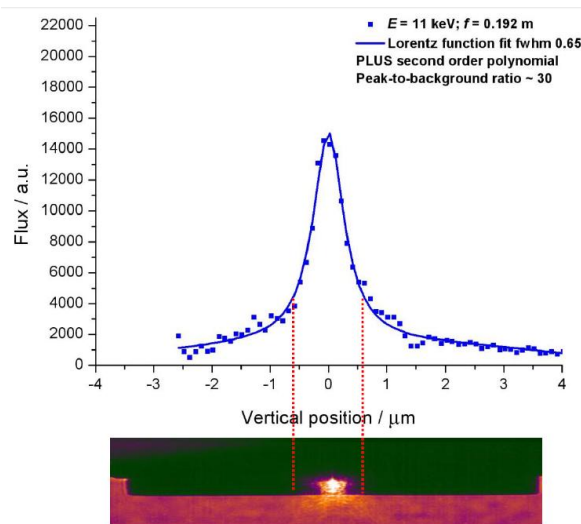


Figure 19: A wire-scan plot of x-ray flux intensity as a function of lens width showing how the focal-width is determined from the FWHM. The x-ray image below the plot shows the transition from illustrative to quantitative analysis. Image courtesy of Lucia Alianelli, DLS.

Some improvements and adjustments have been made since the publication by Alianelli *et al.*^[61] The collaboration has to date achieved a minimum focal line-width of 400 nm. This is the record for diamond refractive x-ray lenses and is approaching a focal size that is competitive with silicon refractive lenses. It is the extension and optimisation of this work that is the basis for this thesis. The deposition conditions for the lens fabrication need to be improved such that the focal width can be decreased yet further. Another extension to this work is to use the same CRL fabrication method to produce diamond kinoform lenses.

5. Experimental Method

5.1 MWCVD Reactor

A detailed description of the MWCVD equipment (**Figure 20**) can be found in Fox, 2011,^[41] however a brief overview is given below.

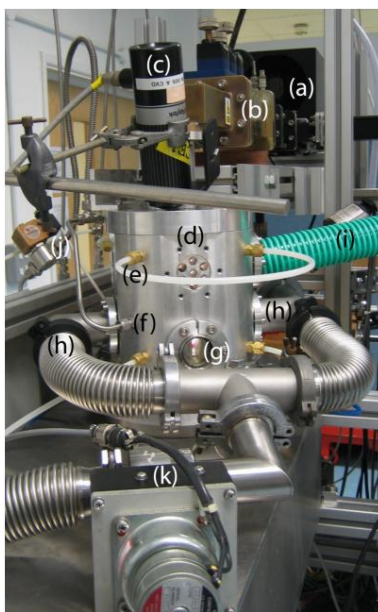


Figure 20: The MWCVD setup used for diamond deposition. (a) MW magnetron (b) MW waveguide (c) optical pyrometer (d) reaction chamber (e) water-cooler (f) process gas inlet (g) silica viewing window (h) gas exhaust (i) air-cooler pipe (j) solenoid valve (k) pressure regulating butterfly valve. Reproduced from reference 41.

The required flow rate for each of the process gases is set using an electronic control box (MKS 247 C) controlling six mass-flow-controllers (MFC), each of which has a filter and bypass valve. The gases are mixed and subsequently fed into the reactor chamber beneath the dielectric (silica) window. The process gases are activated by absorption of 2.45 GHz microwave radiation that is generated by a 1.5 kW magnetron (HS-1000) linked through a thermal load (CS-1000) and a directional coupler (DCS-1000). A radio frequency diode measures the excess power that is reflected back from the reaction cavity. This energy is then absorbed by a water-cooled thermal load and protects the magnetron. In order to enable optimum resonance (which differs for each deposition condition), a waveguide is used to tune the incident microwave radiation.

The silicon lens-mould is placed onto a molybdenum substrate holder situated in the centre of the reaction chamber on a 250 μm -thick tungsten wire. The tungsten wire acts as a thermal break between the substrate (~ 1000 K) and the water-cooled reactor base.

A two-wavelength optical pyrometer (Raytek Thermalert SX) is focused onto the sample and is used to measure its surface temperature. As the diamond begins to grow, the

emissivity of the surface changes and results in a variation in the temperature measured by the pyrometer. This change in emissivity will limit the accuracy of the temperature reading with time, because the pyrometer is calibrated to a set emissivity of 0.6 – the emissivity of silicon at 1000 K.

5.2 Controlling the Gas Flow

Prior to running the depositions, it was important to ensure that all the MFCs were correctly calibrated. This entailed measuring the pressure rise within the reaction chamber, with the exhaust pump from the reaction chamber closed, for a set flow rate, $F(x)$. An appropriate range of flow rates was chosen for each gas depending on both the capacity of the MFC and the values of $F(x)$ that were likely to be used for CVD. The results are shown in (**Figure 21**). It can be seen that the data for the four gases are aligned along the same trend confirming that the MFCs are appropriately calibrated. It should be noted that at the lowest $F(\text{Ar})$, the data points deviate slightly from this trend due to the large capacity of the MFC resulting in inaccuracies arising when using low flow rates. This problem can be circumvented by flowing argon through the nitrogen MFC when low flow rates are required and applying the appropriate gas correction factor.

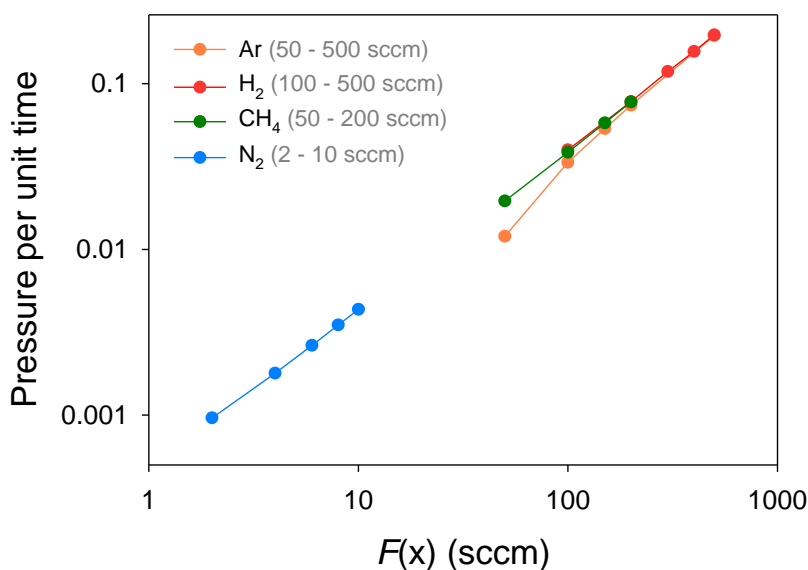


Figure 21: Calibration of MFCs by measuring the change in pressure per unit time as a function of the $F(x)$; $x = \text{Ar}, \text{H}_2, \text{CH}_4, \text{N}_2$. The flow-rate range for each MFC is shown in brackets. Axes have been scaled logarithmically for ease of display.

5.3 Nucleation of the Sample

If diamond is to be deposited by CVD onto a non-diamond substrate (heteroepitaxial growth), it is essential to create nucleation sites at which the diamond can initially start to grow. For this project, the lens moulds are made of silicon and the moulds need to be

nucleated with 5 nm nanodiamond grains prior to deposition. There are a range of nucleation methods that have been developed^[18] of which three methods were used here; ultrasonic (US) abrasion (**Section 5.3.1**), electrospray (ES) method (**Section 5.3.2**) and a self-assembly method (**Section 6.2.4**). The ES method is traditionally preferred over the US in order to create an extremely uniform, monolayer of diamond. Despite this, the former was used for the initial part of this project due to the ES apparatus not functioning.

5.3.1 Ultrasonic Probe Nucleation

A colloidal suspension of diamond nanoparticles (~ 5 nm) dispersed in water was made up at ~0.84 wt %. The samples were then submersed in the suspension and a US probe (Bandelin Sonoplus HD2070, 3 mm microtip) at low power was used to agitate the mixture. The total agitation time was 20 minutes: 5 minute runs at four different probe-sample orientations. This method should create homogeneous nucleation layers however it was found that occasionally diamond particles would cluster on the edges of the samples, partly due to the post-treatment washing and drying. Upon deposition, uniform growth was still obtained, however the ES method produced better results.

5.3.2 Electrospray Method

The electrospray (ES) method entails application of a strong electric field to a colloidal suspension of diamond nanoparticles, causing highly charged droplets to form and exit from a nozzle.^[66] These droplets are of like charge and so repel each other, preventing aggregation of droplets. They are applied evenly and uniformly to a grounded substrate creating a homogeneous monolayer of diamond nanoparticles.

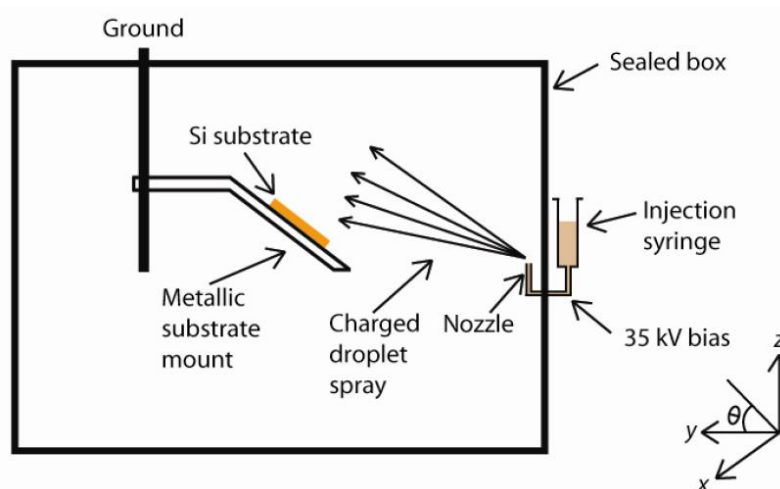


Figure 22: Schematic diagram of the ES deposition apparatus. The coordinates are used to define the angle, θ : the orientation of the substrate relative to the syringe nozzle. Reproduced from reference 41.

A colloidal solution of diamond nanoparticles (~ 5 nm) dispersed in methanol was made up to ~ 1.56 wt %. Approximately 1 ml of this colloidal suspension was injected into a 21G syringe (external diameter = 0.81 mm) situated on the exterior of an insulating box, arranged as shown in **Figure 22**. The sample was placed on a mount at $\theta = 50^\circ$, and ~ 50 mm from the syringe nozzle. Two mounts were used in this project; the standard mount is conducting and able to spin up to 1500 rpm by using a small motor, the second mount is made of an insulating material and is static. A bias potential ranging from 30 - 40 kV was applied to the metal syringe needle resulting in the colloidal suspension being forced out the nozzle forming an aerosol. The methanol evaporates *en route* to the sample such that only diamond nanoparticles arrive at the surface, creating a homogenous nucleation layer.

5.4 Spectroscopic Analysis of the Plasma

5.4.1 Optical Emission Spectroscopy

Optical emission spectroscopy (OES) is a diagnostic technique that allows detection of the excited species present in the plasma, and so can give an indication of the growth environment composition. When an excited atom or molecule relaxes to its ground state, or other low-energy configurations, it emits radiation. OES measures the intensity of this radiation to form a spectrum over a certain wavelength range. It is a simple technique that can provide a lot of information about the different environments in which diamond is deposited. However, it is important to note that it cannot provide information on ground-state species, or those which do not emit radiation in the wavelength range investigated.

The MWCVD reactor has a silica viewing window allowing an optical fibre to collect light directly from the plasma. The radiation was analysed using an Oriel Intraspec IV Spectrometer. Light enters a 25 cm monochromator and is subsequently dispersed by a grating onto a cooled charge-coupled device (CCD) detector. The CCD detector converts the light into digital signals which are displayed as a spectrum on the computer. Prior to taking spectra of the plasma, a wavelength scale was calibrated using a mercury lamp (because the lines characteristic to its spectrum are well known), and a background spectrum inside the reaction chamber with no plasma. Exposure times of 0.019 ms were used, and the data was amassed over 500 accumulations.

When the various transitions in the spectrum had been identified, intensities were obtained by extracting the background count rate. As the baseline is not flat, a different background had to be calculated and subtracted for each peak being analysed.

5.5 Characterisation of Diamond Films

5.5.1 Raman Spectroscopy

Raman spectroscopy is a non-invasive technique that allows quick characterisation of the diamond film. By comparing the relative signals obtained from diamond (sp^3 -bonded carbon) and non-diamond (in particular sp^2 -bonded carbon), the quality of the diamond film, as well as variation of quality across a sample, can be quickly assessed and compared to other samples grown at different conditions. The type of diamond film grown (MCD, NCD *etc.*) can quickly then be determined.

Raman spectroscopy can be used to characterise solids, liquids and gases by analysing the energy exchange between incident photons on a lattice with the phonons (quantised lattice vibrations) within. When a monochromatic photon source is incident upon a sample, a phonon mode can be excited into a higher virtual energy state. This arises due to interaction of the electron cloud with the incoming photon. Upon relaxation, three possible scattering scenarios arise, depending on the photon-phonon interaction. These are summarised below and demonstrated pictorially in **Figure 23**:

- i. *Rayleigh Scattering* – elastic scattering: a photon is emitted of equal energy to the incident photon *i.e.* energy has not been exchanged with the sample.
- ii. *Stokes Scattering* – the phonon relaxes into a virtual state of higher energy than the initial state and the excess energy is emitted as a photon. In this case the emitted photon will be of lower energy than the incident photon.
- iii. *Anti-Stokes Scattering* – the phonon relaxes into a virtual state of lower energy than the initial and, as such, the emitted photon is of higher energy than the incident photon.

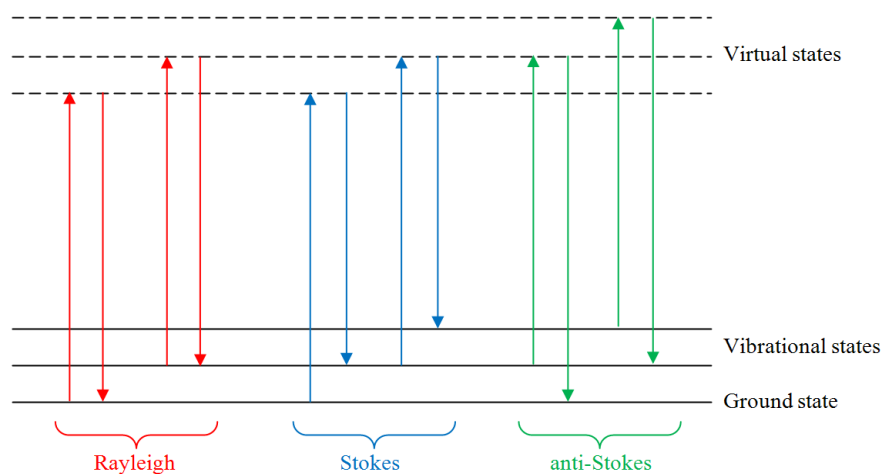


Figure 23: Schematic diagram demonstrating the three types of scattering (both elastic and inelastic) that can occur on relaxation of excited (virtual) states to lower energy states during Raman excitation.

By detecting the photons emitted by the inelastic scattering (Stokes, anti-Stokes), and comparing their energy to that of the incident, information can be obtained on the phonons within the lattice and, therefore, information on the structure of the sample under investigation. Rayleigh scattering is the most common form of scattering but it does not contribute to a Raman spectrum, which is comprised solely of contributions from inelastic scattering. The signal obtained for Stokes scattering is considerably higher than that of anti-Stokes at room temperature and, thus, Stokes Raman spectroscopy is used in this project.

Not everything will display a Raman spectrum. The interaction of the photon with the molecule or lattice relies upon distortion of the electron cloud occurring as a result of the electromagnetic field associated with the incident photons. This distortion depends upon the polarisability of the molecule or lattice, and a transition can only be deemed Raman active if the resulting rotation or vibration has a change in polarisability. If the point group is known, then its Raman active modes can be easily identified. For solid-state Raman spectroscopy there is another criteria for a Raman active mode in that $k = 0$, where k is a wavevector of the Bravais lattice.

As the CVD diamond films grown in this project are made up of small diamond crystallites, as opposed to a single crystal diamond, they are not solely comprised of sp^3 -hybridised carbon (diamond). Instead, there will be non-diamond carbon present as well and in particular sp^2 -hybridised carbon. This makes analysis of the Raman spectrum more complicated than when looking at single crystal diamond (or single crystal graphite). Moreover, the intensities of these different carbon components can vary depending on the excitation wavelength (λ_{exc}) chosen. For this reason, it is advisable to use more than one excitation wavelength to allow full characterisation of the sample. In this project, two types of spectra have been recorded: one using a UV laser ($\lambda_{exc} = 325$ nm) and one using a green laser ($\lambda_{exc} = 514$ nm). Discrepancies between the two spectra and their respective strengths and weaknesses will be discussed.

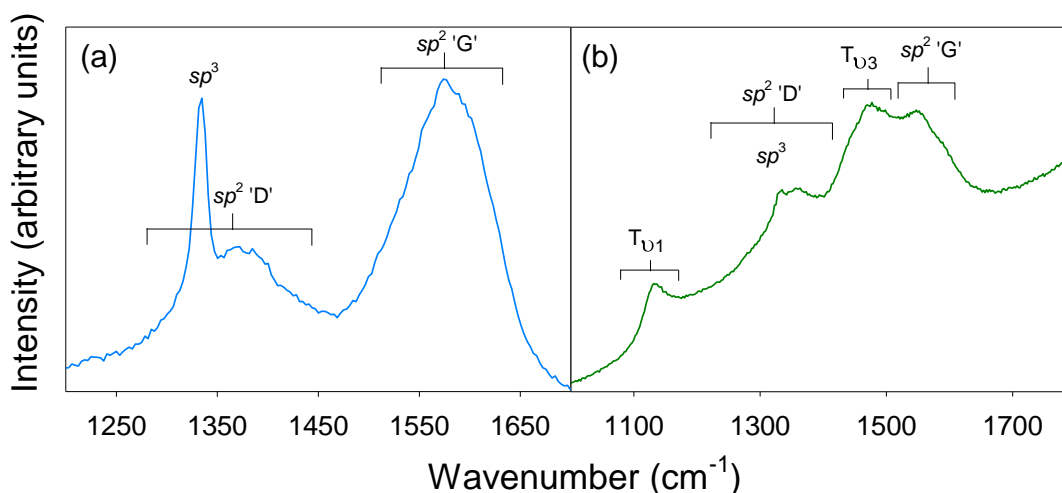


Figure 24: Raman spectra of nanocrystalline diamond taken using (a) UV, $\lambda_{exc} = 325$ nm (b) green $\lambda_{exc} = 514$ nm.

Figure 24 shows two example Raman spectra from lens samples grown in this project, they highlight the four main peaks that arise from NCD material. Each signal, its origin and importance in characterising the film will be discussed below.

sp^3 -bonded carbon ($\sim 1332 \text{ cm}^{-1}$): This is the first order Raman peak for pure single crystal diamond.^[67] The diamond structure comprises of a face centred cubic (fcc) lattice which accumulates into the space group F_{d3m} (*cf.* **Figure 6a**). It belongs to the O_h point group of which there is just one Raman active mode. This mode is first order (involves only one phonon) and triply degenerate (T_{2g} symmetry) (**Figure 25a**). It occurs at $\sim 1332 \text{ cm}^{-1}$ and can be used as a diamond fingerprint, where presence of this peak is unambiguous evidence of sp^3 -hybridised carbon. In SCD this is the only peak that will be present in the Raman spectrum.

sp^2 -bonded carbon ‘G’ peak ($\sim 1550 \text{ cm}^{-1}$): This is the only Raman peak present in a spectrum of single crystal graphite.^[44] The graphite lattice (*cf.* **Figure 6b**), comprises of layers of 2-dimensional sheets arranged in a regular hexagonal network of sp^2 -hybridised carbon. It belongs to the $P_{63/mmc}$ space group, and the D_{6h} point group of which the Raman active mode is doubly degenerate (E_{2g} symmetry) (**Figure 25b**). In terms of the presence of this peak in NCD, it is often very broad due to the greater disorder and smaller crystal sizes compared with single crystal graphite.

sp^2 -bonded carbon ‘D’ peak ($\sim 1357 \text{ cm}^{-1}$): This peak is not present in single crystal graphite but is present in other types of sp^2 -bonded material (*e.g.* charcoal) and diamond thin films.^[44] Due to the larger amount of lattice disorder in these materials and as a result of the smaller crystallite sizes, the $k = 0$ selection rule breaks down thus activating a new phonon mode. This mode is singly degenerate (A_{1g} symmetry) (**Figure 25c**).

‘ T_{v1} ’ peak ($\sim 1150 \text{ cm}^{-1}$): This is the first phonon frequency for *trans*-polyacetylene. The origin of this peak was under debate for a long while, and initially referred to as the ‘UNCD’ peak, due to only arising in smooth nanocrystalline films. Ferrari and Robertson in 2004 confirmed its origin to *trans*-polyacetylene.^[68] The presence of this peak is highly dependent on λ_{exc} , and in this thesis is only present for the $\lambda_{exc} = 514 \text{ nm}$ Raman spectra.

‘ T_{v3} ’ peak ($\sim 1480 \text{ cm}^{-1}$): This is the third phonon frequency for *trans*-polyacetylene. Its close proximity to the ‘G’ peak means that often the presence of this peak is less obvious than the associated ‘ T_{v1} ’ peak. There is also a second phonon frequency (‘ T_{v2} ’), however its low intensity is dominated by the ‘D’ peak and so not visible in Raman spectra for NCD.^[68]

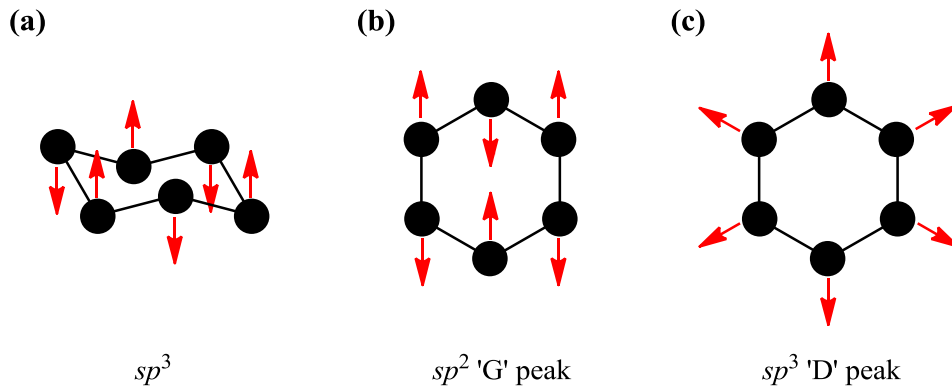


Figure 25: The Raman stretching modes for (a) diamond, sp^3 (b) sp^2 'G' peak (c) sp^3 'D' peak.

In synthetic CVD diamond, as the crystallite size decreases, the amount of non-diamond material in the film increases due to the increased surface area of grain boundaries. As a result, the intensity and line-widths of both the sp^2 peaks will increase with decreasing crystallite size. For this reason, the ratio of the sp^3 peak intensity to either sp^2 peak intensity is often used to assess the film quality and crystallite size, although the λ_{exc} will have some effect on which modes interact more strongly. Another complicating issue arises from the fact that the Raman cross-section for diamond, graphite (sp^2) and amorphous carbon (a-C) are not the same. The cross-section for diamond is $\times 50$ smaller than graphite and $\times 233$ smaller than a-C.^[67] Additionally, the position of the 'D' peak decreases with increasing λ_{exc} , while that of the 'G' peak and sp^3 -peak remain constant irrespective of the excitation energy. These discrepancies are believed to be either due to absorption effects^[69] or resonance effects.^[70]

The spectrum obtained using $\lambda_{exc} = 514$ nm (**Figure 24b**) has a rising background which is due to photoluminescence arising from the presence of nitrogen-vacancy defect centres.^[71] It should be noted that photoluminescence is present in all the Raman spectra, but often to a lesser extent. To achieve quantitative results from the spectra deconvolution of the individual peaks and the background is necessary. Previous work using UV ($\lambda_{exc} = 325$ nm) Raman has shown that, for MWCVD-grown diamond, a ratio of the sp^3 peak intensity to the sp^2 'D' peak intensity > 5 generally corresponds to the MCD morphology because there is only a little sp^2 character in the film. Similarly, a ratio of < 2 corresponds to deposition of NCD and so can be used as a rough guide when determining the crystal morphology in the deposited films.^[41]

Room temperature Raman spectroscopy was performed on a Renishaw 2000 instrument using two laser excitation wavelengths of 325 nm (UV, He:Cd) and 514 nm (green, Ar⁺). The Raman spectra obtained were analysed using the *fityk*^[72] graph-fitting program and entailed removing the background that arises due to interference and photoluminescence, and deconvoluting each spectral peak by fitting them with a Gaussian function. The deconvolution is important in order to determine the relative contribution for the overlapping sp^3 and sp^2 signals.

5.5.2 Optical Microscopy

Analysis of the cross-section of the diamond lens samples was crucial for this project in order to observe how the diamond is filling the silicon moulds. An optical microscope (Zeiss Axiolab) provided magnification of up to $\times 1000$ and was used to determine the uniformity of the deposition, the surface coverage, and an indication of the relative growth on the top of the lens and in the recessed areas.

5.5.3 Scanning Electron Microscopy

Scanning electron microscopy (SEM) can be used to determine the preferred crystal orientation, the morphology and the thickness of a deposited diamond film. In this project, the deposition conditions are known to induce nanocrystalline morphology and electron microscopy was mainly used to find the film thickness in the different regions of the lens and to get an indication of how the surface treatment is effecting the diamond deposition. The cross-sections of the lens samples were prepared by using a laser micromachining system (Oxford Lasers Alpha 532 System) to cleave them along a particular axis. With knowledge of the deposition time, the average growth rate for the different regions of the mould was determined by measuring the cross-sectional thicknesses. An example of the cross-section of two kinoform lenses is shown in **Figure 26**.

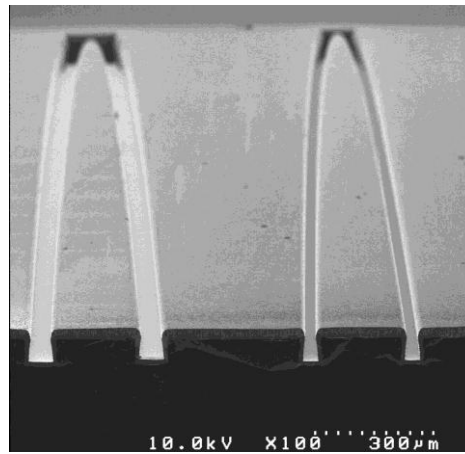


Figure 26: SEM image of cross-section of two kinoform lenses after cleaving a sample using the laser micromachine.

An SEM creates high resolution and high magnification images by focusing an electron beam down onto the sample using electromagnetic fields between 0.5 and 30 kV. The beam is rastered across the sample surface and produces an image by detecting the secondary electrons emitted. Two scanning electron microscopes have been used in this project, a JEOL JSM 5600 LV instrument and a JEOL JSM 6330 F instrument which use different techniques in order to produce the electron beam: the former uses thermionic emission and the latter uses field emission.

6. Results and Discussion

The aim of this diamond x-ray lens project, a collaboration between DLS, MNTC and the University of Bristol, has been to create robust, low-absorption, free-standing diamond lenses able to focus hard x-rays at synchrotron sources down to nanometre resolution and forms an extension of the work discussed in **Section 4.2**. The fabricated lenses will eventually either be used at synchrotron sources to replace the currently-used, silicon mirrors, or they will be used in conjunction with the silicon mirrors to reduce the focal size further without losing too much of the beam intensity. The latter arrangement should enable a focal-width of < 100 nm to be achieved, thus realising the use of hard x-rays as a nanoscopic probe.

Recent work on the diamond x-ray lens project has looked at two main areas and will be addressed in the following sections. The first objective was to provide a set of samples grown under different deposition conditions that allowed the diamond grain size and the $sp^3:sp^2$ ratio most suitable for use in high quality CVD diamond lenses to be determined. These deposition conditions were predominantly looking at the variation in the amount of nitrogen, $\chi_0(N_2)$, added to the process gas mixture and in this thesis the subsequent analysis of these samples by Raman spectroscopy, electron microscopy and, of the plasma, using OES. In **Figure 18** we saw that the x-ray images have some contribution from small angle x-ray scattering (SAXS) which needs to be reduced or eliminated in order to achieve smaller focal widths. These samples will be tested at DLS using the Small Angle Scattering and Diffraction beamline, in order to see which deposition conditions are able to most successfully eliminate this scattering. Another important consideration is the ratio of sp^3 - to sp^2 -bonded carbon because, while unwanted scattering needs to be reduced, the physical properties of bulk diamond do not want to be lost. These samples will also be tested at DLS using near-edge x-ray absorption fine structure (NEXAFS) spectroscopy because it allows quantitative analysis of the $sp^3:sp^2$ -bonded carbon. These two techniques will be crucial in determining the optimum CVD diamond material to be used for the lenses.

The second objective was to investigate the optimum nucleation method and deposition conditions in order to have a uniform filling of the lens moulds, ideally comprising diamond film thickness throughout the entire lens of > 50 μm . The test lens moulds fabricated at MNTC are designed with a range of aspect-ratio structures. At the beginning of the project it was observed that there was an undesired tendency, in high aspect-ratio samples, for voids to form in the centre of the mould due to the difference in growth rate between the top and the bottom surfaces of the lens structures.

A series of lens moulds were fabricated on 20×20 mm silicon substrates by MNTC, and diamond was grown by MWCVD at the University of Bristol. Testing the focusing

capability of the lenses was carried out at DLS. Each silicon chip has a number of lenses on it, each with a fixed focal length, but responsible for focusing a different incident x-ray energy. Examples are shown in **Figure 27**, showing a CRL chip with 13 lenses and a kinoform chip with 10 lenses.

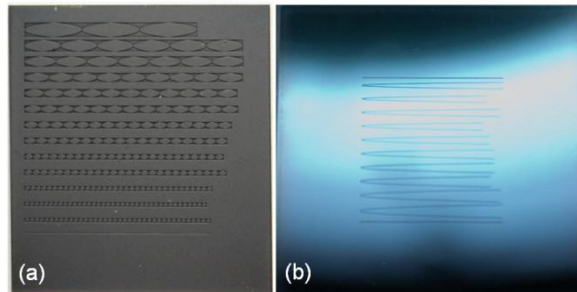


Figure 27: (a) NCD film deposited onto a 13 lens, silicon CRL mould (b) 10 lens, silicon kinoform mould. The straight lines above and below the lens structures are alignment bars.

The standard process conditions are defined as $\text{H}_2/\text{CH}_4/\text{N}_2 = 92.76/6.49/0.74$ % (corresponding to 500/35/4 sccm), and the plasma parameters of input power, P , of 1 kW, chamber pressure, p , of 110 Torr. A 3-mm-high molybdenum substrate holder was used. For the following report any deviations from these standard conditions will be clearly stated. The substrate temperature (T_s) was recorded for each deposition using an IR pyrometer, and under these standard conditions the $T_s \sim 700$ °C.

6.1 Nitrogen Addition and an Argon-Rich Plasma

As discussed, adding nitrogen to a H_2/CH_4 process gas mixture induces nanocrystalline morphology and increases the growth rate. The nanocrystalline diamond is believed to be important for reducing SAXS, and increasing the growth rate is crucial in order to fabricate robust lenses on a feasible timescale. Ten lens-samples were grown using a range of $\chi_0(\text{N}_2)$ from 0.19 to 1.83 % (samples **a – j**) and the films characterised using Raman spectroscopy and electron microscopy, together with OES analysis of the plasma. Changing $\chi_0(\text{N}_2)$ in this range was thought to alter both the crystallite size and filling of the lens moulds due to the different growth rates. It should be noted that three of the samples were grown using the standard conditions, with exception of one using a higher molybdenum substrate holder. This was to demonstrate the repeatability of this method for depositing diamond onto the lens moulds. It is also possible to induce a nanocrystalline morphology using an argon-rich plasma and this was investigated (samples **k, l**), although the results were less successful and the growth rate too low to be useable. The results are detailed and discussed in the following three sections. The deposition conditions for the twelve samples are detailed in **Table 1**. For samples **a - j** the reason for the small fluctuations in $\chi_0(\text{H}_2)$ and $\chi_0(\text{CH}_4)$ is that the increase in

$\chi_0(\text{N}_2)$ was controlled by the MFC by increasing $F(\text{N}_2)$, while the $F(\text{H}_2)$ and $F(\text{CH}_4)$ were held constant. As the concentration fluctuation of H_2 and CH_4 is small, it can be assumed to be constant and that any variation in the diamond film morphology is dependent on $\chi_0(\text{N}_2)$ only (or $\chi_0(\text{Ar})$, in the case of **k** and **l**).

Table 1: Experimental details for the twelve deposition conditions. For all lenses, $P = 1$ kW, $p = 110$ Torr, $t = 10$ h and the 3 mm Mo substrate holder was used. Exceptions are sample **c** for which $t = 5$ h, and sample **g** which used a 5 mm Mo substrate holder.

Sample	$\chi_0(\text{H}_2)$ (%)	$\chi_0(\text{CH}_4)$ (%)	$\chi_0(\text{N}_2)$ (%)	$\chi_0(\text{Ar})$ (%)	T_s (°C)
a	93.28	6.53	0.19	0	690-700
b	93.11	6.52	0.37	0	680-700
c	92.94	6.51	0.56	0	690
d	86.36	6.05	0.69	6.91	690-700
e	92.76	6.49	0.74	0	680-700
f	92.76	6.49	0.74	0	690-700
g	92.76	6.49	0.74	0	680-700
h	92.42	6.47	1.11	0	690-700
i	92.08	6.45	1.47	0	690-700
j	91.74	6.42	1.83	0	690-700
k	14.15	0.94	0	84.91	780
l	15.88	0.99	0.79	83.33	790

Photographs have been taken of the diamond films (**Figure 28**) and although quantitative data cannot be obtained from them, visually they give an indication of the success and uniformity of a deposition. Raman spectra were taken at different regions across each sample ('edge', 'intermediate' and 'centre') to assess the uniformity in quality across the lens mould, these positions have been labelled on the photographs. The photographs will be discussed in the following sections. The seed layer of sample **c** ($\chi_0(\text{N}_2) = 0.56$ %) was manually wiped off before placing in the reactor. For this reason, the effect of $\chi_0(\text{N}_2)$ on the Raman spectra will be discussed, but not on the filling of the lens moulds.

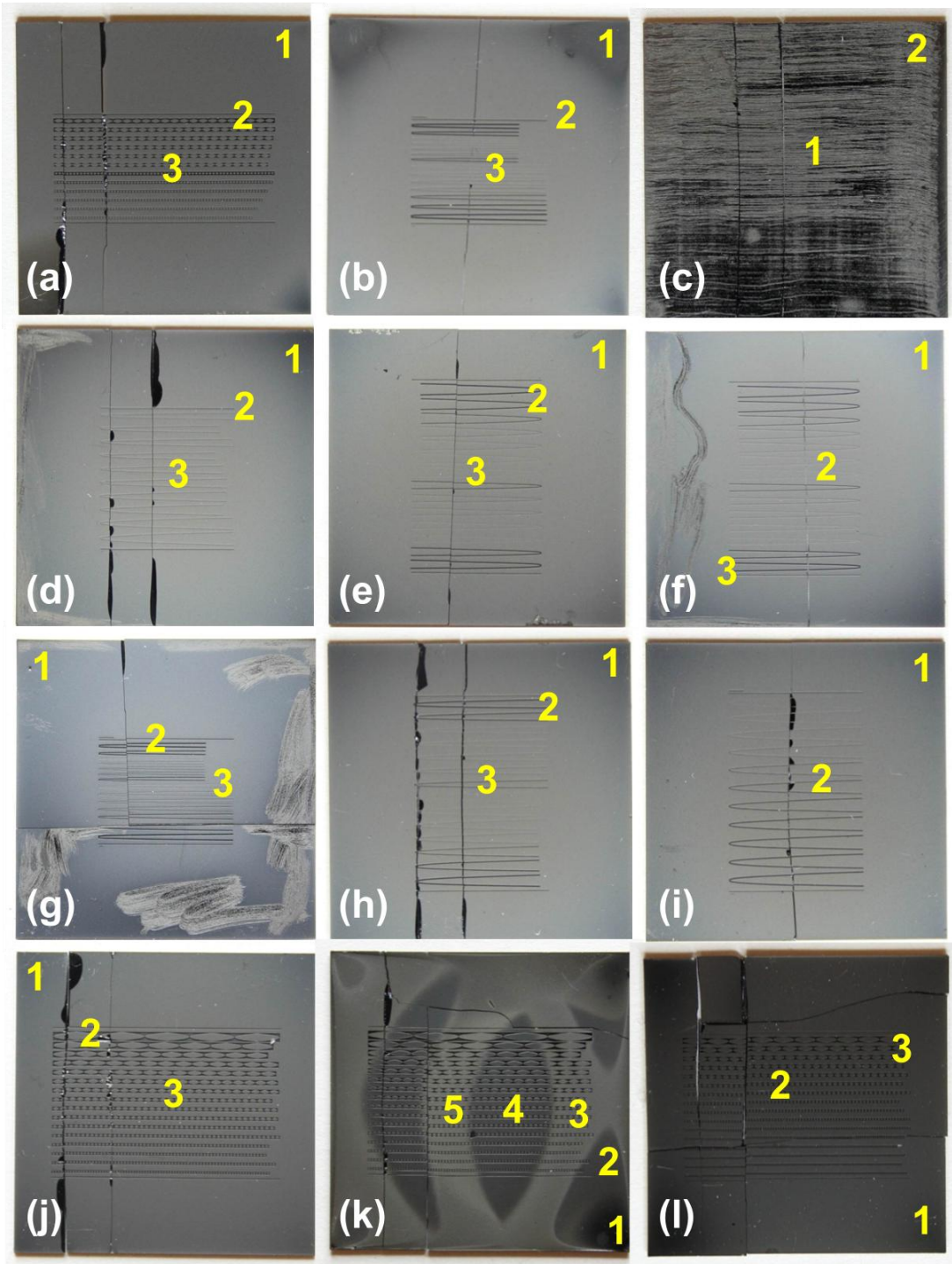


Figure 28: Photographs of the twelve lens samples (a) $\chi_0(\text{N}_2) = 0.19\%$ (b) $\chi_0(\text{N}_2) = 0.37\%$ (c) $\chi_0(\text{N}_2) = 0.56\%$ (d) $\chi_0(\text{N}_2) = 0.69\%$ & $\chi_0(\text{Ar}) = 6.90\%$ (e) $\chi_0(\text{N}_2) = 0.74\%$ (f) $\chi_0(\text{N}_2) = 0.74\%$ (g) $\chi_0(\text{N}_2) = 0.74\%$ (5 mm substrate holder) (h) $\chi_0(\text{N}_2) = 1.11\%$ (i) $\chi_0(\text{N}_2) = 1.47\%$ (j) $\chi_0(\text{N}_2) = 1.83\%$ (k) $\chi_0(\text{N}_2) = 0.00\%$ & $\chi_0(\text{Ar}) = 84.0\%$ (l) $\chi_0(\text{N}_2) = 0.79\%$ & $\chi_0(\text{Ar}) = 83.3\%$. The numbers indicate the positions where Raman spectra have been taken.

6.1.1 Laser Raman Spectra

As mentioned in **Section 5.5.1**, Raman spectroscopy is a non-destructive and powerful technique that allows quick analysis of the quality of the samples grown. Two laser excitation wavelengths have been used in this project (UV, $\lambda_{\text{exc}} = 325\text{ nm}$ and green,

$\lambda_{\text{exc}} = 514 \text{ nm}$), the former has been to obtained quantitative results on the sp^3 - and sp^2 -bonded carbon, while the latter has been used to discuss the presence of *trans*-polyacetylene. The main peaks were fitted by Gaussian functions using the *fityk*^[72] program, obtaining values for the peak centre, intensity, full-width at half-maximum (FWHM) and the peak area. Of particular interest, when comparing the $sp^3:sp^2$ ratios between samples, is their respective intensities. The FWHM is mainly used to ensure that a suitable Gaussian fit has been used for each signal. An example of a fitted spectrum from *fityk* is shown in the following figure.

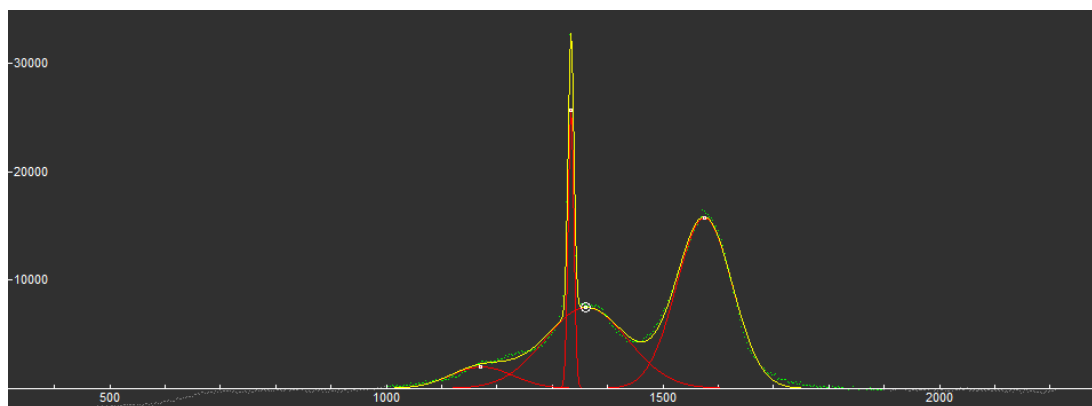
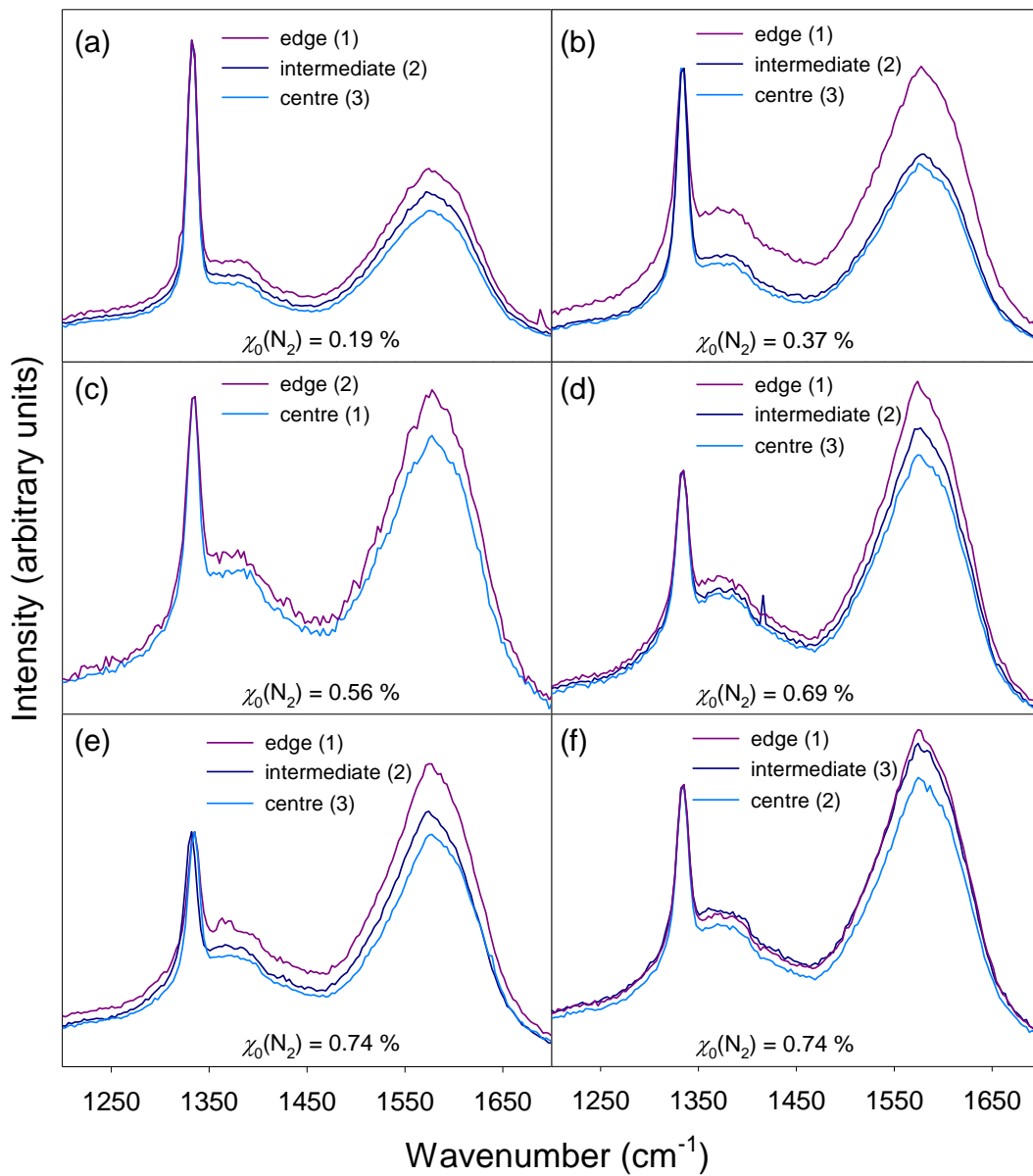


Figure 29: Spectrum fitted using *fityk* where the green line is the raw data, the red lines are the individual Gaussian functions and the yellow line is the fit created by the program.

The UV Raman spectra for the twelve samples are displayed in **Figure 30** and **Figure 31** where for ease of analysis, the spectra have been displayed in two different ways; one normalised with respect to the sp^3 diamond peak (**Figure 30**), and the other with respect to the sp^2 ‘G’ peak (**Figure 31**).

Spectra taken at a central position on samples **a - j** are also plotted together to allow immediate comparison between the different films deposited (**Figure 32**). The spectra show that, despite only a narrow range of $\chi_0(\text{N}_2)$, each lens sample has a different spectrum and $sp^3:sp^2$ ratio. Sample **a** corresponds to the lowest nitrogen concentration and demonstrates the highest quality diamond film where the sp^3 peak at $\sim 1332 \text{ cm}^{-1}$ is sharp and intense compared with the sp^2 ‘G’ peak. The sp^2 ‘D’ peak is only just visible and confirms nanocrystalline morphology although the larger crystallite size means the sp^2 -character in the film is restricted. At the other extreme, sample **j** was grown with the highest nitrogen concentration and the Raman spectrum displays different peak intensities than the low $\chi_0(\text{N}_2)$ spectrum. The intensity of the sp^3 peak has decreased fourfold, and is accompanied by an increase in the FWHM. Alongside this, the sp^2 ‘G’ peak has a higher intensity, and the sp^2 ‘D’ peak is more distinguishable. The crystallites in this sample are smaller giving a higher grain-boundary surface area which explains the higher degree of sp^2 -hybridised carbon. For the intermediate concentrations (**b - i**) each subsequent spectrum has an obvious decrease in sp^3 intensity and corresponding increase in sp^2 ‘G’ and ‘D’ intensities.



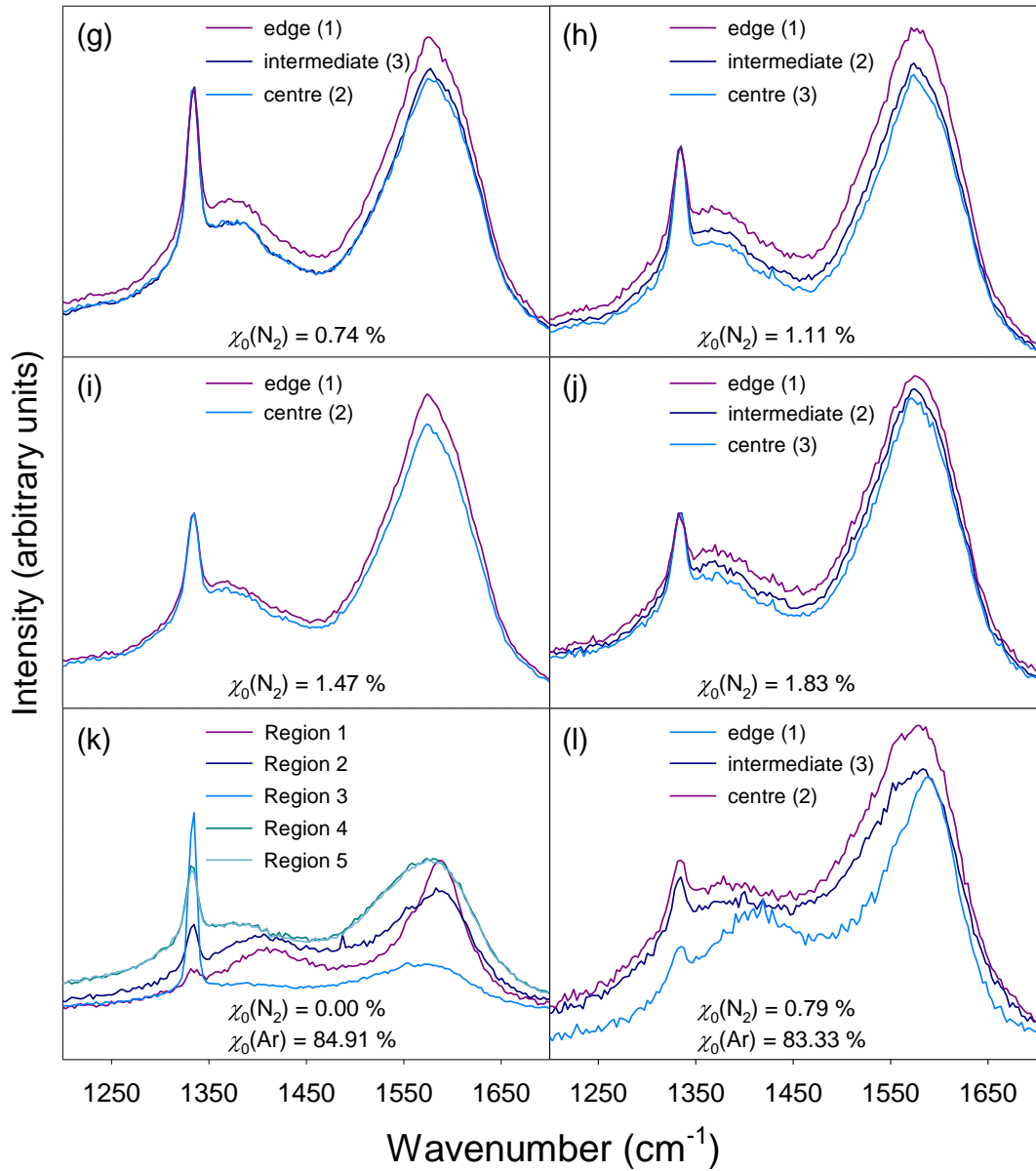
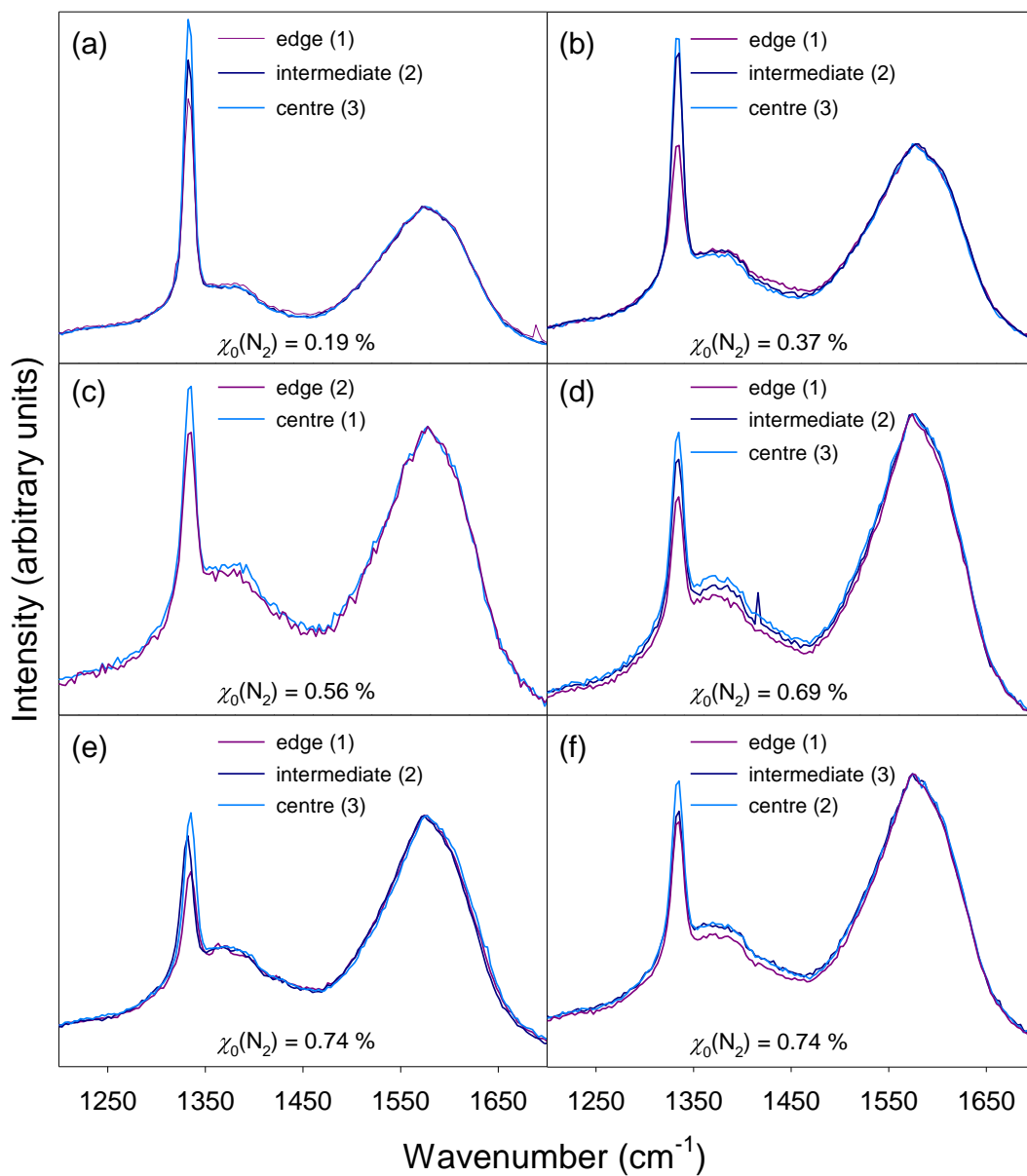


Figure 30: Raman Spectra ($\lambda_{\text{exc}} = 325 \text{ nm}$) for different regions across lens samples grown using 12 different gas mixtures and standard power and pressure conditions. Spectra have been scaled relative to the sp^3 peak. **(a)** $\chi_0(\text{N}_2) = 0.19 \%$ **(b)** $\chi_0(\text{N}_2) = 0.37 \%$ **(c)** $\chi_0(\text{N}_2) = 0.56 \%$ **(d)** $\chi_0(\text{N}_2) = 0.69 \%$ & $\chi_0(\text{Ar}) = 6.90 \%$ **(e)** $\chi_0(\text{N}_2) = 0.74 \%$ **(f)** $\chi_0(\text{N}_2) = 0.74 \%$ **(g)** $\chi_0(\text{N}_2) = 0.74 \%$ (5 mm substrate holder) **(h)** $\chi_0(\text{N}_2) = 1.11 \%$ **(i)** $\chi_0(\text{N}_2) = 1.47 \%$ **(j)** $\chi_0(\text{N}_2) = 1.83 \%$ **(k)** $\chi_0(\text{N}_2) = 0.00 \%$ & $\chi_0(\text{Ar}) = 84.0 \%$ **(l)** $\chi_0(\text{N}_2) = 0.79 \%$ & $\chi_0(\text{Ar}) = 83.3 \%$. The numbers in parenthesis correspond to the photographs (**Figure 28**) showing the regions of the substrate where the spectra were taken.



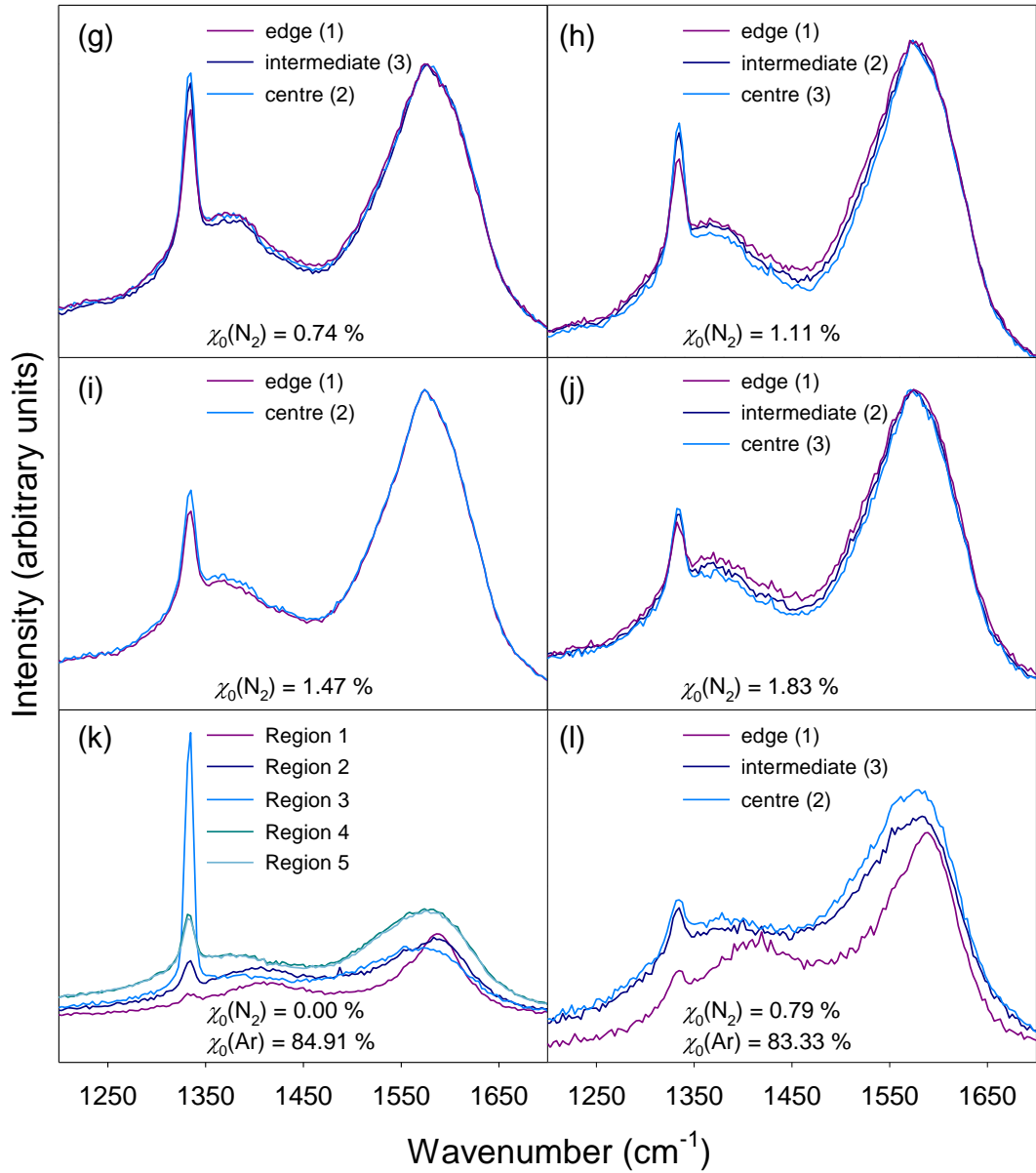


Figure 31: Raman Spectra ($\lambda_{\text{exc}} = 325 \text{ nm}$) for different regions across lens samples grown using 12 different gas mixtures and standard power and pressure conditions. Spectra have been scaled relative to the sp^2 'G' peak. **(a)** $\chi_0(\text{N}_2) = 0.19 \%$ **(b)** $\chi_0(\text{N}_2) = 0.37 \%$ **(c)** $\chi_0(\text{N}_2) = 0.56 \%$ **(d)** $\chi_0(\text{N}_2) = 0.69 \%$ & $\chi_0(\text{Ar}) = 6.90 \%$ **(e)** $\chi_0(\text{N}_2) = 0.74 \%$ **(f)** $\chi_0(\text{N}_2) = 0.74 \%$ **(g)** $\chi_0(\text{N}_2) = 0.74 \%$ (5 mm substrate holder) **(h)** $\chi_0(\text{N}_2) = 1.11 \%$ **(i)** $\chi_0(\text{N}_2) = 1.47 \%$ **(j)** $\chi_0(\text{N}_2) = 1.83 \%$ **(k)** $\chi_0(\text{N}_2) = 0.00 \%$ & $\chi_0(\text{Ar}) = 84.0 \%$ **(l)** $\chi_0(\text{N}_2) = 0.79 \%$ & $\chi_0(\text{Ar}) = 83.3 \%$. The numbers in parenthesis correspond to the photographs **(Figure 28)** showing the regions of the substrate where the spectra were taken.

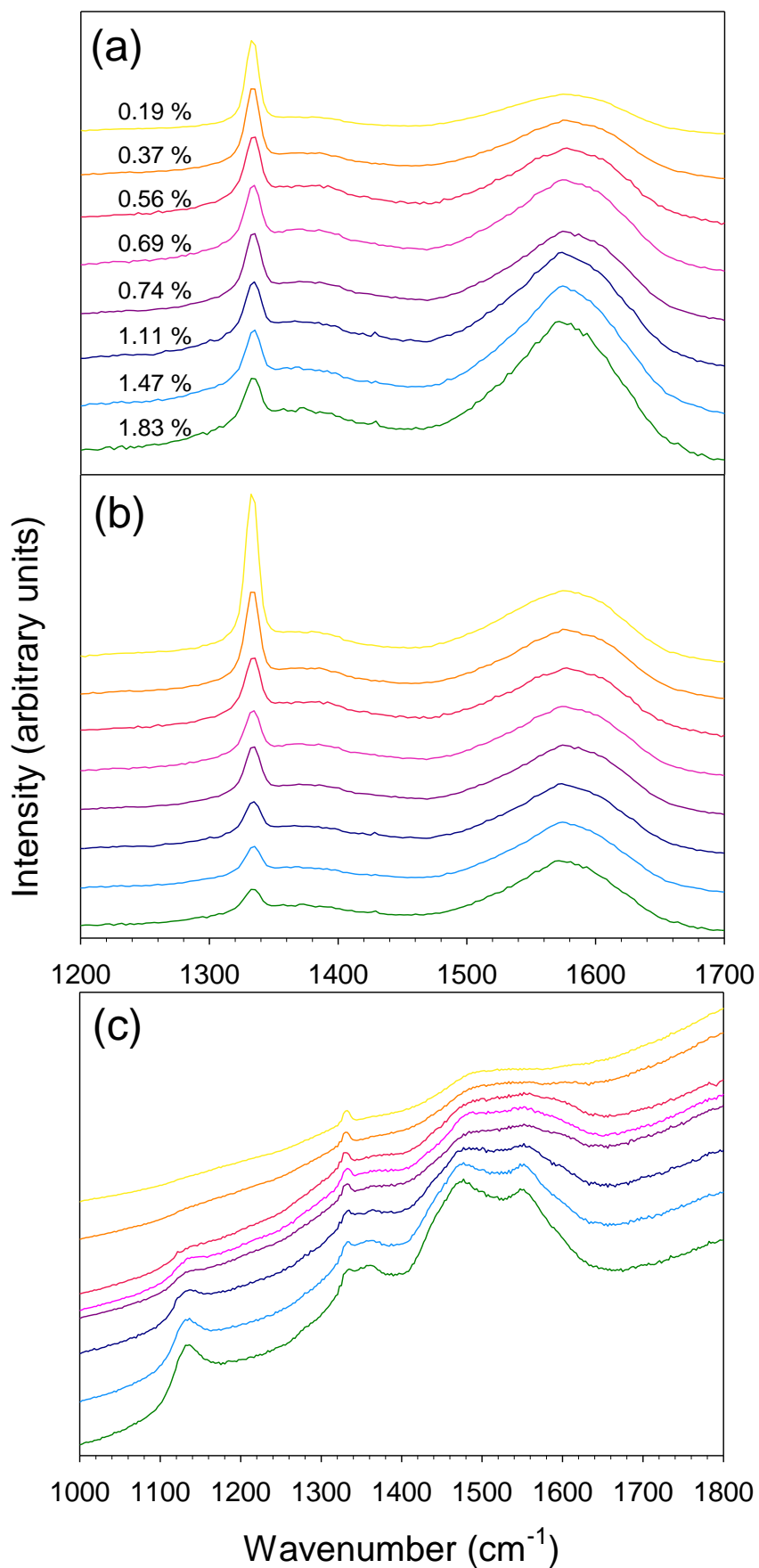


Figure 32: Raman spectra taken at the central position of samples grown at different $\chi_0(\text{N}_2)$ for (a) $\lambda_{\text{exc}} = 325 \text{ nm}$ scaled relative to the sp^3 peak (b) $\lambda_{\text{exc}} = 325 \text{ nm}$ scaled relative to the sp^2 'G' peak (c) $\lambda_{\text{exc}} = 514 \text{ nm}$ normalised to the intensity at the highest wavenumber. The spectra have been offset vertically for ease of display

The UV Raman spectra show that increasing $\chi_0(\text{N}_2)$ reduces the crystal size of the NCD material. This effect is made more obvious by normalising the spectra to different peaks. In **Figure 30** and **Figure 32** the sp^3 peak has been held constant and so the relative changes in the sp^2 ‘G’ peak is enhanced. In **Figure 31** and **Figure 32**, the sp^2 ‘G’ peak is held constant and so the relative change in sp^3 intensity is made obvious.

For a more quantitative analysis, the ratio of peak intensities ($I(sp^3):I(sp^2 \text{ ‘D’})$, $I(sp^3):I(sp^2 \text{ ‘G’})$ and $I(sp^2 \text{ ‘D’}):I(sp^2 \text{ ‘G’})$) for spectra obtained using $\lambda_{\text{exc}} = 325 \text{ nm}$, have been plotted as a function of $\chi_0(\text{N}_2)$ (**Figure 33**). The ratios $I(sp^3):I(sp^2)$ (plots **(a)** and **(b)**) have been fitted with an exponential model. These two graphs show an initial decrease in the ratio between the sp^3 and sp^2 ‘G’ or ‘D’ peaks, but as the concentration is increased above $\sim 1.1 \%$ the ratio starts to level off. This shows that the increase in nitrogen concentration has less influence above a certain value rather than having a linear effect on the $sp^3:sp^2$ character and, hence, crystal size. Above $\chi_0(\text{N}_2) \sim 1.1 \%$ a further increase in $\chi_0(\text{N}_2)$ will not have a noticeable influence on the morphology of the films produced.

As both the ‘G’ and ‘D’ peaks both originate from the sp^2 -hybridised carbon, there should be little, or no, variation in their intensity ratio and this is confirmed in plot **(c)** where no trend is seen as $\chi_0(\text{N}_2)$ is increased, and the ratio remains roughly constant.

Sample **d** ($\chi_0(\text{N}_2) = 0.69 \%$), grown using standard conditions but with a small amount of argon added to the process gas mixture, shows similar spectra and intensity ratios to the films grown without Ar. Therefore, the addition of Ar was not seen to have an effect on the quality and morphology of the diamond and was not used in later depositions.

As well as the variation in the sp^3/sp^2 character from sample to sample, a slight variation in the quality across the surface each sample from the edge to the centre is observed. The observation that a more intense sp^2 ‘G’ peak (or less intense sp^3 peak) is recorded at the edge of the sample compared with the centre holds true for all the samples grown. It can therefore be inferred that the crystallite sizes are slightly larger in the centre of the lens substrates as the degree of sp^3 -character is higher due to a decrease in the grain boundary surface area. It should be noted that this difference in quality is subtle and less significant than the difference in quality from sample to sample grown with varied $\chi_0(\text{N}_2)$. The shape and position of the MWCVD plasma is, in part, determined by the dimensions of the molybdenum substrate holder and the plasma tends to latch onto the side of the holder. The diameter of the substrate holder is 30 mm which means that the edge of the lens moulds are closer to the periphery of the plasma. This part of the plasma will have a different temperature and gas-phase composition to that nearer the centre, and will result in small changes in the rates of deposition and etching processes leading to the slight non-uniformity across the sample.

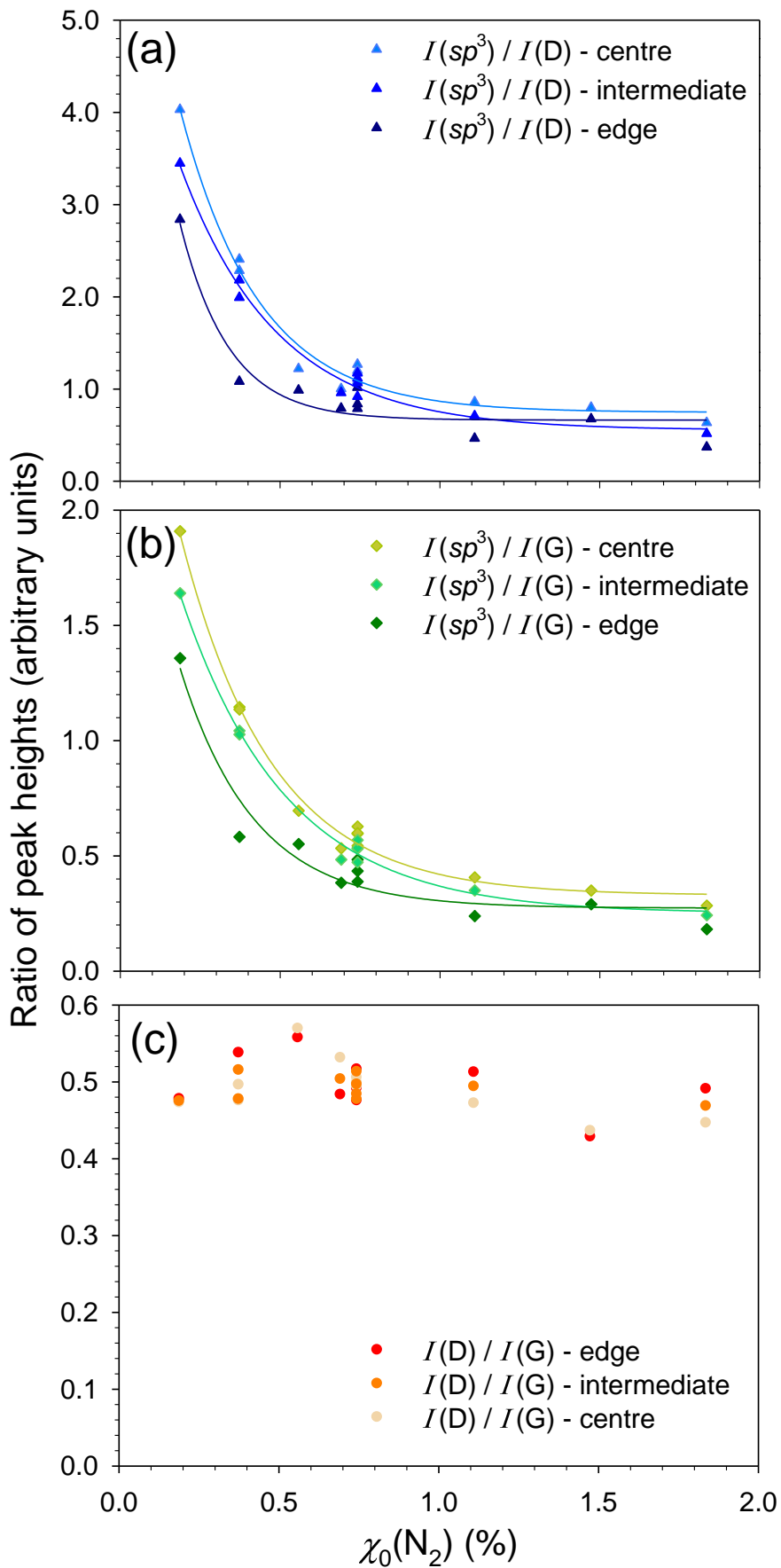
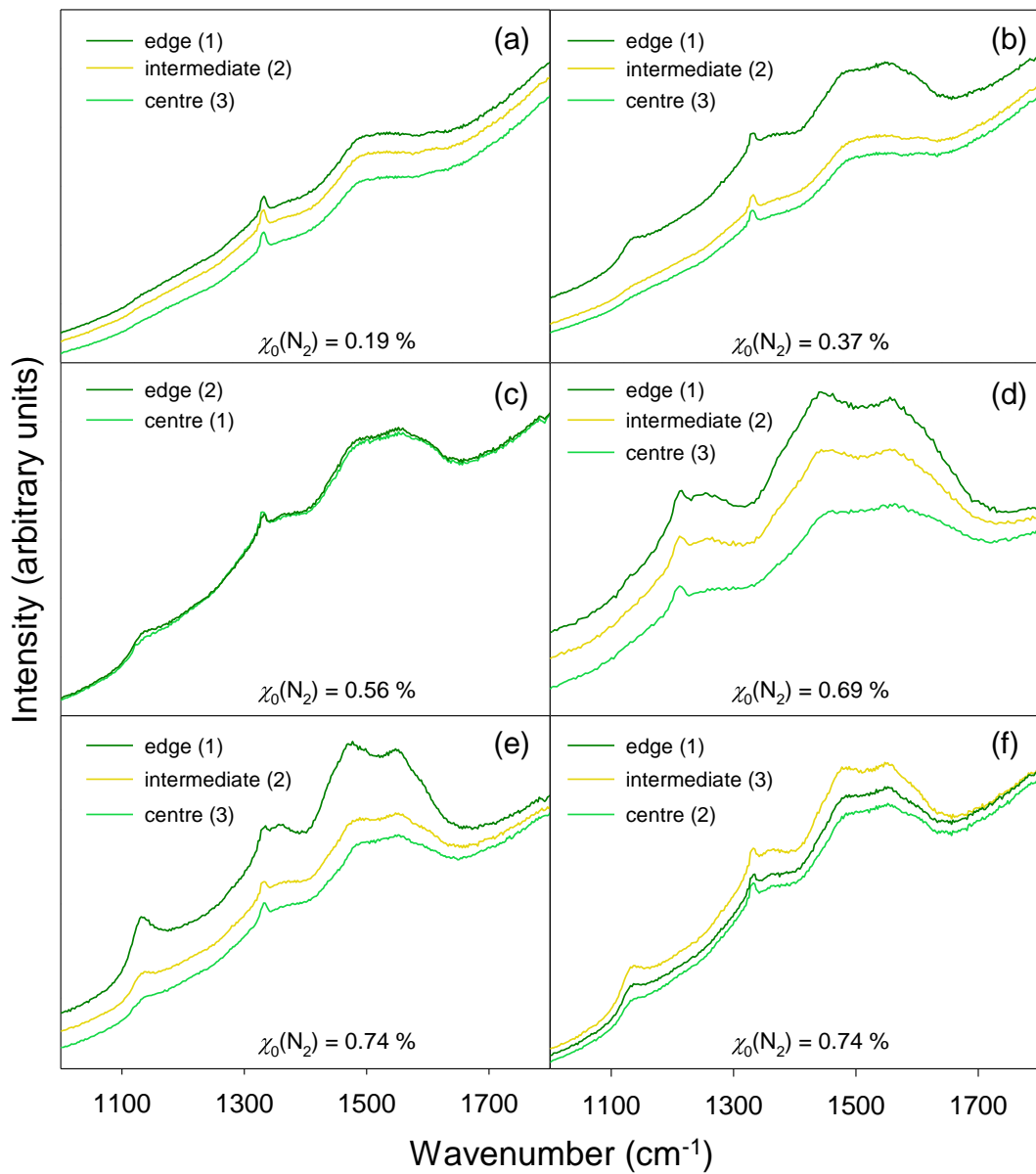


Figure 33: Collated intensity ratios from Raman spectra (a) $I(sp^3) : I(sp^2 \text{ 'D' })$ (b) $I(sp^3) : I(sp^2 \text{ 'G' })$ (c) $I(sp^2 \text{ 'D' }) : I(sp^2 \text{ 'G' })$ as a function of $\chi_0(\text{N}_2)$ at edge, intermediate and central positions on the samples.

The Raman spectra and photographs for samples **k** and **l** show that the depositions using an Ar-rich plasma were not successful. Sample **k** was grown with no nitrogen present and the film is markedly non-uniform with regions of the lens that are coated with a-C or non-diamond deposits and others with high quality CVD diamond growth. The Raman spectra for the different regions reflect this observation with one exhibiting a high intensity sp^3 -carbon peak and much lower intensity sp^2 -carbon peaks indicating high-quality microcrystalline diamond. Conversely, other spectra hardly display a sp^3 -carbon peak at all and correspond to the regions of a-C. Sample **l** is slightly more uniform although the Raman spectra show that there are still non-diamond regions dominated by sp^2 -carbon material and the chip is not of sufficient quality to create a diamond lens. Due to the poor uniformity, low quality and slow growth rate of these depositions using argon was not further investigated.

The green Raman spectra ($\lambda_{\text{exc}} = 514 \text{ nm}$) for the twelve samples are displayed in **Figure 34** where for ease of comparison the spectra have been normalised with respect to the intensity at the highest wavenumber value. In the green Raman spectra the sp^3 diamond peak is less varying between samples however information on the degree of non sp^3 -bonded carbon can be investigated. In sample **a** ($\chi_0(\text{N}_2) = 0.19 \%$), the spectral features are relatively smooth; the sp^3 diamond peak and the sp^2 ‘G’ peak are the most noticeable, with the ‘D’ peak at low intensity and a small broad peak at $\sim 1150 \text{ cm}^{-1}$. As $\chi_0(\text{N}_2)$ is increased (samples **b – j**), the peak at $\sim 1150 \text{ cm}^{-1}$ increases in intensity, the ‘D’ peak becomes dominant over the sp^3 diamond peak and the ‘G’ peak appears to have split into two peaks (~ 1480 and 1550 cm^{-1}). The peaks at $\sim 1150 \text{ cm}^{-1}$ and $\sim 1480 \text{ cm}^{-1}$ are the ‘ T_{v1} ’ and ‘ T_{v3} ’ *trans*-polyacetylene peaks. *Trans*-polyacetylene is found at grain boundaries of diamond CVD thin films. Decreasing the crystallite size increases the grain boundary surface area and thus the amount of *trans*-polyacetylene in the films. The intensity of the *trans*-polyacetylene peaks increase with $\chi_0(\text{N}_2)$, supporting the result from the UV Raman spectra that crystallite size decreases with increasing $\chi_0(\text{N}_2)$.

Sample **k** was carried out in an argon-rich plasma with no nitrogen present. Despite the variation in the quality across the film, there are no ‘ T_{v1} ’ or ‘ T_{v3} ’ peaks present. This indicates that the film is microcrystalline. The absence of nitrogen prevents the crystallites from becoming nanocrystalline, maintaining a smaller grain boundary surface area and reducing the amount of *trans*-polyacetylene in the deposited diamond film.



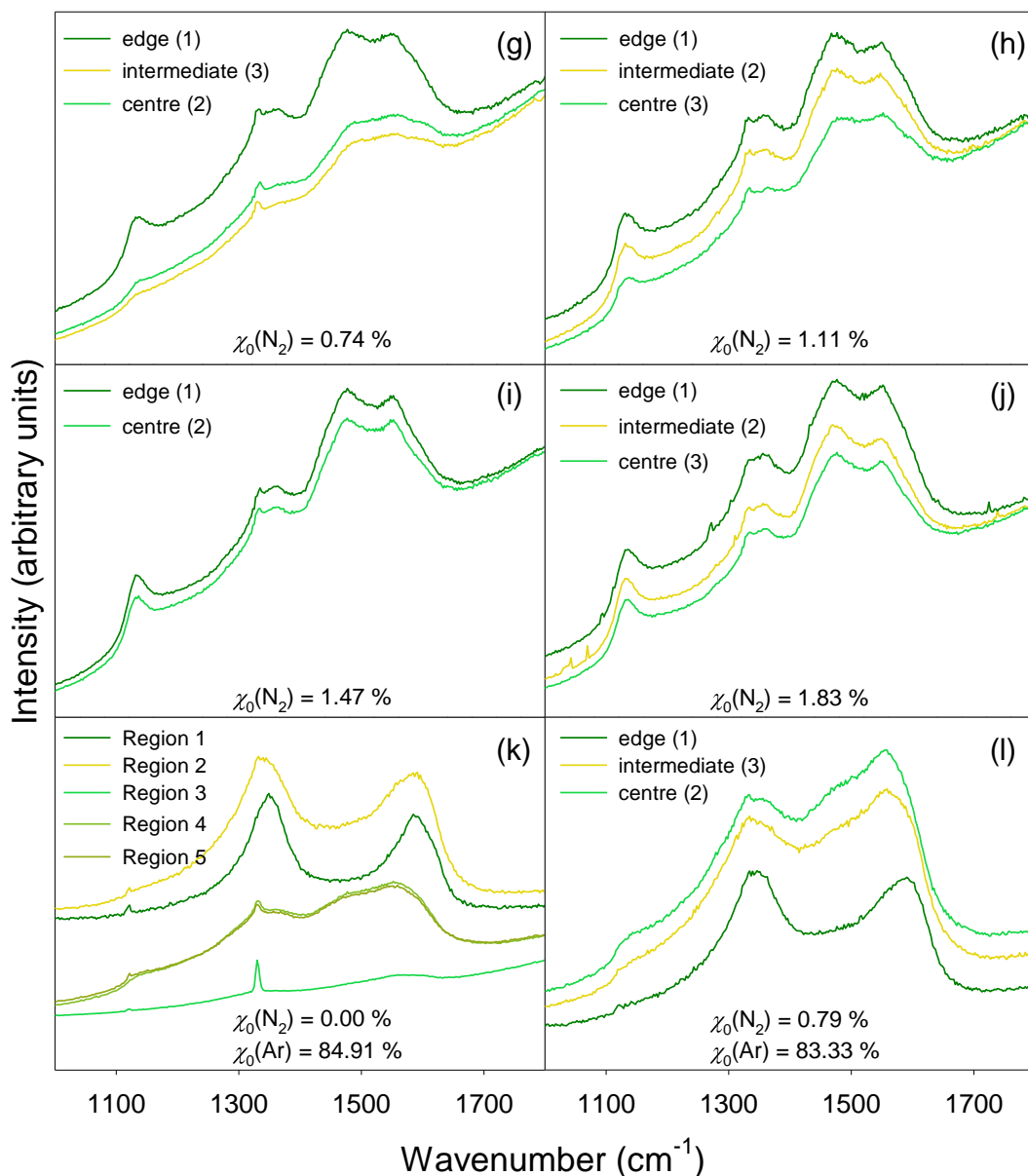


Figure 34: Raman Spectra ($\lambda_{\text{exc}} = 514 \text{ nm}$) for different regions across lens samples grown using 12 different gas mixtures and standard power and pressure conditions. Spectra have been scaled relative the intensity at the highest wavenumber. **(a)** $\chi_0(\text{N}_2) = 0.19 \%$ **(b)** $\chi_0(\text{N}_2) = 0.37 \%$ **(c)** $\chi_0(\text{N}_2) = 0.56 \%$ **(d)** $\chi_0(\text{N}_2) = 0.69 \%$ & $\chi_0(\text{Ar}) = 6.90 \%$ **(e)** $\chi_0(\text{N}_2) = 0.74 \%$ **(f)** $\chi_0(\text{N}_2) = 0.74 \%$ **(g)** $\chi_0(\text{N}_2) = 0.74 \%$ (5 mm substrate holder) **(h)** $\chi_0(\text{N}_2) = 1.11 \%$ **(i)** $\chi_0(\text{N}_2) = 1.47 \%$ **(j)** $\chi_0(\text{N}_2) = 1.83 \%$ **(k)** $\chi_0(\text{N}_2) = 0.00 \%$ & $\chi_0(\text{Ar}) = 84.0 \%$ **(l)** $\chi_0(\text{N}_2) = 0.79 \%$ & $\chi_0(\text{Ar}) = 83.3 \%$. The numbers in parenthesis correspond to the photographs (**Figure 28**) showing the regions of the substrate where the spectra were taken.

Quantitative analysis was carried out on the ‘T₀₁’ peak to see how the intensity varied with $\chi_0(\text{N}_2)$ (**Figure 35**). A curved background was fitted and subtracted from each spectrum. The intensities analysed were from the centre of the samples as this represents the diamond morphology responsible for focusing the x-ray beam. It was not possible to investigate the ‘T₀₃’ peak as there is too much overlap with the sp^2 ‘G’ peak. It shows that the peak intensity increases linearly with $\chi_0(\text{N}_2)$ in the range investigated showing an increase in the amount of *trans*-polyacetylene present in the deposited diamond. **Figure 35** displays the absolute intensities of *trans*-polyacetylene, as opposed to intensity-ratios as in **Figure 33** which may explain why the *trans*-polyacetylene analysis shows a linear relationship $\chi_0(\text{N}_2)$ as opposed to an exponential-type dependence.

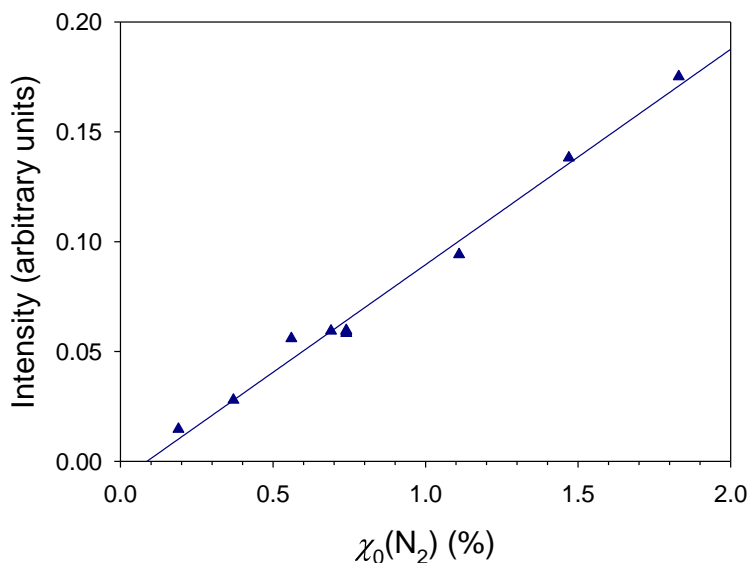


Figure 35: Intensity of the ‘T₀₁’ Raman peaks ($\lambda_{\text{exc}} = 514 \text{ nm}$) from the sample centres as a function of $\chi_0(\text{N}_2)$. A curved background had been taken from the data before performing the fitting.

6.1.2 Growth Rate and Electron Microscopy

In order to reduce the focal-width of the lenses grown by the silicon mould/diamond CVD method to $< 400 \text{ nm}$, the filling of the lens mould needs to be improved such that, when grown in order for testing at DLS, the film thickness in the recessed areas is $> 50 \mu\text{m}$. For $< 50 \mu\text{m}$ the sidewalls of the lens structure form internal surfaces which scatter the x-rays, limiting the possible focal-width size. A diamond filling of $> 50 \mu\text{m}$ would reduce the extent of beam slitting resulting in the focused beam having a higher intensity.

The kinoform lenses have higher aspect ratios than the CRLs and so it was important to determine how the diamond was depositing into these new lens designs and whether $\chi_0(\text{N}_2)$ would affect the mould filling. As previously mentioned, $\chi_0(\text{N}_2)$ is known to increase the growth rate. However, this is when the deposition occurs onto a two-dimensional substrate and so it was necessary to see the influence of $\chi_0(\text{N}_2)$ when diamond is being deposited over the three-dimensional structures. Each deposition was carried out for

$t = 10$ h, as this was long enough to indicate how each different aspect-ratio trench would fill over time. When a free-standing lens substrate for testing at the synchrotron is produced the deposition time was > 18 h.

While Raman spectroscopy is able to give insights into the quality of the diamond and the dominant bonding state of carbon it cannot show how well the diamond filled the mould. Instead, electron microscopy of the lens substrates viewed in cross-section was used in order to determine the success of each deposition. Using a graphics program called *Inkscape* (<http://inkscape.org/>), measurements were made of the film thickness at different positions on the mould and of the trench width. **Figure 36a** is a schematic diagram of a lens cross-section with the different dimensions labelled and **Figure 36b** shows how these were determined using *Inkscape*.

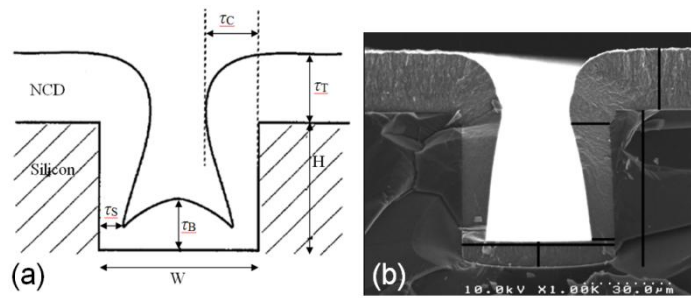


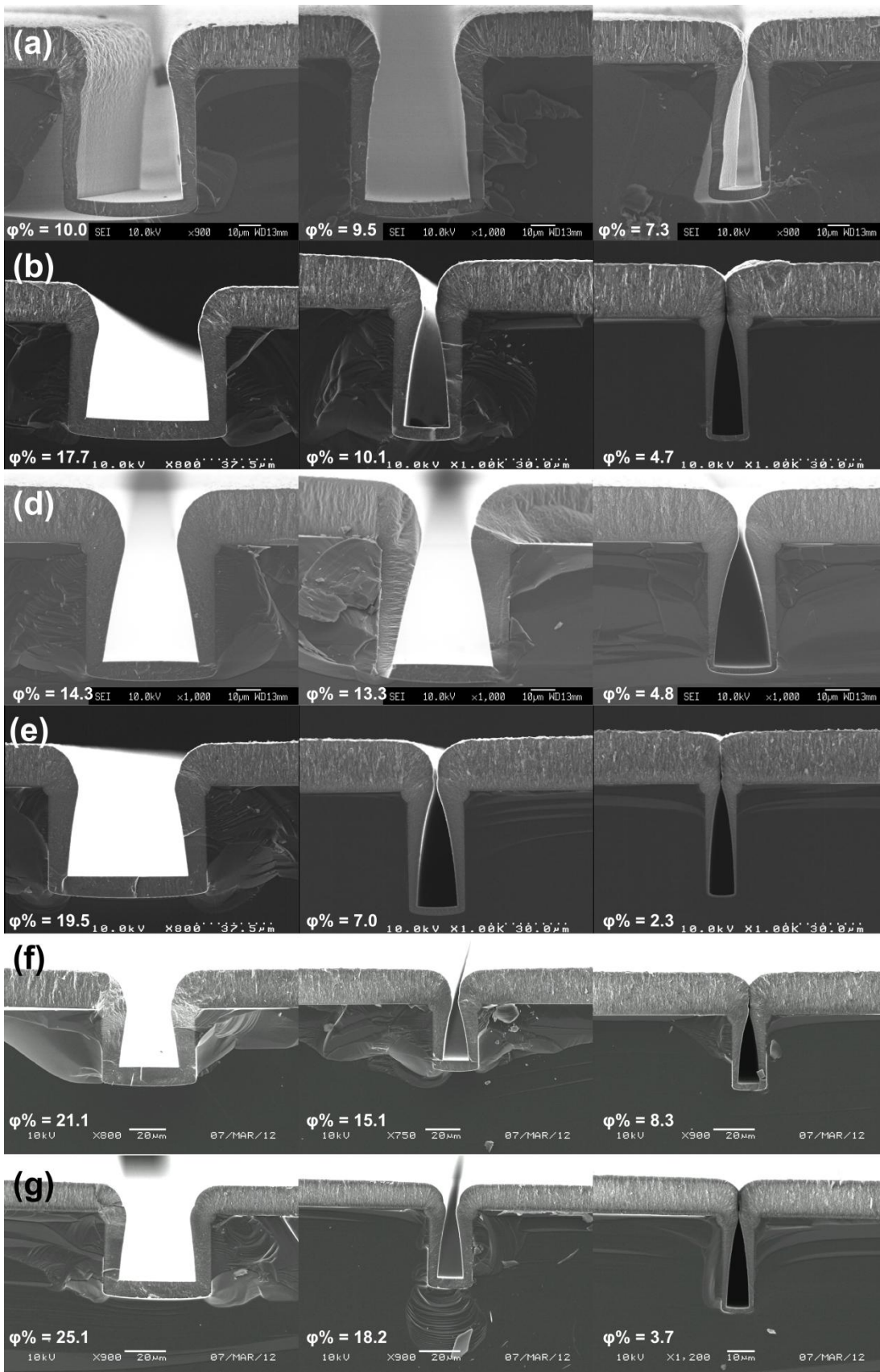
Figure 36: (a) schematic diagram of lens cross-section with the different dimensions labelled: W = trench width, H = trench height, τ_T = NCD film thickness on top surface, τ_B = NCD film thickness at bottom of trench, τ_C = NCD film on the top corners, τ_S = NCD film thickness at the base of the sidewalls (b) SEM cross-section of lens showing analytical measurements taken.

It was found that the top surface of the lens (τ_T) grew at a faster rate than in the base of the trench (τ_B). This is believed to be because the recessed surfaces are further from the plasma and have a lower incident flux of the reactive species responsible for diamond growth. The top surface will also be at a higher temperature and so the rate of deposition will be higher. The anisotropic nature of the growth rates due to these effects led to overgrowth of the top corners (τ_C), termed ‘cusping’ and this problem was addressed in subsequent depositions. A quantitative value for the ‘cusping factor’, κ , (**Equation 5**) $\kappa = \frac{\tau_C - \tau_S}{\tau_S}$ allowed comparison between deposition conditions. For each lens mould the percentage of filling, $\phi\%$, of the diamond in the recessed areas was calculated using **Equation 6**.

$$\kappa = \frac{\tau_C - \tau_S}{\tau_S} \quad \text{Equation 5}$$

$$\phi\% = 100 \times \frac{\tau_B}{H} \quad \text{Equation 6}$$

$$\text{aspect ratio} = \frac{\text{trench height}}{\text{trench width}} = \frac{H}{W} \quad \text{Equation 7}$$



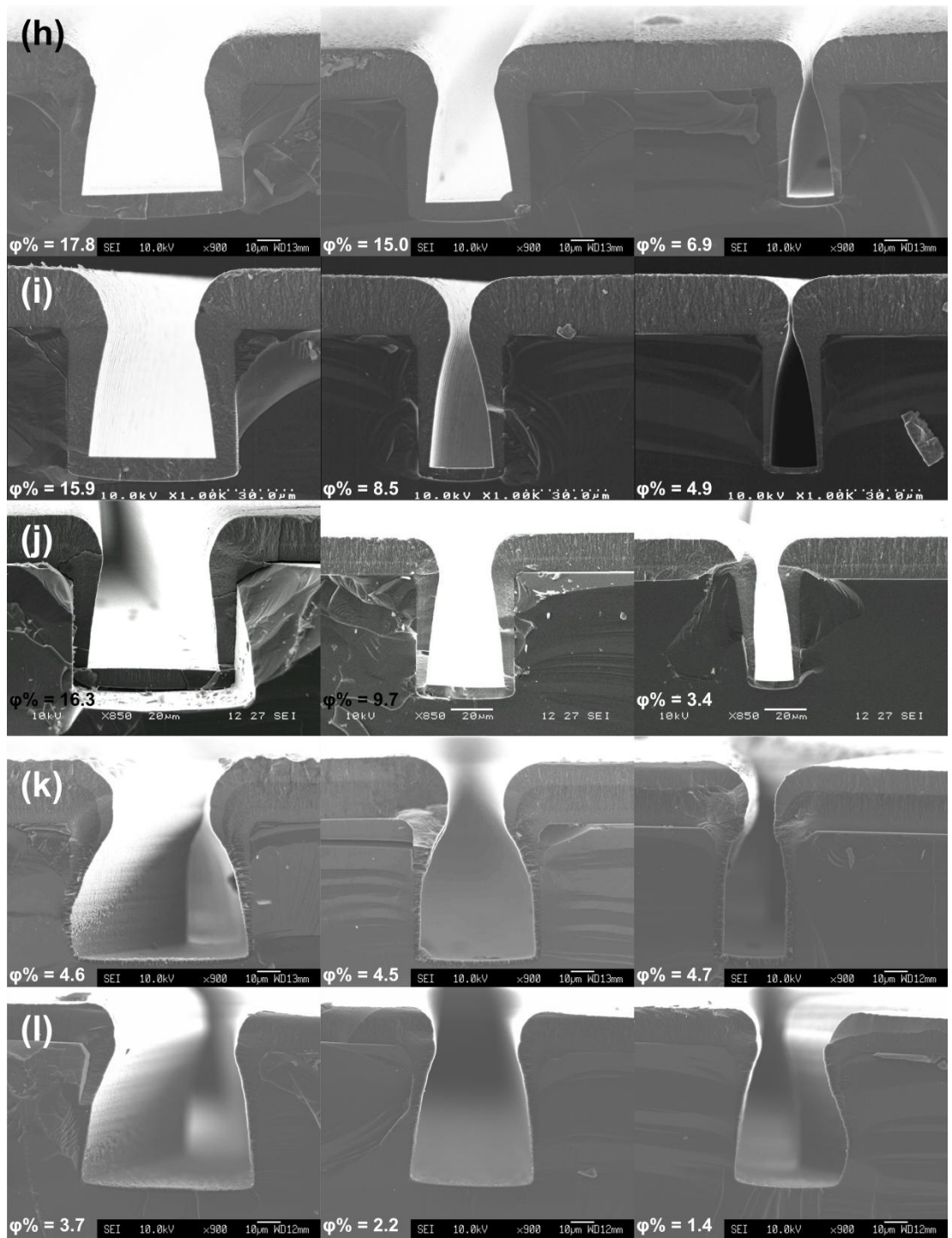


Figure 37: Cross-sectional SEM images of lenses **a - l** at three different aspect ratios displaying the accompanying $\phi\%$. (**a**) $\chi_0(\text{N}_2) = 0.19\%$ (**b**) $\chi_0(\text{N}_2) = 0.37\%$ (**c**) $\chi_0(\text{N}_2) = 0.56\%$ (**d**) $\chi_0(\text{N}_2) = 0.69\%$ & $\chi_0(\text{Ar}) = 6.90\%$ (**e**) $\chi_0(\text{N}_2) = 0.74\%$ (**f**) $\chi_0(\text{N}_2) = 0.74\%$ (**g**) $\chi_0(\text{N}_2) = 0.74\%$ (5 mm substrate holder) (**h**) $\chi_0(\text{N}_2) = 1.11\%$ (**i**) $\chi_0(\text{N}_2) = 1.47\%$ (**j**) $\chi_0(\text{N}_2) = 1.83\%$ (**k**) $\chi_0(\text{N}_2) = 0.00\%$ & $\chi_0(\text{Ar}) = 84.0\%$ (**l**) $\chi_0(\text{N}_2) = 0.79\%$ & $\chi_0(\text{Ar}) = 83.3\%$. The growth conditions are summarised in **Table 1**. All lenses have $H = 50\ \mu\text{m}$ with exception of samples **f** and **g** for which $H = 30\ \mu\text{m}$.

Figure 37 shows cross-sectional SEM images for each deposition run at a range of aspect ratios to demonstrate how it affects the filling of the moulds. Accompanying this figure is **Table 2** which relates the type of lens design and the $\chi_0(\text{N}_2)$ to the filling factor, $\phi\%$, and the cusping factor, κ . The $\phi\%$ for samples **f** and **g** are misleading as they are higher than the other samples. This is not because the deposition conditions are more successful, but

because the trench height was 20 μm less than the other lens samples. The film thickness obtained remained of similar order to the other lens samples.

Table 2: Comparing the type of lens, $\chi_0(\text{N}_2)$ and the aspect ratio with the $\phi\%$ and κ for samples **a - l**. Sample **c** was not investigated in this section. $H= 50 \mu\text{m}$ for all samples with exception of samples **g** and **h** ($H = 30 \mu\text{m}$).

Sample	$\chi_0(\text{N}_2)$ (%)	Type of lens	Aspect Ratio	$\phi\%$ (%)	κ
a	0.19	CRL	1.11	10.0	0.79
			1.20	9.5	0.99
			2.28	7.3	1.38
b	0.37	kinoform	0.72	17.7	0.50
			1.90	10.1	1.14
			2.87	4.7	2.31
d	0.69	kinoform	1.06	14.3	1.19
			1.10	13.3	1.50
			1.92	4.8	3.90
e	0.74	kinoform	0.71	19.5	0.50
			1.77	7.0	1.83
			3.56	2.3	4.33
f	0.74	kinoform	0.83	21.1	0.63
		30 μm	1.56	15.1	1.00
			1.96	8.3	2.16
g	0.74	kinoform	0.80	25.1	0.37
		30 μm	1.79	18.2	0.38
			2.29	3.7	1.74
h	1.11	kinoform	0.72	17.8	0.57
			1.04	15.0	0.73
			1.85	6.8	1.76
i	1.47	kinoform	0.91	15.9	0.31
			1.70	8.5	1.90
			2.34	4.9	2.74
j	1.83	CRL	0.79	16.3	0.64
			1.25	9.7	1.03
			2.09	3.4	2.17
k	0	CRL	0.80	4.6	5.89
	$\chi_0(\text{Ar}) = 84.91$		1.11	4.5	2.75
			1.67	4.7	0.84
l	0.79	CRL	0.86	3.7	6.34
	$\chi_0(\text{Ar}) = 83.33$		1.14	2.2	6.43
			1.35	1.4	6.00

For the depositions using Ar-rich plasmas (samples **k** and **l**) the photographs **Figure 28** and Raman spectra (**Figure 30, 31, and 34**) showed that the uniformity and diamond quality was poor. Likewise, the SEM cross-sections (**Figure 37**) indicate that the diamond deposition rate in the trench regions is very low. For these samples grown in the argon-rich plasma, two distinct layers ('bands') in the diamond film are also observed. As deposition runs were carried out in two parts ($t_1 = 6$ h, $t_2 = 4$ h) it is assumed that the observed banding is due to the plasma being restarted on consecutive days. The substrate was kept under vacuum and never exposed to air in between the two depositions. This banding is only seen in the Ar-rich plasma samples and so the reason for this effect is likely to be a result of reduced hydrogen in the plasma. For samples **a – j**, the start and end of each deposition is a pure hydrogen plasma ($\chi_0(\text{H}_2) = 100\%$), so the surface can be cleaned up (cf. **Section 3.2.1**). For samples **k** and **l**, the concentration of hydrogen in the plasma is lower so banding arises when the growth is carried out by a number of deposition runs.

A trend that is common for every deposition is that τ_T is thicker than τ_B , as already mentioned. While the diamond thickness on the top surface remains constant as the trench width is decreased, the film thickness in the trench areas decreases. By looking at kinoform lenses of identical design, the effect of $\chi_0(\text{N}_2)$ on the lens filling is compared (**Figure 38**). For the widest trenches, the growth rate in the trench remains lower than that of the top surface. The figure also shows that the film thickness in each region is not obviously affected by $\chi_0(\text{N}_2)$.

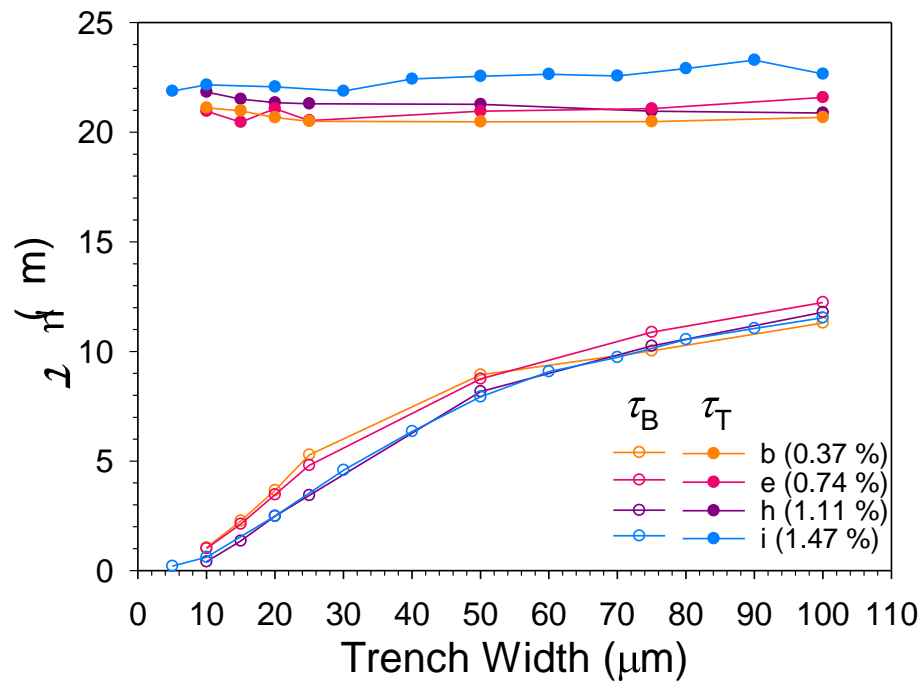


Figure 38: The thickness of the deposited NCD on the top surface (filled symbols) and the recessed areas (open symbols) for five kinoform lenses ($H = 50\ \mu\text{m}$) at varying $\chi_0(\text{N}_2)$ as a function of the trench width.

In order to make comparisons between all the lens samples and to find a deposition method that can be used on any lens design, the filling in the trench needs to be analysed with respect to the aspect ratio (**Equation 7**), as opposed to trench width. The film thickness in recessed areas and κ are plotted as a function of aspect ratio in **Figure 39**. Despite the expectation that $\chi_0(\text{N}_2)$ would affect the growth rate and hence the filling of the moulds, little variation is seen between the different deposition conditions, it is solely the aspect ratio that affects the filling of the trenches. A cusping factor of zero corresponds to a uniform thickness for the entire sidewall, and so a low κ corresponds to better filling of the lens mould. The cusping factor is also affected by aspect ratio as opposed to $\chi_0(\text{N}_2)$.

The results for both τ_B and κ for the samples grown under standard conditions (samples **e**, **f** and **g**) are the same despite the trench height in the former being deeper. This shows the repeatability of this MWCVD method and how the filling is dependent on the aspect ratio, and not just the trench width.

It has been shown that although $\chi_0(\text{N}_2)$ has an effect on the morphology of the deposited diamond in the range investigated, the growth rate is not affected. There is a substantial difference in growth rate between τ_T and τ_B which results in an overhang of the NCD deposited at the corners of the lens mould. For high aspect ratio samples, this overhang inhibits the flux of growth species incident on the lower surface thus decreasing the deposition rate. A better filling of these lens moulds is required before growing the samples for $t_{\text{growth}} \geq 18$ h. For the kinoform-design moulds the aspect ratios are much higher as the lens thickness is smaller than the CRL design. As such, it is crucial to find a way to prevent the top-surface growth from hindering the deposition in the recessed areas. This was the focus of the second part of this project (**Section 6.2**).

Because $\chi_0(\text{N}_2)$ did not affect the filling of the lens, $\chi_0(\text{N}_2) = 0.74\%$ will be used in the second part of this project as it is currently believed to be the appropriate crystallite size for reduced scattering while preserving the bulk diamond properties.

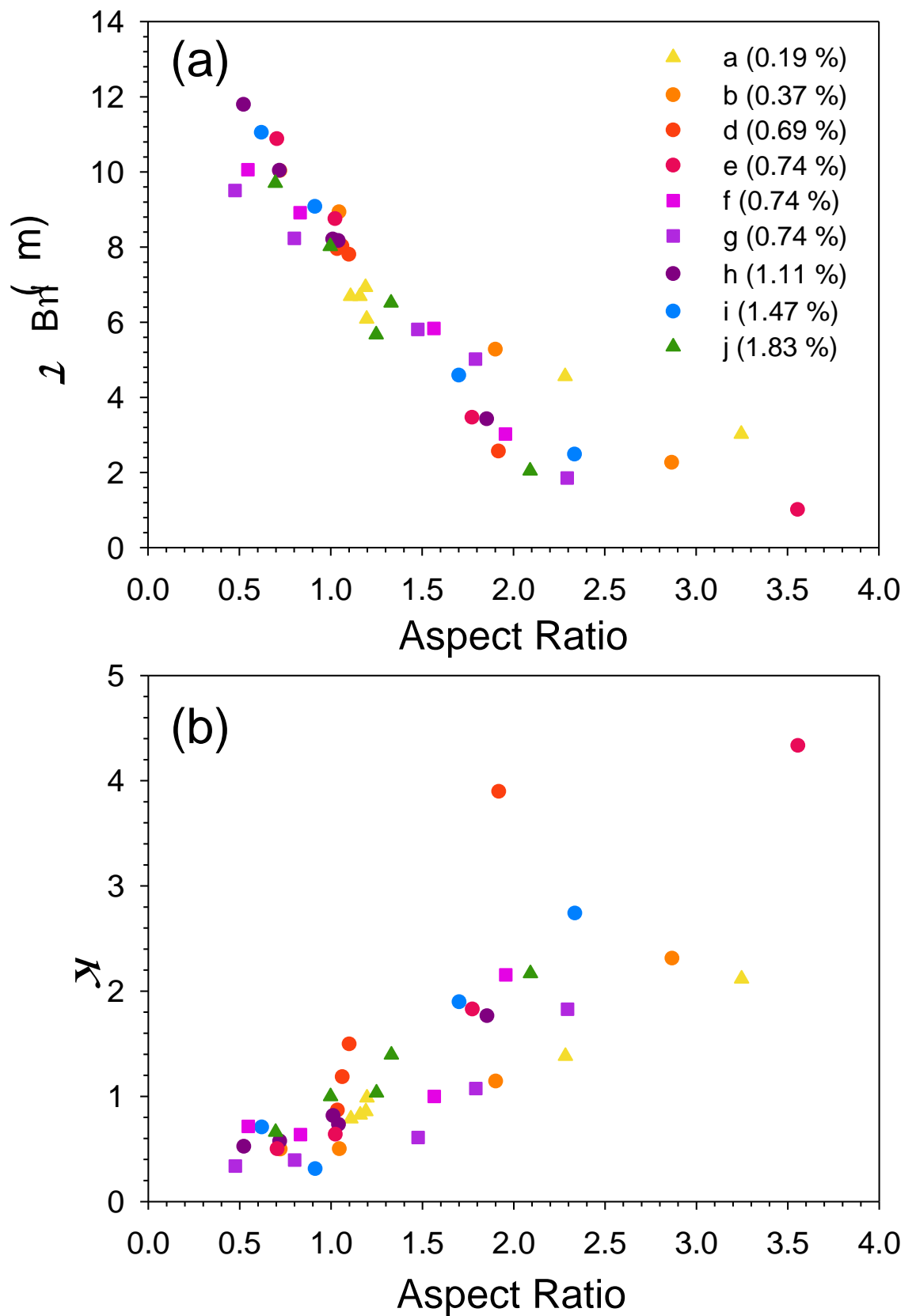


Figure 39: (a) τ_B and (b) κ as a function of aspect ratio for samples a–j ($\chi_0(N_2) = 0.19 - 1.83\%$). Conditions are summarised in **Table 1**.

6.1.3 Optical Emission Studies of the Plasma

After the effect of $\chi_0(\text{N}_2)$ on the morphology of the grown film and the growth rate was investigated, the effect of $\chi_0(\text{N}_2)$ on the plasma was studied. OES was used in order to probe changes in plasma environment across the $\chi_0(\text{N}_2)$ range used in this project. Seven spectra were measured in the range $\chi_0(\text{N}_2) = 0.19 - 3.67\%$, and the spectral intensities of peaks for four emitting species were analysed (CN, C₂, CH and H). An example of the full spectrum measured is shown in **Figure 40**, with details of the observed spectral bands summarised in **Table 3**. The spectrum has been displayed in two sections due to the strong H _{α} peak otherwise dominating over the other spectral features. **Figure 40** shows spectral bands for the molecular species (CN, CH and C₂) and sharp peaks for the atomic species (H). The increase in structure is due to polyatomic species have a greater number of degrees of freedom (from vibrational and rotational energy) than atomic species which have only translational energy. For polyatomic species, when there is no change in the J rotational quantum number ($\Delta J = 0$) for a particular transition, the band-head obtained is termed the ‘Q-branch’, while $\Delta J = +1, -1$ are termed the R- and P- branches, respectively.^[73]

Table 3: Details of the spectral bands present in the optical emission spectra detected. v'' and v' are the ground and excited state vibrational quantum numbers respectively and $\Delta v = v' - v''$.^[74]

Species	System	Symbols	Branch type	Wavelength (nm)	v''	v'	Δv
CN	Violet	$B^2\Sigma - X^2\Sigma$	Q-head	388.3	0	0	0
	System			421.6	1	0	-1
CH	Å	$A^2\Delta - X^2\Pi$	Q-head	431.4	0	0	0
	System						
C ₂	Swan	$A^3\Sigma_g - X'^3\Sigma_u$	Q-head	473.7	0	1	1
	System			516.5	0	0	0
					563.6	1	0
H	Balmer	H _{α} ($n=3 - n=2$)	-	656.3	-	-	-
	Series	H _{β} ($n=4 - n=2$)		486.1			
		H _{γ} ($n=5 - n=2$)		434.4			

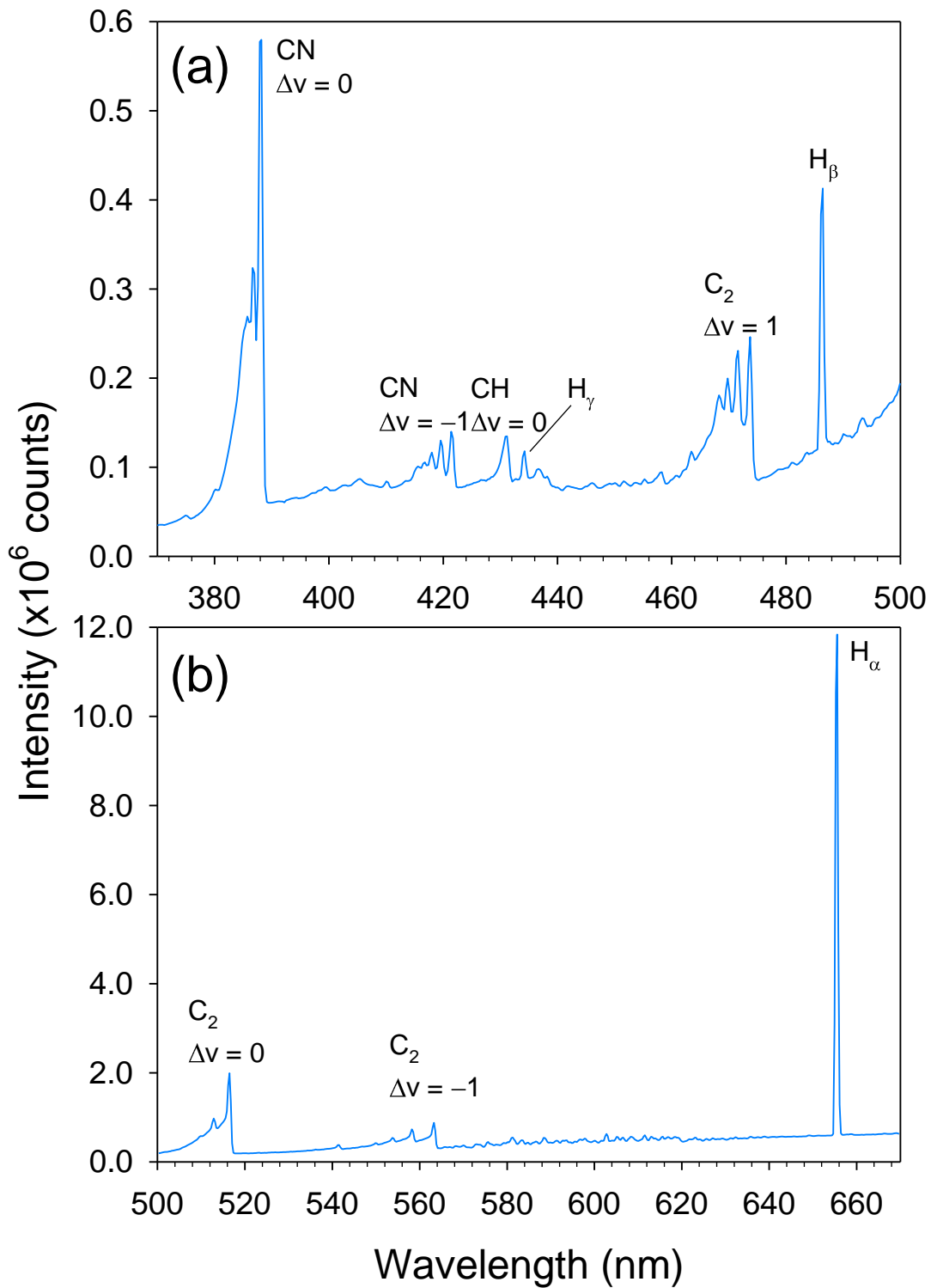


Figure 40: Example of an optical emission spectrum indicating the observed radical species bands. The spectrum was taken using $\chi_0(\text{N}_2) = 3.67\%$.

6.1.3.1 CN

A linear increase in the intensity of the CN 388 and 421 nm band-heads was found as $\chi_0(\text{N}_2)$ was increased. Even at low $\chi_0(\text{N}_2)$ the CN peak was clearly present in the emission spectra indicating that only a small amount of $\chi_0(\text{N}_2)$ is required to have an effect on the plasma environment. This observation supports the results for the lenses grown at the range of

nitrogen concentrations where only a small range of $\chi_0(\text{N}_2)$ produced a large range of material morphology.

The intensity of the CN 388 nm band was always higher than the 421 nm band. This is due to the former corresponding to a $\Delta v = 0$ transition which have the highest probabilities for diatomic species.^[75]

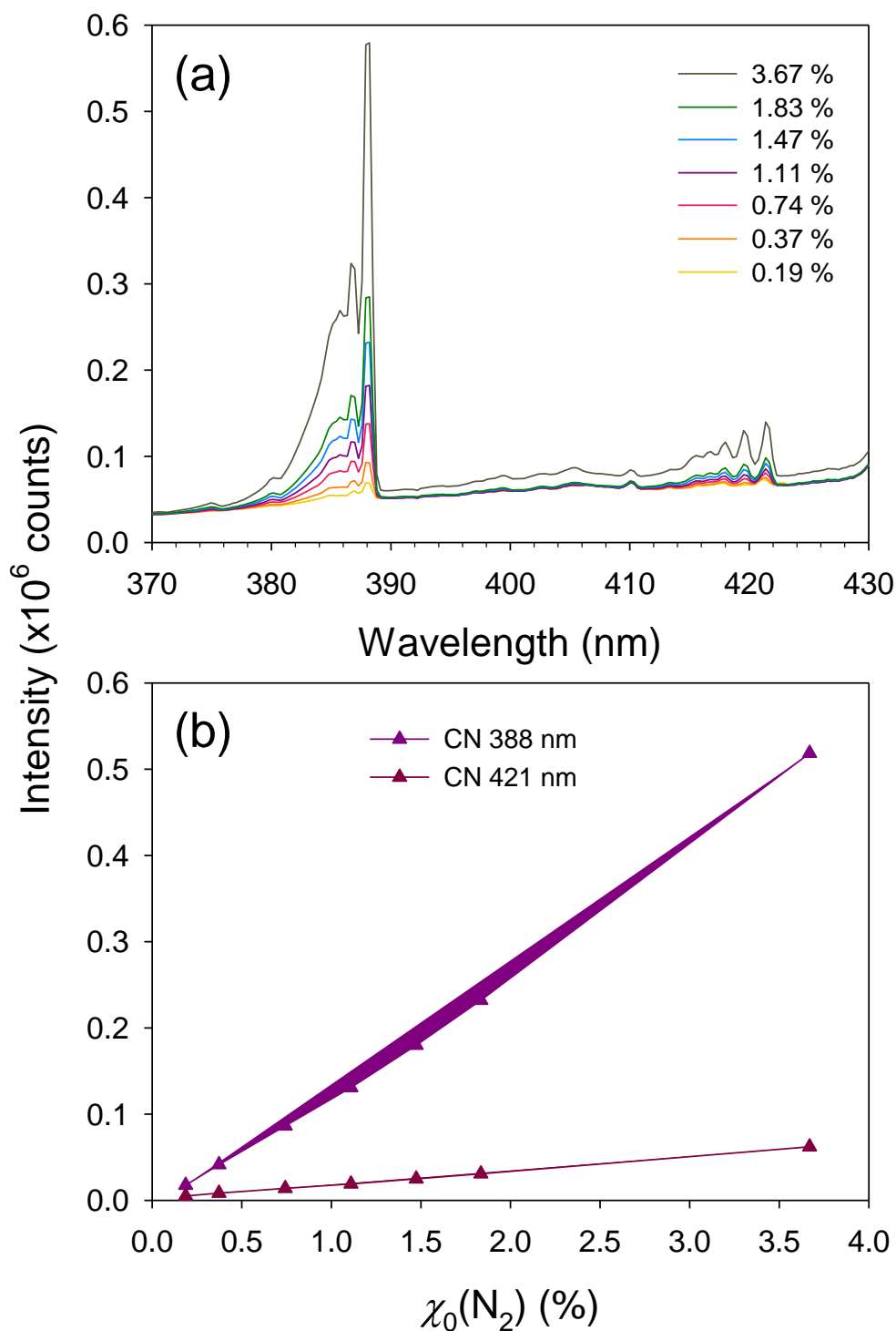


Figure 41: (a) OES for both CN bands for $\chi_0(\text{N}_2) = 0.19 - 3.67$ % (b) OES intensities of CN ($\Delta v = 0, -1$) band-heads as a function of $\chi_0(\text{N}_2)$.

6.1.3.2 C₂

There is a moderate increase in the intensity of the C₂ 516 nm peak with $\chi_0(\text{N}_2)$ until a sharper increase observed between $\chi_0(\text{N}_2) = 1.83$ and 3.67 %. The intensity increase at the highest $\chi_0(\text{N}_2)$ is attributed to the influence of additional N₂ but to the way the experiment was conducted. The issue arises because $\chi(\text{C}_2)$ is strongly influenced by the H:C ratio in the plasma.^[76] The plasma conditions used for all the spectra except for $\chi_0(\text{N}_2) = 3.67$ % utilized flow rates of $F(\text{H}_2) = 500$ and $F(\text{CH}_4) = 35$ sccm and the increase in $\chi_0(\text{N}_2)$ was achieved by increasing $F(\text{N}_2)$ from 1 to 10 sccm ($\chi_0(\text{N}_2) = 0.19 - 1.83$ %). As $\chi_0(\text{N}_2)$ is increased in this range, the ratio of H:C was marginally decreased, resulting in a gradual increase in $\chi(\text{C}_2)$. As the MFC used had a maximum $F(\text{N}_2)$ of 10 sccm, to obtain $\chi_0(\text{N}_2) = 3.67$ %, the $F(\text{H}_2)$ had to be reduced to 250 sccm, while the $F(\text{CH}_4)$ and $F(\text{N}_2)$ were maintained at 35 and 10 sccm, respectively. This reduction in the H:C ratio explains the jump in C₂ intensities for $\chi_0(\text{N}_2) = 3.67$ %.

As for CN ($\Delta v = 0$), the C₂ ($\Delta v = 0$) emission is the most intense. The intensities for $\Delta v = 1$ and -1 are of similar magnitude to each other, with $\Delta v = -1$ being slightly more intense. This is due to there being a greater probability in diatomic species of a $\Delta v = 0$ transition.^[75]

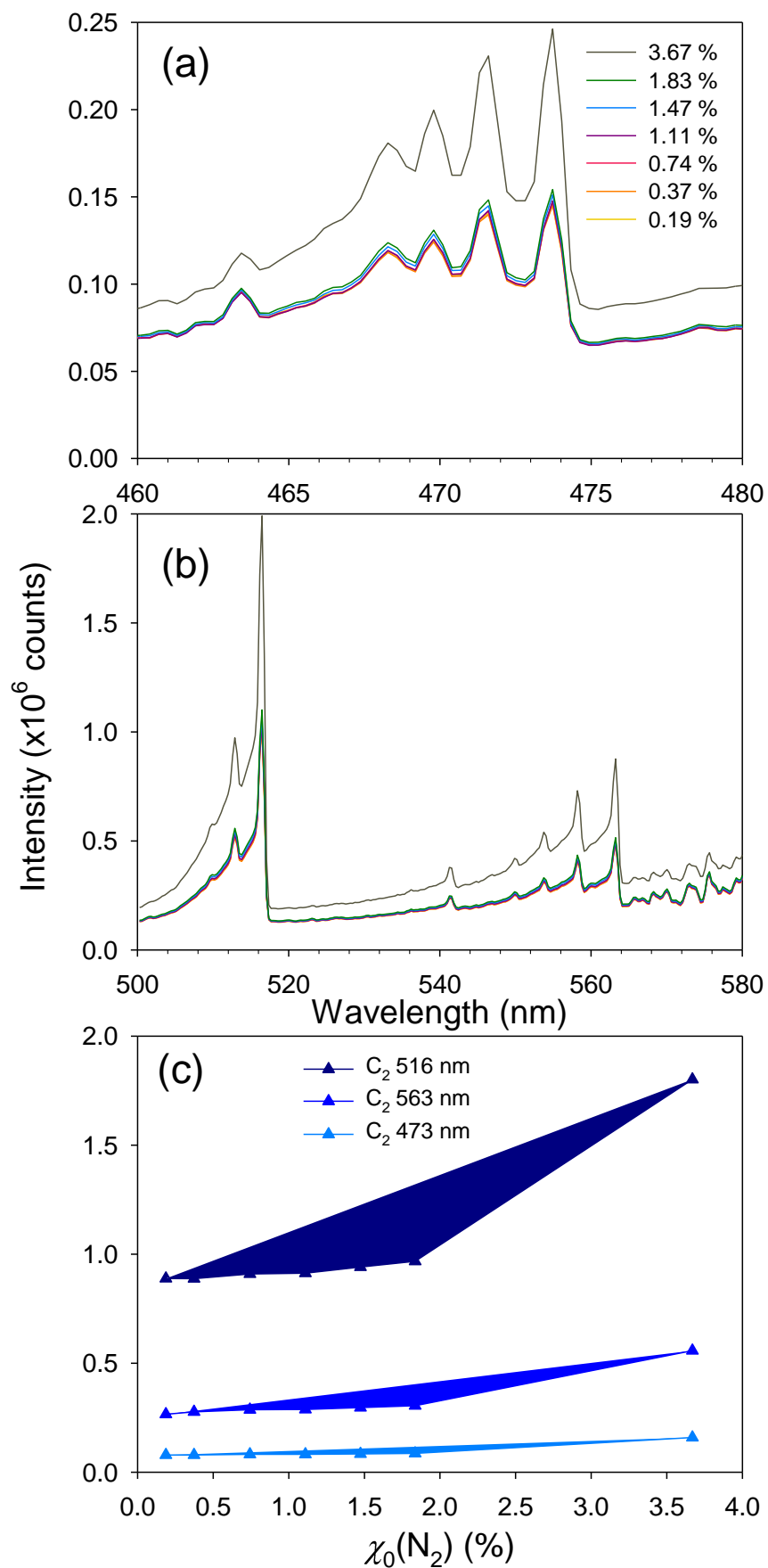


Figure 42: OES for (a) C_2 ($\Delta v = 1$) and (b) C_2 ($\Delta v = 0, -1$) for $\chi_0(N_2) = 0.19 - 3.67\%$ (c) OES intensities for C_2 ($\Delta v = 0, -1, 1$) band-heads as a function of $\chi_0(N_2)$.

6.1.3.3 CH

At low $\chi_0(\text{N}_2)$ there is little fluctuation in the CH emission intensity, then at $\chi_0(\text{N}_2) \sim 1.11\%$ a sharp linear increase is observed. The intensity of the CH ($\Delta v = 0$) band is lower than the CN and C_2 ($\Delta v = 0$) band-heads.

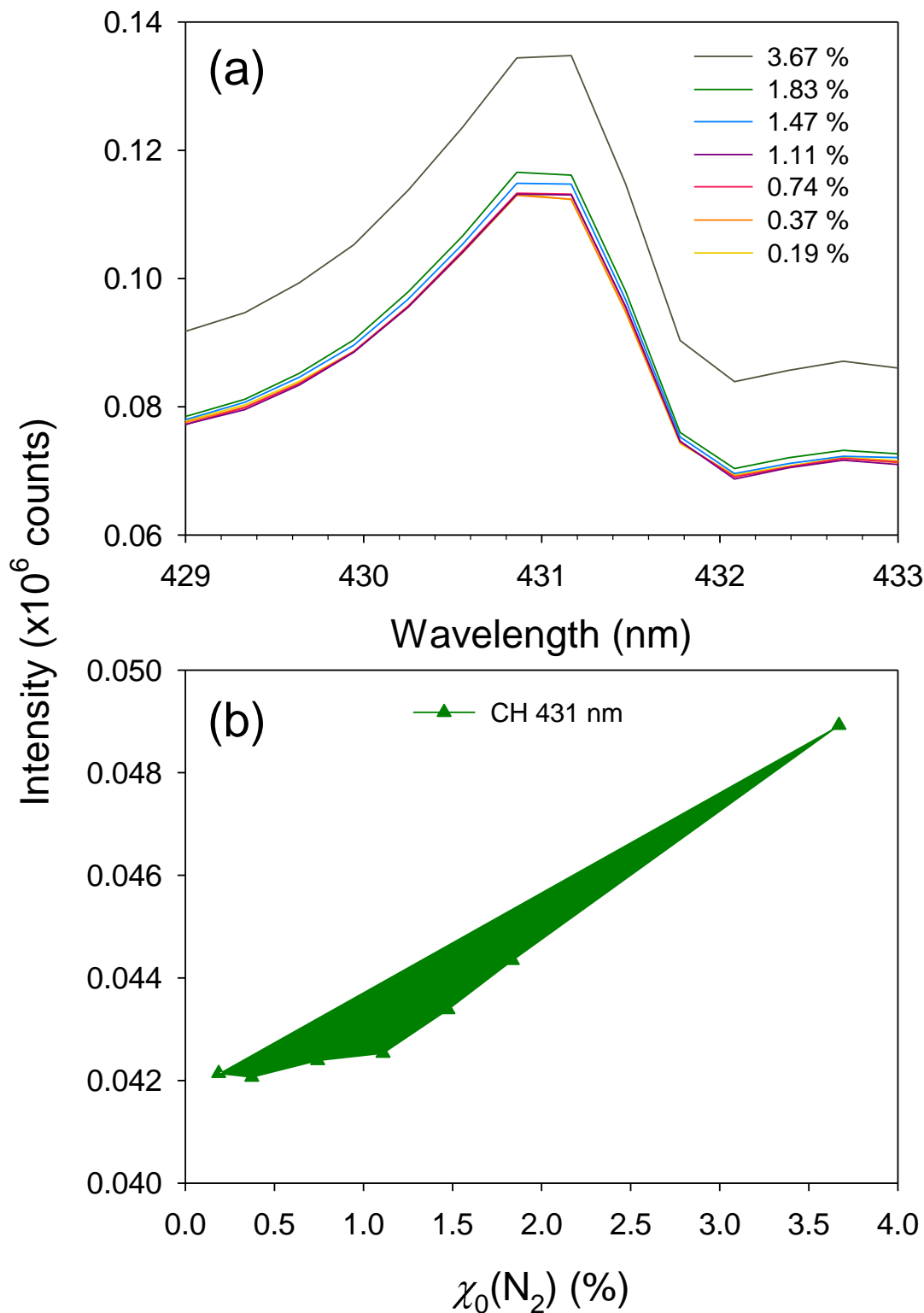


Figure 43: (a) OES for the CH radical for $\chi_0(\text{N}_2) = 0.19 - 3.67\%$ (b) OES intensity of CH ($\Delta v = 0$) band-head as a function of $\chi_0(\text{N}_2)$.

6.1.3.4 H

The intensities from the H atom spectral lines stay roughly constant with increasing $\chi_0(\text{N}_2)$ with a small decrease corresponding to $\chi_0(\text{N}_2) = 3.67\%$. As $\chi_0(\text{N}_2)$ is increased from 0.19% to 1.83%, $\chi_0(\text{H}_2)$ only changes from 93.3 to 91.7% and results in only minor fluctuations. The decrease in intensity for $\chi_0(\text{N}_2) = 3.67\%$ ($\chi_0(\text{H}_2) = 84.7\%$) is likely to be due to the altered H:C ratio influencing the intensities of the atomic H spectrum.

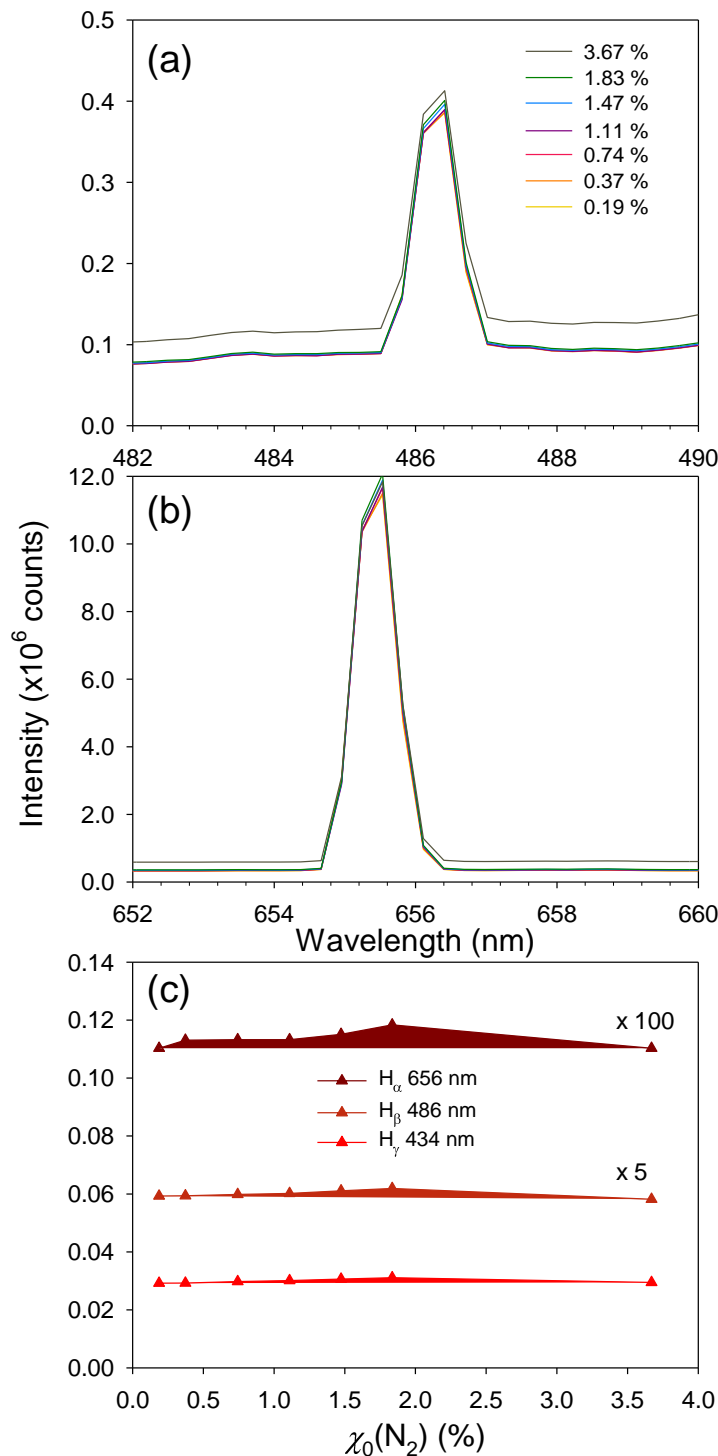


Figure 44: OES for (a) H_α and (b) H_β for $\chi_0(\text{N}_2) = 0.19 - 3.67\%$ (c) Intensities of $\text{H}_{\alpha, \beta, \gamma}$ peaks as a function of $\chi_0(\text{N}_2)$.

6.2 Preferential Nucleation

In order to use NCD lenses to focus the x-ray synchrotron radiation down to nanometre resolution, the diamond layer in the trench regions of the Si mould needs to be between 30 and 100 μm thick. This proved not possible using the deposition conditions described above due to the overlapping growth on the top surface of the mould. Moreover, the narrower trenches in the kinoform lens design meant a solution was required in which the diamond deposited on the top surface would not hinder the deposition in the trench regions. Preferential nucleation or selective seeding of the moulds before deposition could, theoretically, ensure that diamond is, initially, only deposited in the trenches, producing a thicker diamond layer in the recessed areas. If required, for a thicker, free-standing lens chip, a diamond layer could be grown on the top surface as a subsequent/re-seeded step. This would allow construction of a uniform lens chip, free from any voids and unwanted internal surfaces. Initial attempts to realise this comprised manually wiping the seed layer from the top, but the project progressed into various, more advanced methods as detailed in **Sections 6.2.2, 6.2.3 and 6.2.4**. The lens samples have been labelled with a letter, according to the methodology and its relative success, and with a Roman numeral, according to the specific sample within the group.

6.2.1 Manual Removal of Nucleation Layer

The nucleation layer from both US and ES seeding is weakly bound to the silicon surface. Removal of the nucleation layer from the top surface will lower the growth rate in this region while not influencing the deposition in the trench regions. The simplest way to remove this seed layer is by manually wiping the surface.

The first attempts at removing the seed layer on the top surface used a lens cleaning tissue soaked in methanol to wipe the top surface after the sample had been nucleated using the US probe. Different methods of wiping the surface were attempted, including cleaning from each side of the sample, only in one direction or using multiple wipes, before diamond was deposited in the MWCVD reactor using conditions detailed in **Table 4**. It was found that this method was not able to remove all the diamond particles from the top surface with the result that diamond was deposited non-uniformly across the surface. The samples had streaks of diamond growth interspersed amongst streaks of bare silicon (**Figure 45**)

Cross-sectional SEM images of the two samples are displayed in **Figure 46** which show that for both trials there was still a lot of diamond deposition on the top surface, with only occasional areas less well nucleated. These regions are where the layer is not continuous due to the lower nucleation density.

Table 4: Process conditions for lens samples where the nucleation layer was removed manually.

Sample	Lens type	Trench height (μm)	Seeding	$\chi_0(\text{H}_2)$ (%)	$\chi_0(\text{CH}_4)$ (%)	$\chi_0(\text{N}_2)$ (%)	P (kW) p (Torr) T_s ($^\circ\text{C}$)	t_{growth} (h)	Seed removal
a/i	kinoform	50	US	92.76	6.49	0.74	1 110 630	5	1×tissue, 1×wipe
a/ii	kinoform	30	US	92.94	6.51	0.56	1 110 690	5	2×tissue, 4×wipe

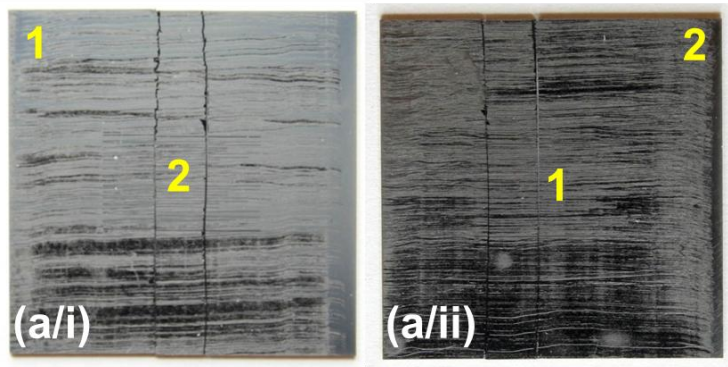


Figure 45: Photographs of the top surface **a/i** and **a/ii**. Deposition conditions are summarised in **Table 4**.

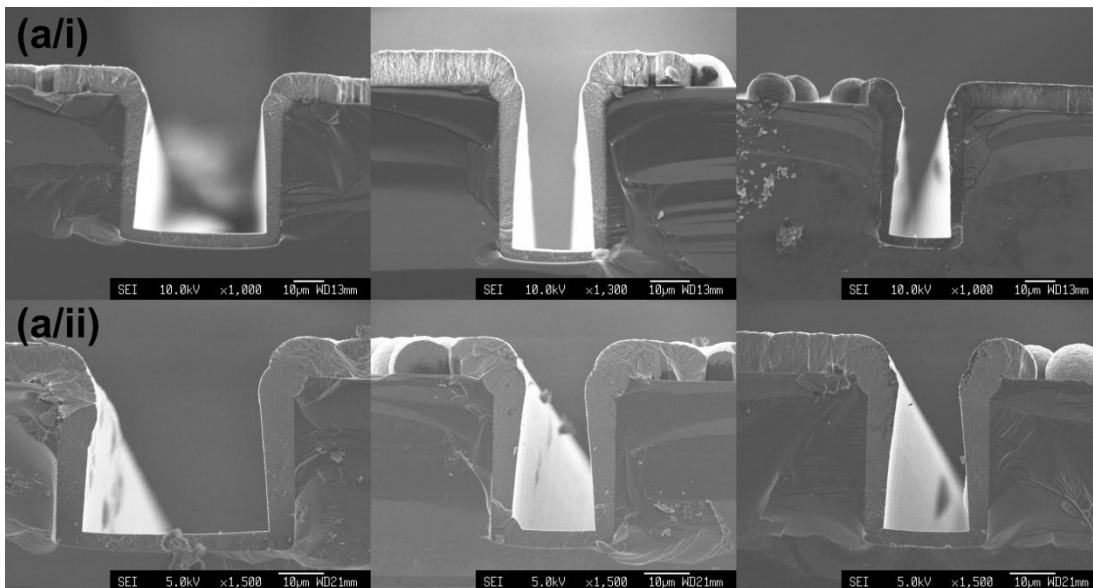


Figure 46: Cross-sectional SEM images of three different aspect-ratios for samples **a/i** and **a/ii**, which had been manually wiped before diamond deposition in the MWCVD reactor, as summarised in **Table 4**.

The Raman spectra for these samples (both $\lambda_{\text{exc}} = 325$ and $\lambda_{\text{exc}} = 514$ nm) are displayed in **Figure 47**. The values for $I(\text{sp}^3) / I(\text{sp}^2 \text{ 'D'})$ fit the trend for $\chi_0(\text{N}_2) = 0.74\%$ from **Figure 33** showing that the removal of the seed layer did not affect the quality of the deposited diamond, which is an important consideration when altering the pre-deposition conditions. Although the SEM images show unsatisfactory results, this was only a very simple preliminary technique which led to the development of more advanced lens-moulds, as detailed in the following sections.

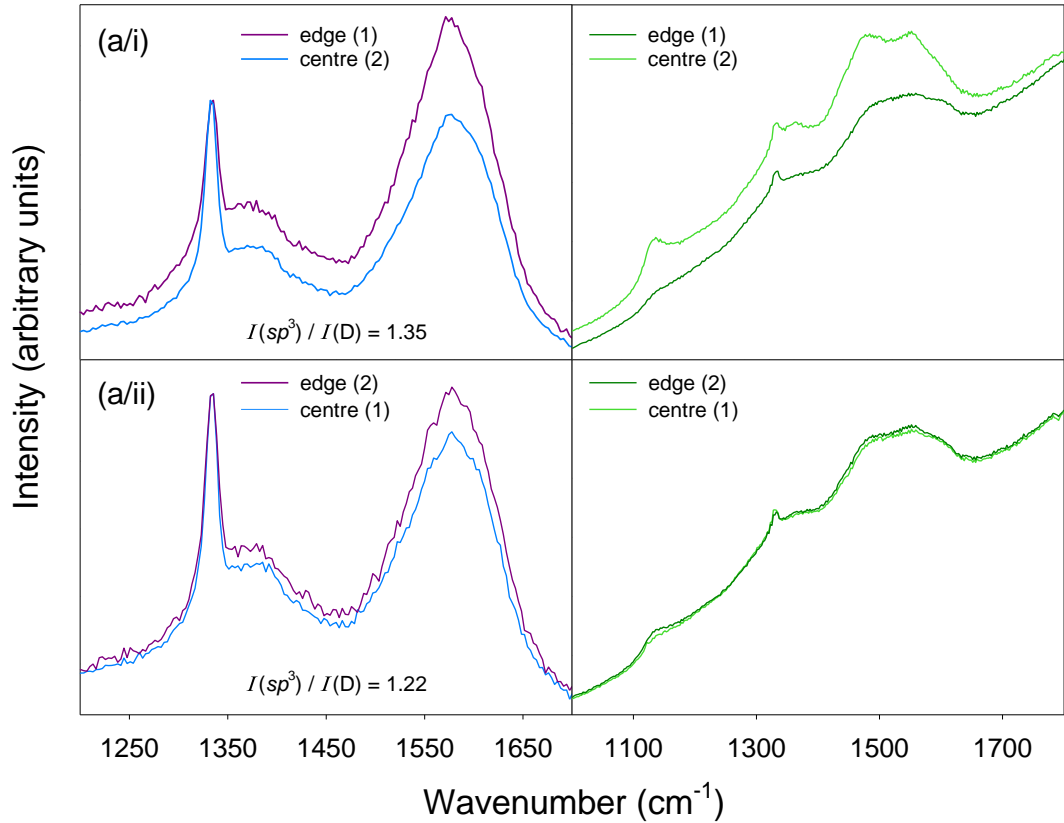


Figure 47: Raman spectra measured using $\lambda_{\text{exc}} = 325\text{nm}$ (left) and 514 nm (right) for group **a** samples. The numbers in parenthesis correspond to the photographs (**Figure 45**) showing the regions of the substrate where the spectra were taken.

6.2.2 Polymer-Resist-Coated Silicon Moulds

This method entailed using silicon moulds on which the top-surface is coated with a polymer resist. This resist has been used to mask the patterned lens design during etching of the silicon moulds. This Si-etch step leaves the resist on the top surface while the sidewalls and trench regions are bare silicon.

The lens moulds are fabricated onto a 6-inch silicon wafer that holds an array of nine lens chips. The dicing of the wafers into the 9 individual 20×20 mm square chips was carried out two different methods. Initially, dicing was achieved using a diamond-saw at

MNTC but later chips were produced by laser-machining the wafers at the University of Bristol.

For the selective seeding process, the resist-coated lens moulds were seeded by electrospray (ES) deposition and then the resist layer was removed by either an O₂ plasma treatment at MNTC or in the MWCVD reactor using a H₂/N₂ plasma. The aim was to remove the resist layer together with the nucleation layer on top of it in the plasma, and leave only a nucleation layer in the mould recesses. After removal of the seed layer from the top surface the samples were grown under the standard MWCVD conditions. The processes for each test substrate are summarised in **Table 5**. The samples are categorised in terms of both success of the experiment and the deposition conditions used and so are not discussed in chronological order.

Table 5: Experimental details for the resist-coated lenses. All depositions were undertaken using the standard MWCVD conditions. $H = 50 \mu\text{m}$. Samples have been grouped according to the process used and the relative success of the preferential seeding and so are not in chronological order.

Sample	Lens type	Dicing	ES	H ₂ /N ₂ or O ₂	$\chi_0(\mathbf{x})$ H ₂ /N ₂ (sccm)	t_{removal} (min)	t_{growth} (h)	T (°C)	Selective?
b/i	kinofom	laser	×1	H ₂ /N ₂	500/10	30	3	705	✓
b/ii	kinofom	laser	×2	H ₂ /N ₂	500/10	30	3	690	✓
b/iii	kinofom	laser	×1	H ₂ /N ₂	500/10	20	3	700	✓
c/i	CRL	laser	×1	H ₂ /N ₂	500/10	30	18	700	✓
c/ii	CRL	laser	×1	H ₂ /N ₂	500/10	20	18	700	✓
d/i	kinofom	laser	×1	H ₂ /N ₂	250/10	30	3	690	✗
d/ii	kinofom	laser	×1	H ₂ /N ₂	500/10	60	3	700	✗
e/i	kinofom	saw	×1	H ₂ /N ₂	500/4	5	3	740	✗
e/ii	kinofom	laser	×1	H ₂ /N ₂	500/4	30	3	730	✗
f/i	kinofom	saw	×1	O ₂	-	60	3	710	✗
f/ii	kinofom	laser	×1	O ₂	-	60	3	710	✗
f/iii	kinofom	laser	×2	O ₂	-	60	3	710	✗

Five variables were investigated when optimising this resist method:

- i. dicing of the silicon wafer using a diamond-saw or laser machining;
- ii. resist removal in O₂ or H₂/N₂ plasmas;
- iii. exposure time (t_{removal}) in the H₂/N₂ plasma;
- iv. concentration of $\chi_0(\text{N}_2)$ in the H₂/N₂ plasma;
- v. density of nucleation layer determined by the number of ES depositions.

It was found that if the silicon wafer had been diced into the nine 20×20 mm lens chips using a diamond-saw then material from the cut would coat the top surface of the moulds. This contaminating material was not removed in the plasma and resulted in the deposition of a layer of NCD on the top surface regardless of how the resist was removed. Laser machining of the wafer into individual chips provided a cleaner method for dicing up the samples with the result that the diamond film was dependent on the selective nucleation rather than the total nucleation of the contaminating cutting debris. The laser-machining process does cause some material to be deposited at the extremities of each 20×20 mm lens chip, but this did not cause unwanted diamond deposition in these regions. After this issue was encountered all lens samples were diced using the laser-machining method.

Using a H₂/N₂ plasma to remove the resist and the seeding layer from the top surface of the substrates was investigated first. A range of nitrogen concentrations were investigated, $\chi_0(\text{N}_2) = 0.79 - 3.85\%$. Initially, the gas mixture used similar ratios to the standard deposition conditions (without methane), although it was found that for $\chi_0(\text{N}_2) = 0.79\%$ (group **e** samples) the plasma was unable to remove the diamond seed layer together with the resist (**Figure 48**). The SEM images (**Figure 49**) of these samples show that a continuous diamond layer has grown across the whole structure and that after $t_{\text{growth}} = 3$ h the diamond layer on the top surface is thicker than that at the bottom. Extending the exposure time from $t_{\text{removal}} = 5$ (sample **e/i**) to 30 minutes (sample **e/ii**), while keeping the plasma conditions constant, did not improve the resist/seed layer removal and so was concluded that the plasma was not intense enough.

While the H₂/N₂ plasma conditions for group **e** were not extreme enough to remove the seed layer with the resist, other situations were found which were too effective and removed the resist and the seed layer not only from the top surface but the seeding in the trench regions as well (group **d**). Sample **d/i** used a plasma made up of $\chi_0(\text{N}_2) = 3.85\%$ in H₂ for $t_{\text{removal}} = 30$ minutes and removed the seed layer from the recessed areas as well as the top surface. The photographs of the top surface (**Figure 48**) look like the seeding has been selective because there was no diamond visibly deposited on the top surface. However the SEM cross-sections show that the diamond deposition across the entire structure is extremely sparse and non-continuous (**Figure 49**). Sample **d/ii** used a lower nitrogen concentration

($\chi_0(\text{N}_2) = 1.96\%$ in H_2) but for a longer exposure of an hour and, again, this was too effective at removing the nucleation layer from the trench areas as well as the top surface.

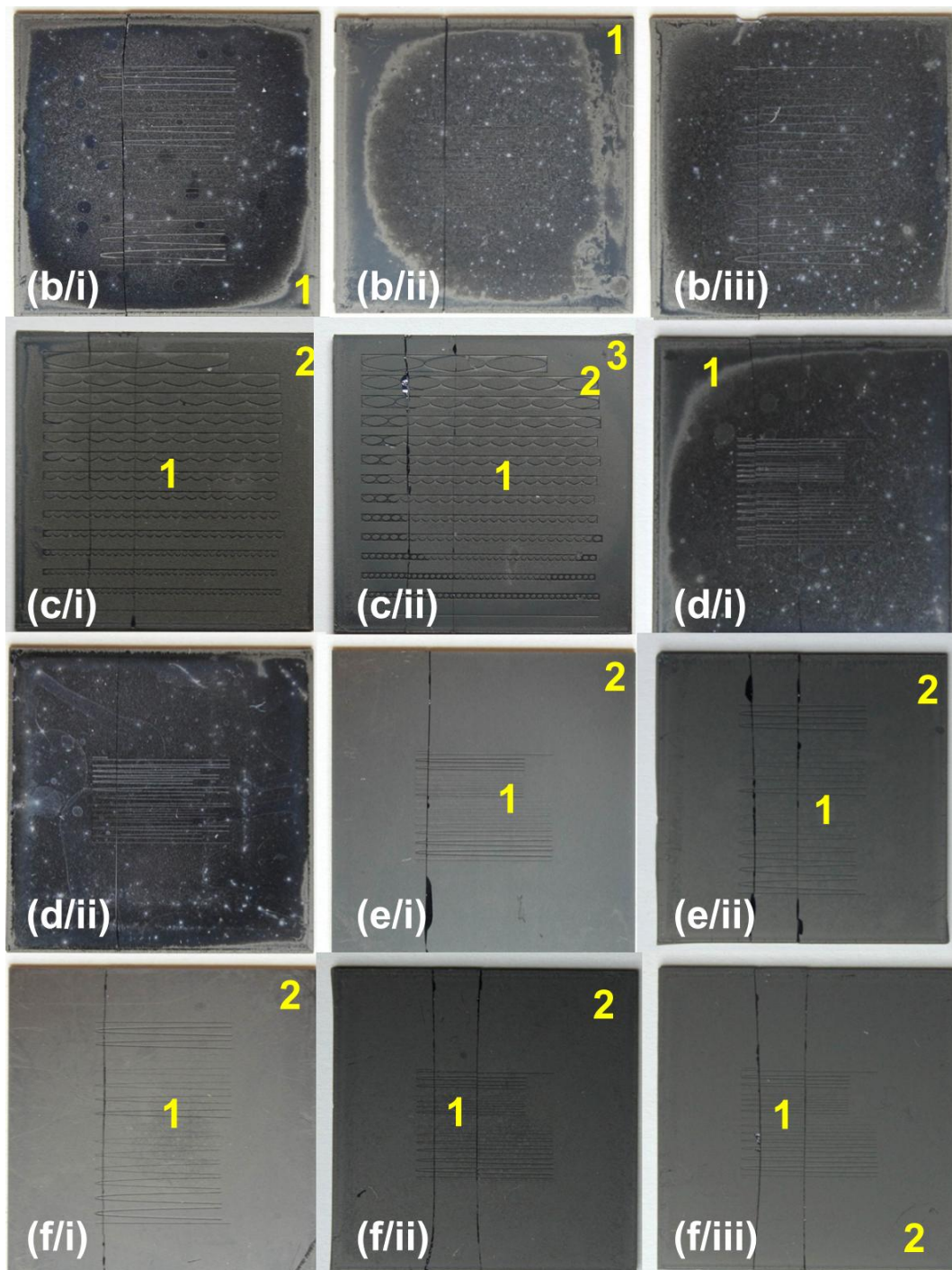


Figure 48: Top-view photographs of group **b**, **c**, **d**, **e** and **f** samples. Deposition conditions are summarised in **Table 5**. The numbers corresponds to regions on the substrate where Raman spectra were taken.

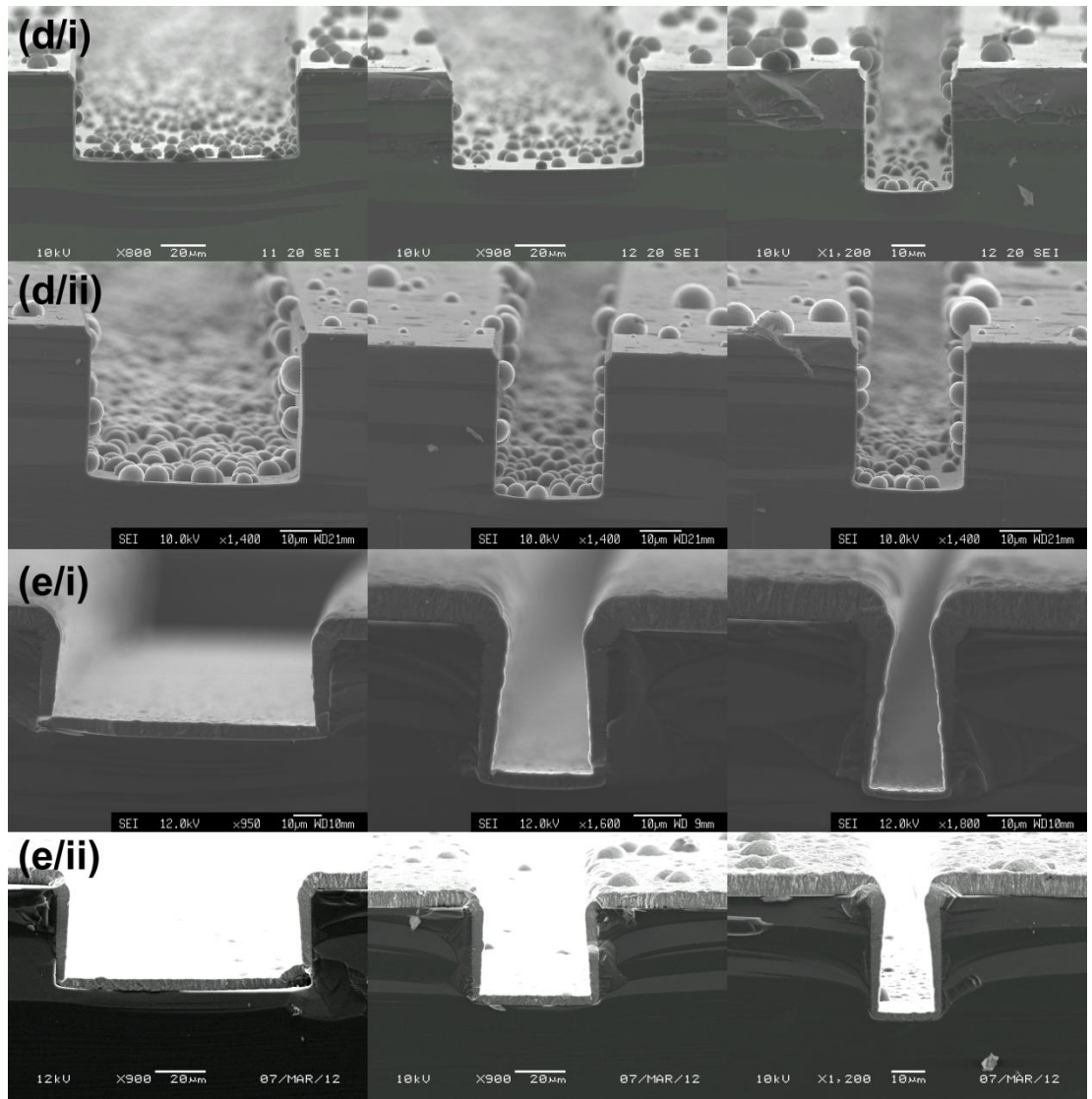


Figure 49: Cross-sectional SEM images of group **d** and **e** samples showing no selectivity in the seeding.

Achieving the removal of the seed from only the top surface while leaving the nucleating particles in the recessed areas of the mould required plasma conditions and exposure times located between the extremes already discussed. As such, a $\chi_0(\text{N}_2) = 1.96\%$ in H_2 plasma (from sample **d/ii**) was used but for a shorter exposure time of $t_{\text{removal}} = 30$ minutes. The photograph of the chip (sample **b/i**) shows minimal diamond deposited on the top surface and the SEM cross-sections show a continuous layer of diamond in the trench regions. This was the first successful selective seeding of these moulds where diamond had deposited preferentially in the mould recesses and only sparsely on the top surface. Although we hope to suppress the growth rate on the top surface of the mould, a non-zero nucleation density, and, hence, growth rate, is required to provide a diamond backing-layer that acts to hold the CRL arrays in a rigid structure.

Repeating these etch conditions after seeding the substrate twice in the ES apparatus (sample **b/ii**) showed little difference in the cross-sectional images. The double-seeding did

not greatly affect the diamond in the recessed areas although the nucleation density on the top surface was higher than the single-ES method (sample **b/i**). Therefore, an additional ES seeding step was not necessary to improve the results. After the positive result from sample **b/i**, this preferential seeding method was applied to a CRL design (sample **c/i**) with $t_{\text{growth}} = 18$ h to discover how the mould would fill over longer deposition times. Since the top surface after $t_{\text{growth}} = 3$ h was not completely bare (sample **b/i**) then over a longer deposition time a continuous layer would form on the top surface as well. A deposition time of 18 h was chosen as this was used to grow the previous batch of diamond CRLs which achieved a 400 nm focal width.

While the preliminary samples were grown on kinoform lens moulds as they have greater range of aspect ratios and therefore able to better scrutinize the preferential nucleation, the longer depositions were carried out using CRLs. There were two reasons for this: firstly, the NCD lenses that were previously tested at DLS^[61] were CRL designs and so allowed direct comparison with the selective-nucleation lenses. Secondly, the CRLs are lower aspect-ratio structures and will not overgrow the recessed areas as quickly during long depositions.

In the SEM cross-sections (**Figure 50**) for sample **c/i** it is seen that the longer deposition time using the CRL mould has produced a diamond thickness of ~ 20 μm in the recessed areas. However, the diamond layer in the trench-areas is not entirely uniform with a morphology of spherical diamond clusters implying that the nucleation layer was less dense than ideal. This shows that the initial H_2/N_2 plasma etch step removed slightly more of the seed layer than required. As expected for the longer deposition times, the cusping problem at the corners of the mould is still evident, particularly for the highest aspect-ratio trenches.

To try and reduce the amount of nucleating diamond material etched during the H_2/N_2 plasma step sample **b/iii** was fabricated using the same conditions as sample **b/i** with $t_{\text{growth}} = 3$ h, but a shorter etch time of $t_{\text{removal}} = 20$ minutes. It was clear from the SEM cross-sections that this was still long enough to remove the nucleation layer from the top surface, while not etching the seeding in the trench regions. This shorter etch step was then used for the deposition of a CRL mould for $t_{\text{growth}} = 18$ h (sample **c/ii**) in hope that the lower regions of the mould would be more uniform compared with sample **c/i**. The SEM cross-sections show an improvement with a continuous diamond layer on both the top and bottom surfaces, and better $\phi_{\%}$ for the lens moulds. The quality of the diamond film has also benefitted with less internal structure visible within the film and fewer voids and imperfections.

In both long depositions, the top layer of diamond was still thicker than that at the bottom of the recesses, resulting in cusping in the higher aspect-ratio trench regions. This resist method will need to be improved in future work where, it is hoped, diamond deposition

is hindered on the sidewalls of the mould as well as the top surface. Quantitative analysis of these long-deposition samples will be addressed in **Section 6.2.5**.

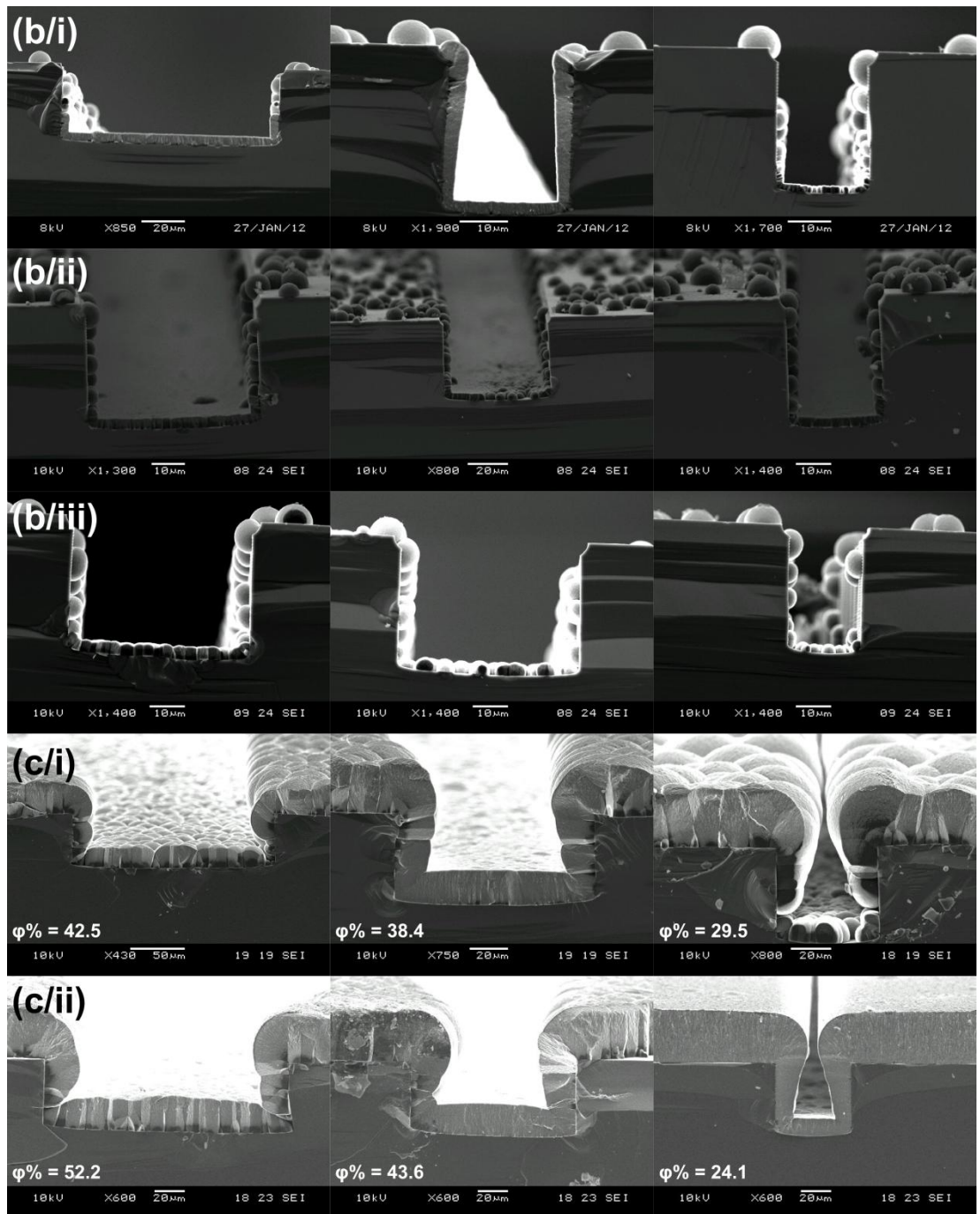


Figure 50: Cross-sectional SEM images of group **b** and **c** samples, whereby group **c** conditions repeat the conditions of **b** samples but for a longer deposition time of $t_{\text{growth}} = 18$ h. Deposition conditions are summarised in **Table 5**.

In theory the O_2 plasma etch (group **f** samples) should be equally successful at selectively seeding the substrates, as this method is a widely used resist-removal procedure.^[77, 78] However, it was found that, despite the O_2 plasma successfully removing the resist, it did not remove the nucleation layer as well. Consequently, there was no selectivity and a NCD layer was still grown on the top surface. The O_2 plasma processing

was carried out at MNTC and this method was not extensively researched with only one process condition investigated. It is possible that altering the etch conditions could provide satisfactory results and this will be addressed in future work. Three samples were supplied to MNTC varying the dicing method and the number of times the sample was seeded by the ES method, however no difference was seen between them after the O₂ plasma treatment and $t_{\text{growth}} = 3$ h. The photographs (**Figure 48**) of the top-views show that a diamond layer has grown on the top surface and the SEM cross-sections (**Figure 51**) confirm that a continuous diamond layer has grown throughout the structure with no preferentiality for the recessed regions. Based on the current findings this method was deemed less successful than the H₂/N₂ etch.

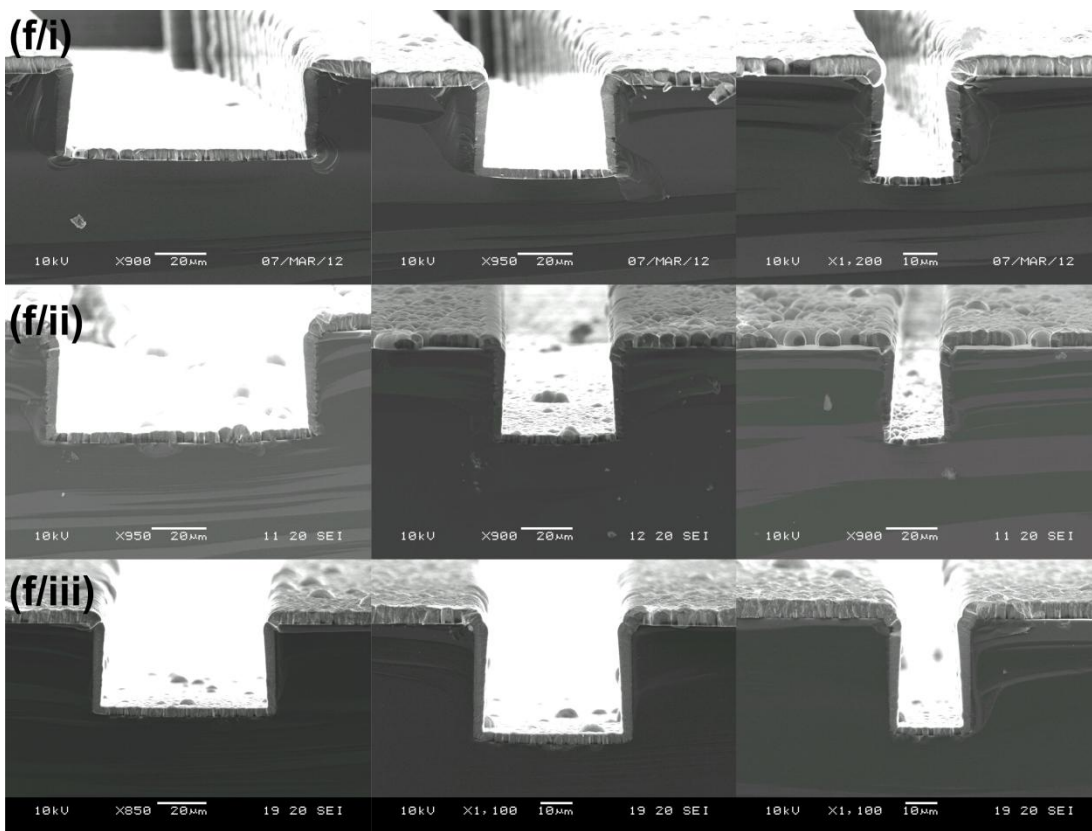
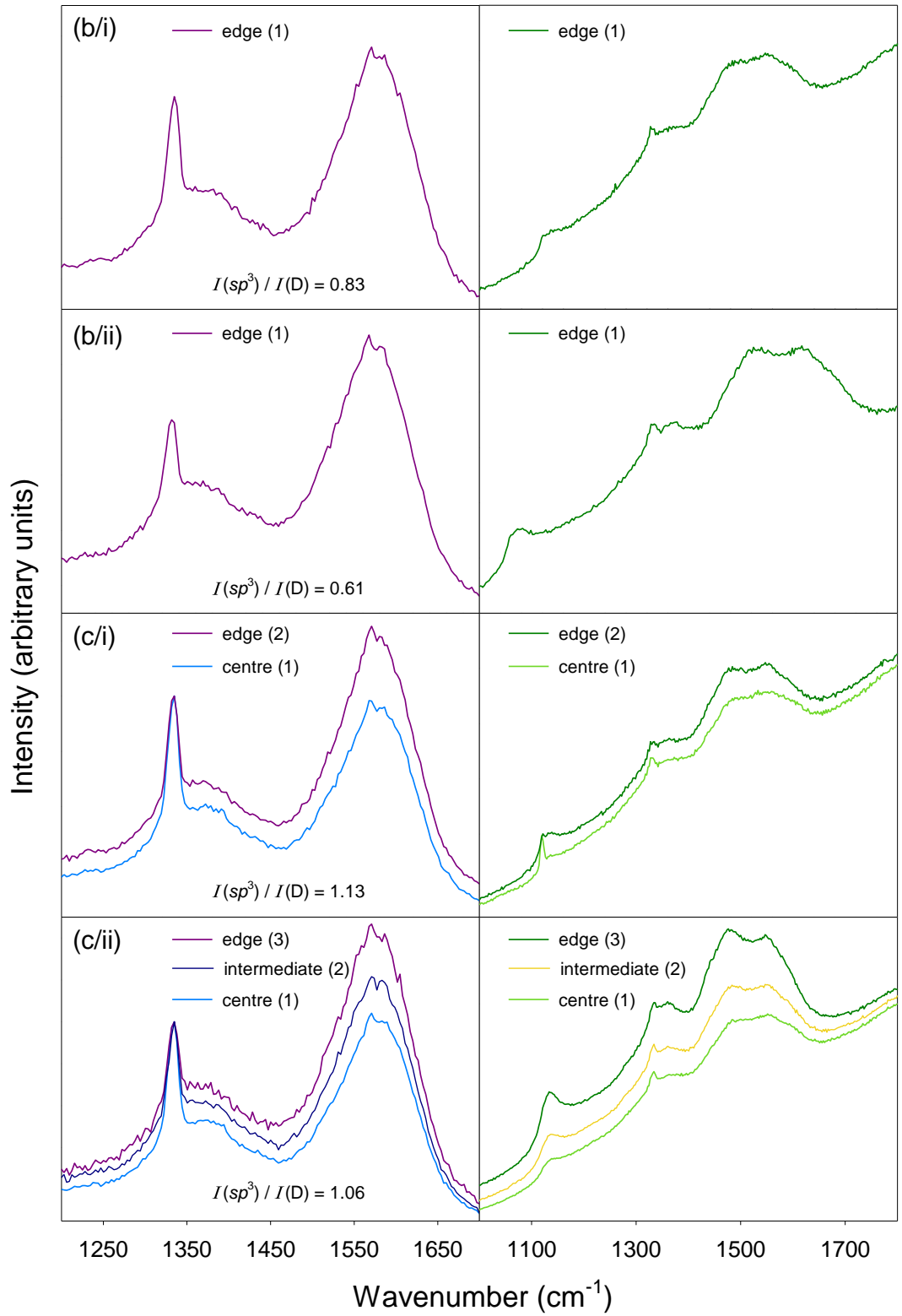
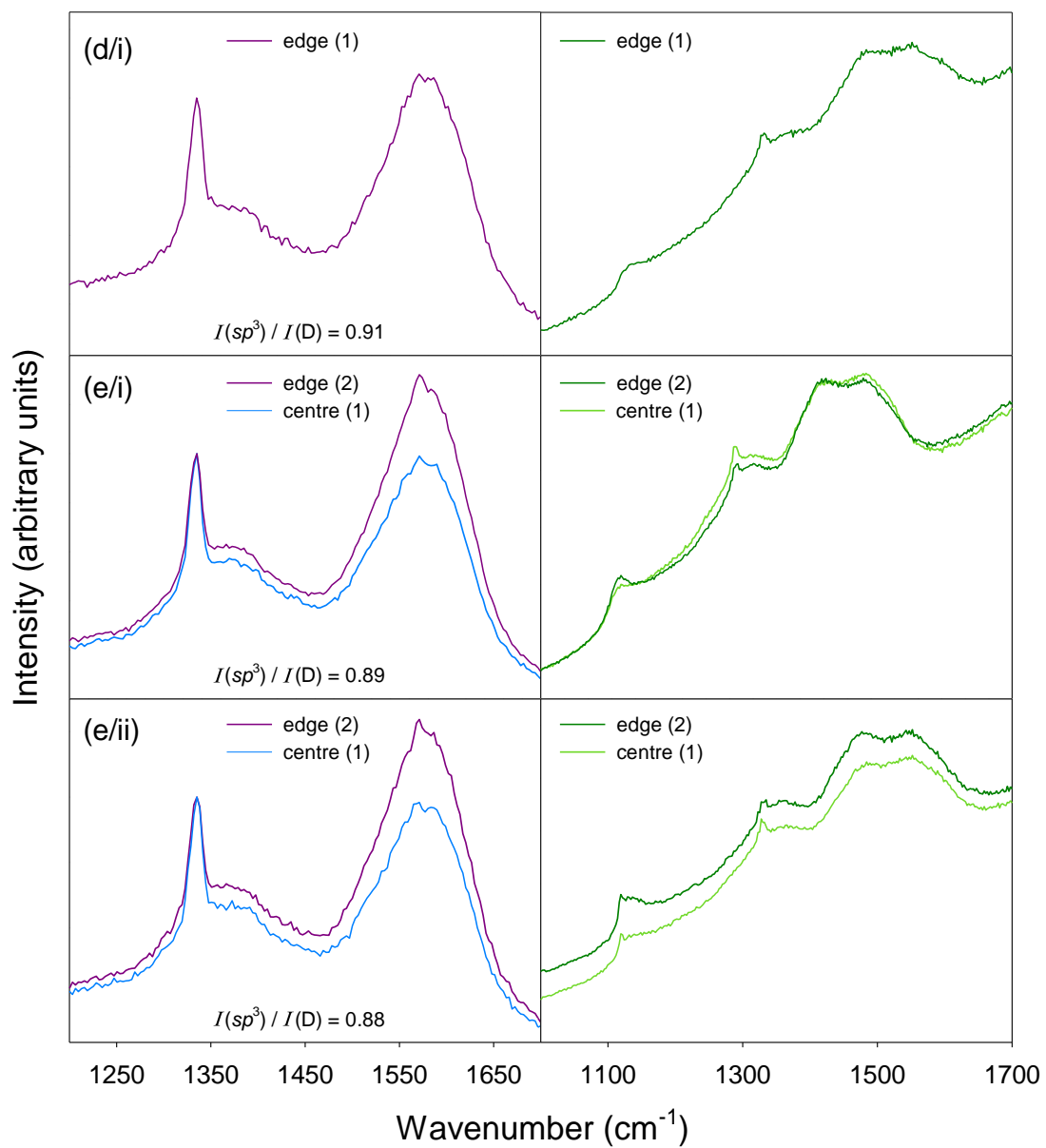


Figure 51: Cross-sectional SEMs of group f samples at a range of aspect ratios. Deposition conditions are summarised in **Table 5**.

The Raman spectra for the group **b**, **c**, **d**, **e** and **f** samples (**Figure 52**) have been taken where possible if there was a sufficient diamond on the top surface. They confirm that the desired NCD morphology has been deposited with all $I(sp^3) : I(D)$ ratios falling within a small range.

The next stages of this project will involve attempting to limit diamond deposition on the sidewalls, as well as the top surface, and also trying a range of different O₂ plasma conditions to see if this technique can perform as well as the H₂/N₂ MWCVD method.





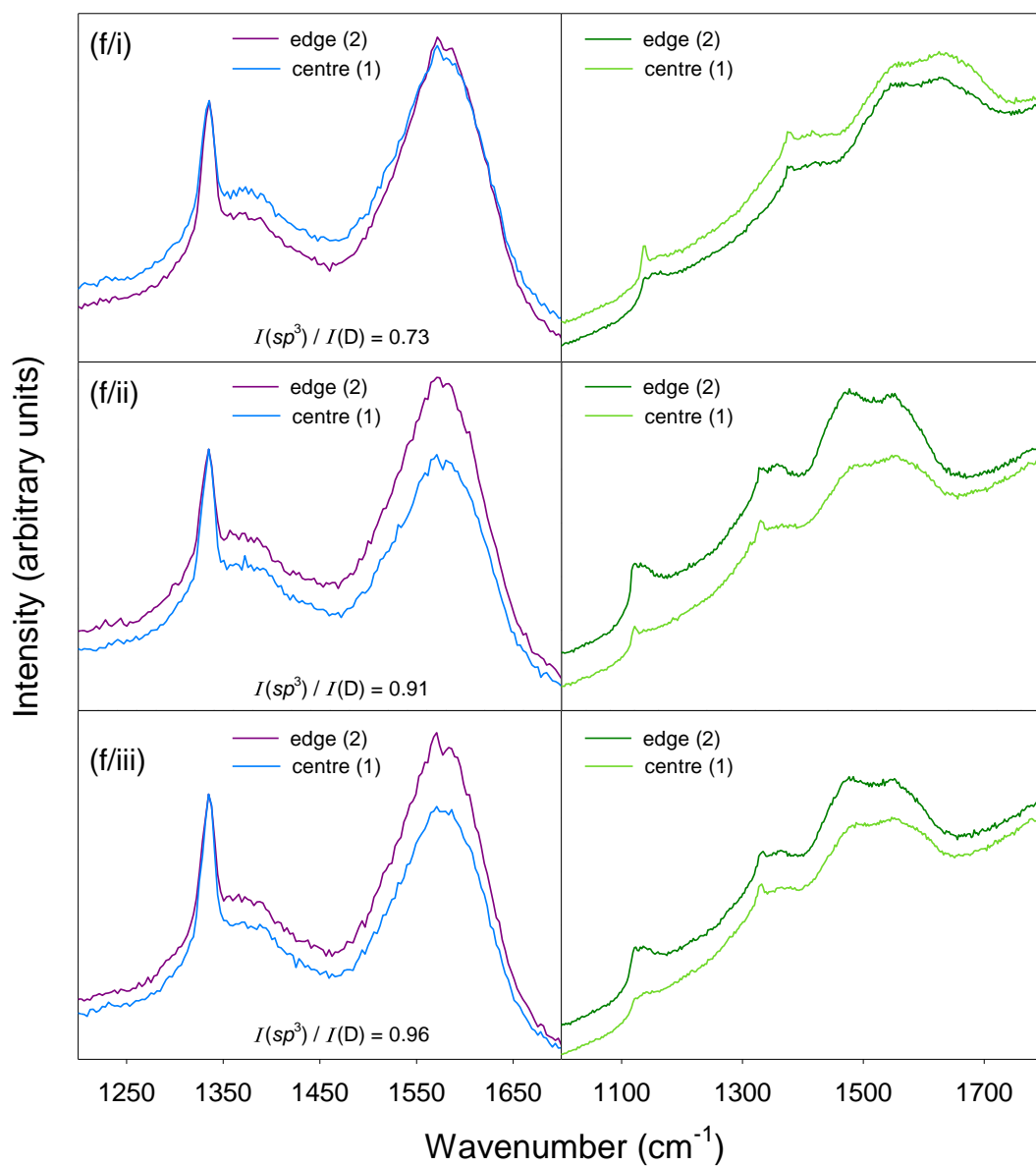


Figure 52: Raman spectra measured using $\lambda_{\text{exc}} = 325$ nm (left) and 514 nm (right) for group **b**, **c**, **d**, **e**, **f** samples. The numbers in parenthesis correspond to the photographs (**Figure 48**) showing the regions of the substrate where the spectra were taken. Deposition conditions are summarised in **Table 5**.

6.2.3 Oxide Coated Silicon Moulds

Section 5.3.2 described how the ES method can be used to seed the substrates by forming an electric field between the syringe nozzle, and the conducting/earthed substrate holder. As silicon oxide is electrically insulating and silicon is semiconducting it was hypothesised that if certain areas of the silicon moulds were coated in SiO₂, while leaving the trenches as bare Si, then the electro sprayed particles would follow the electric field lines to the conducting regions on the sample, thus selectively seeding the trenches.

Six oxide-coated silicon lens moulds were fabricated by MNTC, consisting of three different types (two of each) depending on the position of the oxide coating:

- i) oxide only on the top surface (T);
- ii) oxide over the entire sample, top/sidewall/bottom (T+S+B);
- iii) oxide on the top surface and the sidewalls (T+S).

The oxide layer on the top surface is $\sim \times 10$ thicker than the layer inside the trench due to the way in which it was fabricated. The additional fabrication steps required to remove oxide from the bottom of the trench (from T+S+B to T+S) is expensive and so two of the samples (**ii**, above) were retained to discover if the extra processing steps were necessary to induce the preferential nucleation. It was thought that the thin oxide layer at the trench bottom would not provide much resistance to the selectivity. Four of the lens substrates were tested using this electrostatic preferentiality theory (group **g**), while the remaining two were used to investigate a different technique (group **h**). The process conditions and substrate details are provided in **Table 6** (group **g**) and **Table 7** (group **h**).

Table 6: Experimental details for group **g** oxide-coated samples. All depositions were undertaken using the standard MWCVD conditions. The lens substrates were kinoform designs with a trench height of 50 μm and the wafers diced using a diamond saw.

Sample	Oxide position	Seeding method	Extra seeding details	t_{growth} (h)	T_s ($^{\circ}\text{C}$)	Selective?
g/i	T+S	ES x 1 standard	N/A	3	720	✗
g/ii	T	ES x 1 standard	manual wipe (MeOH)	3	720	✗
g/iii	T+S+R	ES x 1 insulating	N/A	3	700	✗
g/iv	T+S+R	ES x 1 insulating	oxide layer removed off backside of mould	3	685	✗

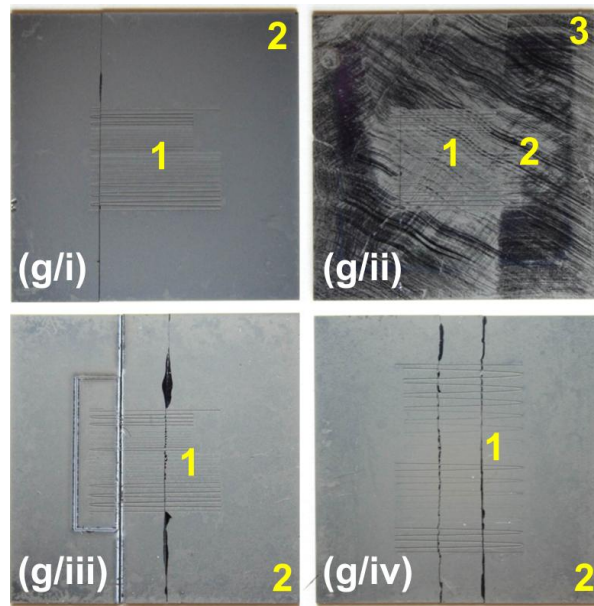


Figure 53: Photographs of the top surface of group **g** samples. Deposition conditions are summarised in **Table 6**. The numbers corresponds to regions on the substrate where Raman spectra were taken.

To test the selectivity of the ES system to samples with insulating oxide and conducting Si areas a substrate (sample **g/i**) was seeded using the standard ES holder and a diamond film grown using standard conditions in the MWCVD reactor. After $t_{\text{growth}} = 3$ h it was clear (**Figure 53**) that the seeding had not been selective and that diamond had uniformly deposited across the substrate. This was confirmed when looking at the SEM cross-sections (**Figure 55**) where after $t_{\text{growth}} = 3$ h the top surface had grown thicker than the layer in the trench area. The nucleation was uniform with no preferential nucleation for the bare Si areas over the oxide coated regions. The same method was then employed for sample **g/ii**, except the top surface was manually wiped with MeOH after seeding to lower the nucleation density. Although this method had been unsuccessful for the US seeded substrates, it was interesting to compare the how tightly the seed layer was attached to the surface in the US compared to the ES samples. However, the results showed little difference in the nucleation density between the US and ES seeded wiped substrates.

A possible reason for the lack of selectivity in samples **g/i** and **g/ii** could be because the ES holder is metallic and, as it covers a larger area than the substrate, would mask any differences in the electric field caused by the SiO/Si substrate. To investigate this, the standard metal holder was replaced with a plastic, insulating ES holder where only the substrate was grounded and used to seed sample **g/iii**. After $t_{\text{growth}} = 3$ h, there was, again, no selectivity with the result identical to sample **g/i** (see SEM cross-section for sample **g/iii** in **Figure 55**). Another possible factor was that oxide layer was present on the reverse side of these samples which may be preventing the bare Si areas from being properly earthed. Before seeding sample **g/iv**, a region of the oxide layer on the reverse side was milled off to allow a better conducting contact to the ground (**Figure 54**). However, after seeding using

the insulating ES holder, the results were similar to the previous runs (**Figure 53** and **Figure 55**).

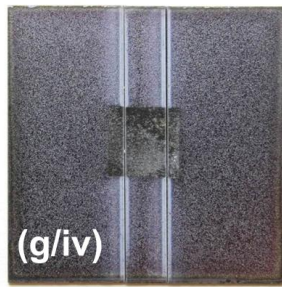


Figure 54: The reverse side of sample **g/iv** showing where the oxide layer has been milled off (dark central square) to provide better electrical contact to the earthed ES holder.

The reason for the lack of any selectivity in samples using the insulating ES holder (**g/iii** and **g/iv**) was unlikely to be due to the oxide layer at the trench bottom as this layer was very thin compared with the top layer. If the ES method had been preferential for SiO and Si coated regions then at least partial selectivity should have been observed in these samples with thin oxide in the recessed areas. Due to the lack in selectivity, the method was not investigated further as other methods proved more successful.

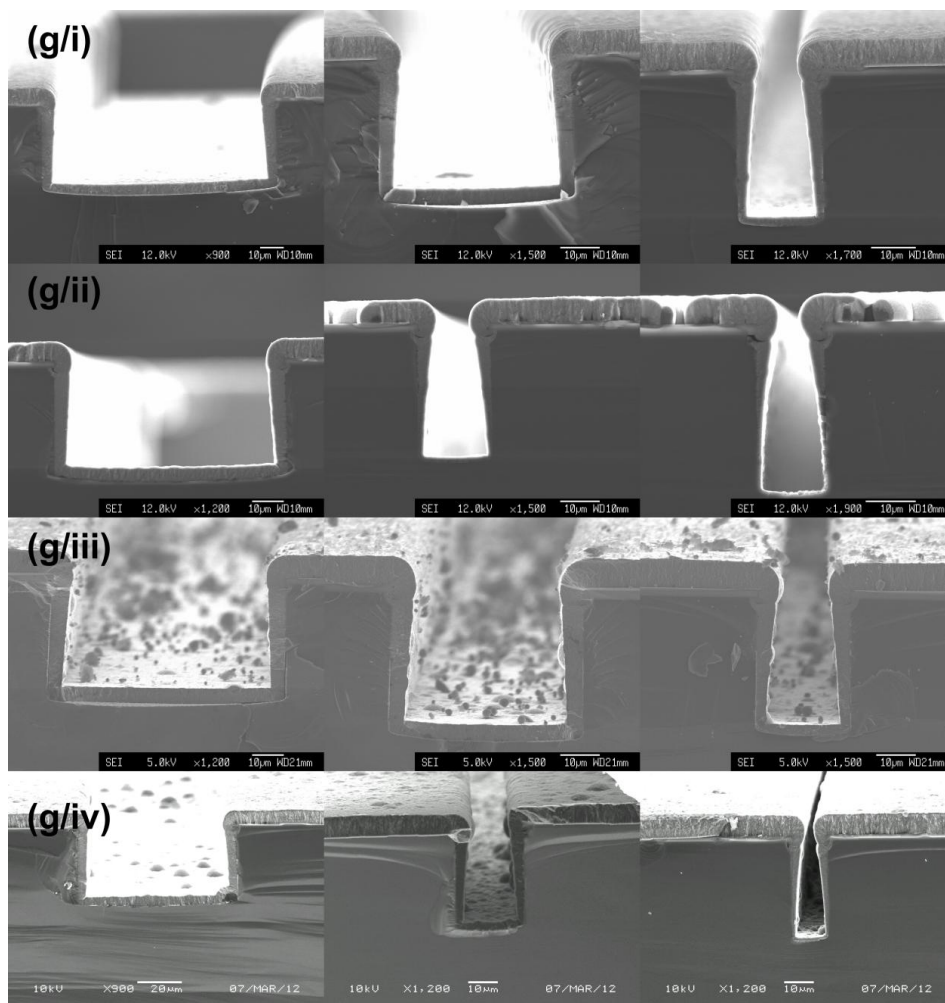


Figure 55: Cross-sectional SEM images for group **g** samples showing a range of aspect-ratios. Deposition conditions summarised in **Table 6**.

Raman spectra of the group **g** samples were taken which, again, indicate that the diamond deposited was of identical quality to that deposited using the standard conditions. The appearance of the $\lambda_{\text{exc}} = 514$ nm spectra for sample **g/ii**, results from the laser sampling regions with no diamond due to the manual wipe of the surface.

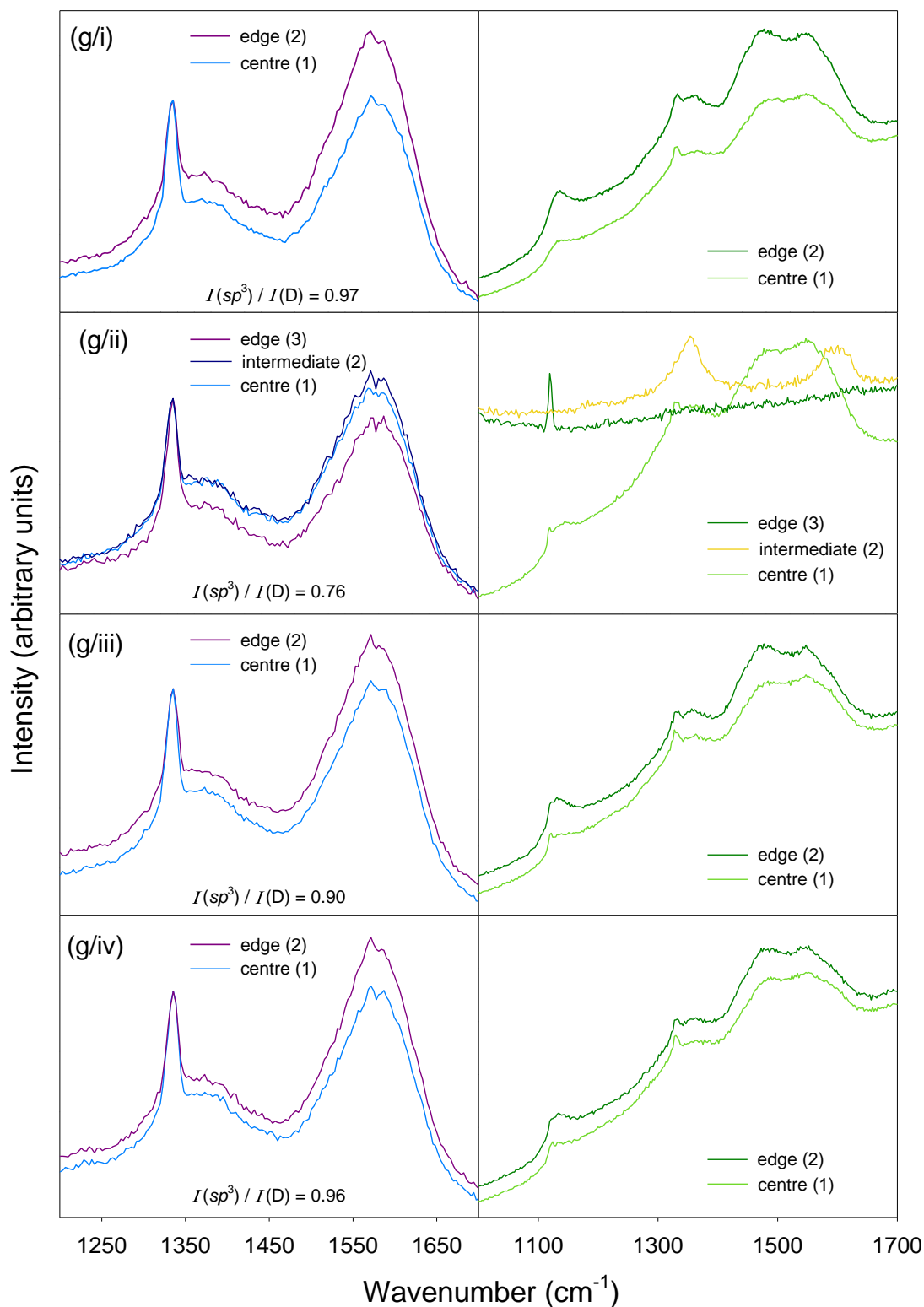


Figure 56: Raman spectra measured using $\lambda_{\text{exc}} = 325$ nm (left) and 514 nm (right) for group **g** samples. The numbers in parenthesis correspond to the photographs (**Figure 53**) showing the regions of the substrate where the spectra were taken.

As the preferential ES seeding had not worked as predicted, this approach was abandoned and another method investigated using the remaining oxide-coated lens samples (group **h**, **Table 7**). Here the samples were seeded using the standard ES method and a thin layer of NCD grown over the entire surface using a short CVD run. A buffered-oxide etch ($\text{NH}_3\text{F} + \text{HF}$) was then used to remove the oxide layer as well as the thin diamond layer that had grown on top of the oxide. It was necessary to deposit a thin layer of NCD before the HF etch, opposed to just nucleating the samples, as the wet acid etch would wash off the nucleating layer. After the HF etch the samples were returned to the CVD reactor for a further, thick diamond deposition.

Table 7: Experimental details for group **h** oxide coated samples. All depositions were undertaken using the standard MWCVD conditions. The lens substrates were kinoform designs with a trench height of 50 μm and the wafers diced using a diamond saw.

Sample	Oxide position	Seeding method	Extra seeding details	t_{growth} (h)	T_s ($^{\circ}\text{C}$)	Selective?
h/i / h/ii	T	ES \times 1 standard	i) standard MWCVD conditions $t_{\text{pre-etch}} = 15$ min ii) HF etch, $t = 60$ min	3 / 10	710	✓
h/iii	T+S	ES \times 1 standard	i) standard MWCVD conditions $t_{\text{pre-etch}} = 10$ min ii) HF etch, $t = 60$ min	3	690	✓

This method proved to be more successful than for group **g** samples with recessed areas preferentially growing instead of the surrounding top surface. An important variable identified in this work is the initial deposition time, $t_{\text{pre-etch}}$, before the acid etch. Photographs of the two substrates (consisting of three post-etch depositions because a section of sample **h/i** was placed back in the reactor for a further 7 h) are shown in **Figure 57**, and it can be seen that the top surface of sample **h/iii** (shorter $t_{\text{pre-etch}}$) has been more selective, with less diamond grown on the top surface. However, it is clear that there has still been deposition of diamond on the top surface in both cases and is an issue which will be addressed in further work using shorter $t_{\text{pre-etch}}$ times.

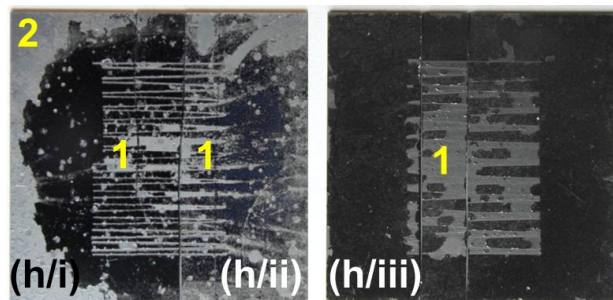


Figure 57: Top-view photographs of samples **h/i**, **h/ii** and **h/iii**. Deposition conditions are summarised in **Table 7**. The numbers corresponds to regions on the substrate where Raman spectra were taken.

The SEM cross-sections allow a better understanding of the deposition at different positions on the Si mould (**Figure 58**). The cross-section of sample **h/i** shows that, after $t_{\text{growth}} = 3$ h, the method has allowed selectivity of the recessed areas. However, from the top view it is clear that the acid etch is anisotropic, and unsuccessful in entirely removing the diamond from the top surface. Sample **h/ii** is the part of the same substrate that was grown for further 7 h resulting in $t_{\text{growth}} = 10$ h and, thus, allowing comparison with the N_2 variable work in **Section 6.1** which used this length of deposition time. The thickness in the trench is larger than when using non-preferential nucleation, although it is obvious that overgrowth on the corners is still a major problem. There is also the problem of a void forming between the silicon surface and diamond deposition on the top surface showing where the oxide layer has been removed (sample **h/ii**). For sample **h/iii** the cross-sections show that the HF etch was less uniform. There are regions where the top surface has little diamond deposition and other, adjacent areas, with a continuous diamond layer.

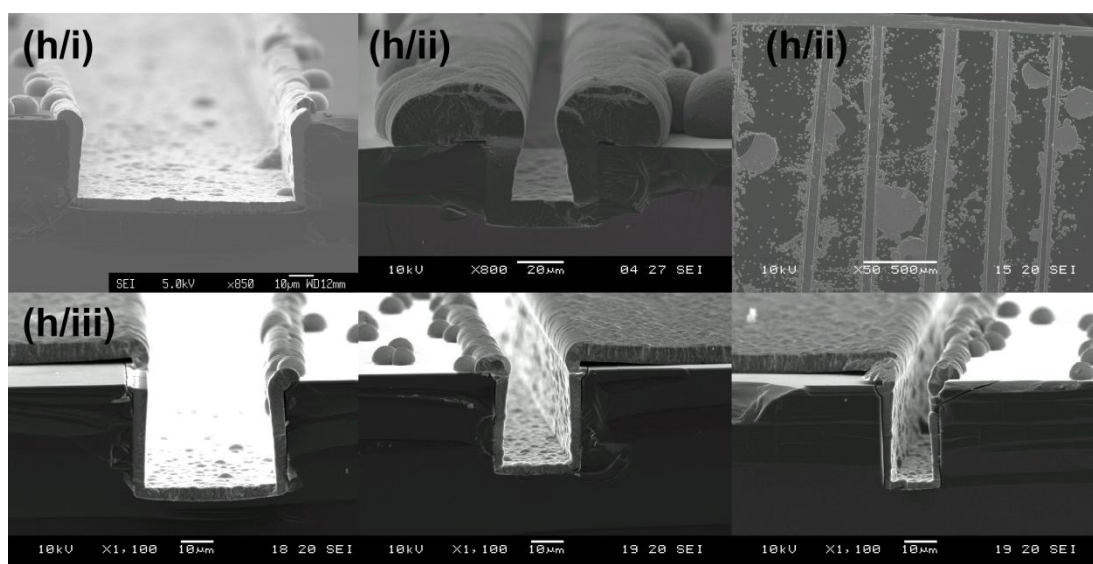


Figure 58: SEM images of group **h** samples. For sample **h/i**, a top view (top right) has been displayed as well. The other images are in cross-section. Deposition conditions are summarised in **Table 7**.

Although the partial-oxide/HF acid etch method shows promising results, the technique needs further optimisation of the pre-etch diamond thickness and uniformity of the acid etch. Future research will experiment with shorter $t_{\text{pre-etch}}$ so that the initial diamond layer is thinner. It is crucial that the thin diamond layer on the top surface (and sidewalls) is removed with the etch and so improved results are planned using a shorter deposition time where the growth is stopped before the film becomes continuous. The buffered-oxide etch step will also be optimised with hope of a uniform removal of diamond from the entire top surface (and sidewalls where applicable).

The Raman spectra for the samples are shown in **Figure 59**. As with the other selective seeding methods, it can be seen that the $sp^2:sp^3$ -carbon bonding ratio has been unaffected by the partial oxide/HF acid etch method, and the diamond quality across the

samples is similar to that the samples grown under standard, non-preferentially seeded, conditions.

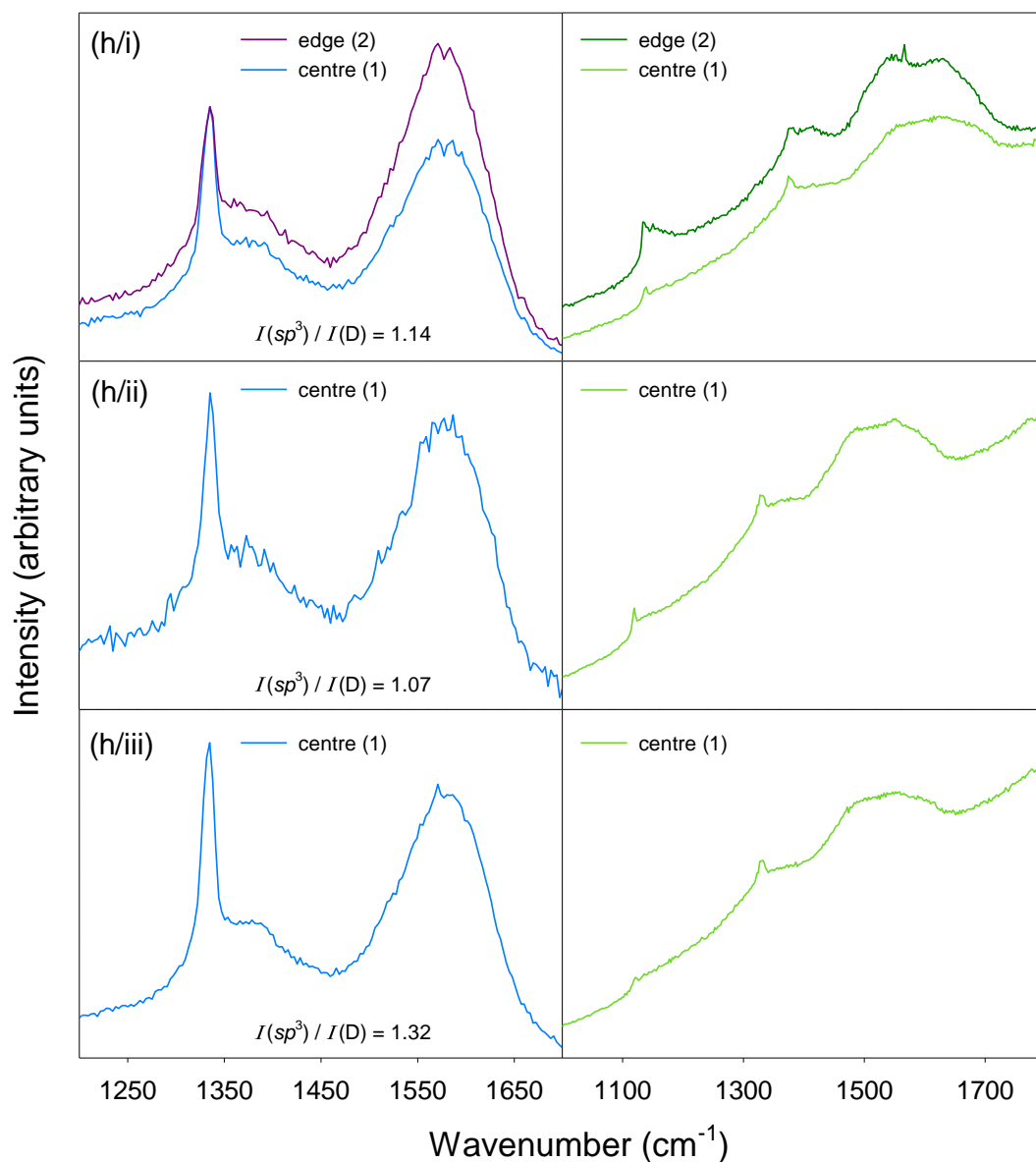


Figure 59: Raman spectra measured using $\lambda_{\text{exc}} = 325$ nm (left) and 514 nm (right) for group **h** samples. The numbers in parenthesis correspond to the photographs (**Figure 57**) showing the regions of the substrate where the spectra were taken.

6.2.4 Electrostatic Self-Assembly Nucleation

In 2010, Lee *et al.*^[79] devised a novel method for enabling CVD diamond to be deposited in a pre-determined pattern on a two-dimensional substrate using an electrostatic self-assembly method of two surfactants and diamond nanoparticles. This approach has been extended for the selective nucleation of our three-dimensional lens-mould structures. For this process, the resist-coated samples were submerged in a solution of a cationic polymer, polyethyleneimine (PEI), attaching it to the areas of bare Si in the lens mould. An anionic dispersion was made

by mixing ~5 nm diamond nanoparticles (ND) with an anionic polymer, poly sodium 4-styrene sulfonate (PSS). Submersion of the cationic-polymer-coated lens moulds in the anionic dispersion causes the spontaneous electrostatic self-assembly of the two polymers and selectively nucleates the sample. Removal of the resist in acetone results in the nucleation of only the trench and sidewalls.

Aqueous solutions of 10 wt % cationic polyethyleneimine (PEI, M_w : 8000, M_n : 600, Sigma Aldrich) and 10 wt % anionic dispersion agent, poly sodium 4-styrene sulfonate (PSS, M_w : 70,000, Sigma Aldrich) were prepared. To trial different concentrations of ND, dispersions 0.5 g or 1.0 g of ND solution (aqueous colloid, 98.8 wt %, Nano-Carbon Research Institute) were added to different portions of the PSS solution. On addition of the ND, the dispersion was treated for 5 min using an US probe to form a monodisperse suspension. For the nucleation process, a resist-coated lens substrate was placed in the PEI solution for 10 minutes, then rinsed in DI water and dried using an air-blower. The sample was then placed in the anionic dispersion for 16 – 18 h, after which it was rinsed and dried as before. The sample was then placed in acetone and agitated in an US bath for 10 s to remove the resist layer. As with the previous selective nucleation trials, initial testing of the experimental variables was carried out using kinoform samples (group **i**) with a range of aspect-ratio structures before longer depositions were attempted using CRL moulds (group **j**).

Table 8: Experimental details for group **i** and **j** samples. All lenses were grown in the MWCVD reactor using standard conditions. The trench height is 50 μm and wafers diced using the laser micromachine.

Sample	Lens type	Mass of ND (g)	$t_{\text{PSS-ND}}$ (h)	t_{growth} (h)	T_s (°C)	Selective?
i/i	kinoform	0.5	17.5	3	690	✓
i/ii	kinoform	0.5	17.8	7	690	✓
i/iii	kinoform	1.0	17.8	2.5	700	✓
j/i	CRL	0.5	17.5	18	690	✓
j/ii	CRL	0.5	17.8	36	690	✓

In the first trial (sample **i/i**) it was found that the self-assembly method was effective in selectively nucleating our three-dimensional structures. The photographs of the top surface of sample **i/i** (**Figure 60**) indicate minimal diamond deposition (hence a Raman

spectrum could not be taken) and the SEM cross-sections (**Figure 61**) show that a continuous diamond layer has formed in the trench area, yet hardly any diamond has formed on the top surface. The nucleation density on the top surface is lower than the other selective seeding methods showing that the resist removal step is an effective method for preferentially nucleating the substrate. The same method was repeated (sample **i/ii**) for longer deposition of $t_{\text{growth}} = 7$ h to determine how the selective deposition filled the moulds. Both the top surface and cross-section images indicate that more diamond has deposited on the top surface although it has not yet formed a continuous coating. Sample **i/iii** was prepared using a higher concentration of nanodiamond in the anionic dispersion. After $t_{\text{growth}} = 3$ h, this did not produce a different result from sample **i/i** so there was no benefit in using the higher concentration dispersion.

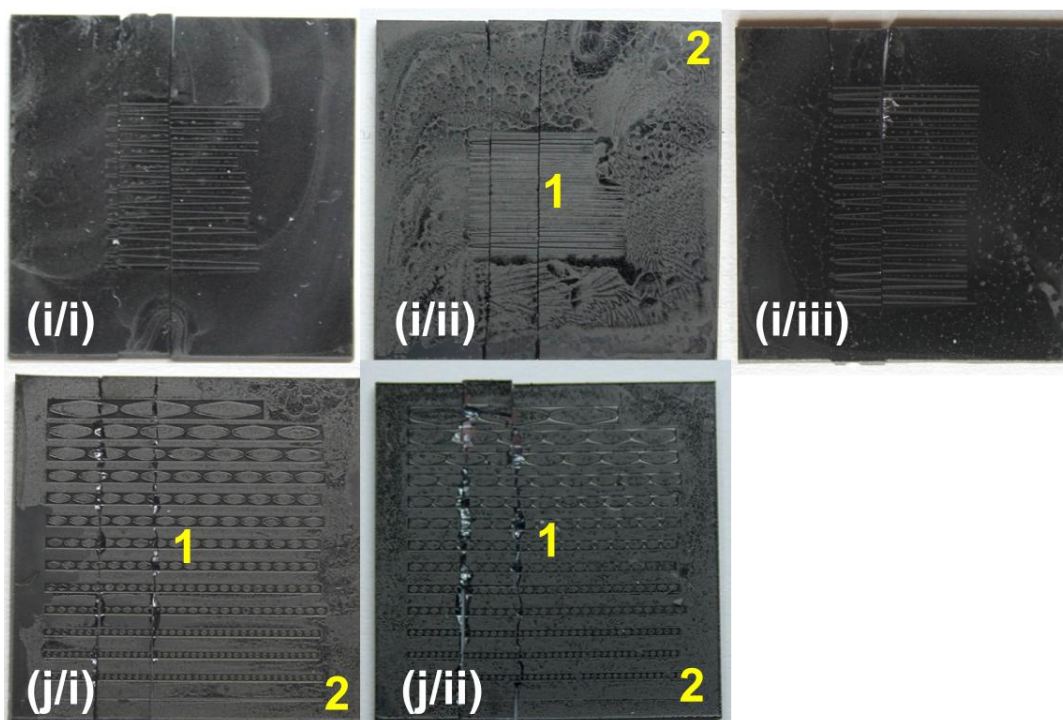


Figure 60: Top-view photographs of group **i** and **j** samples. Deposition conditions are summarised in **Table 8**. The numbers correspond to the regions on the substrate where Raman spectra were taken although the lack of diamond on the top surface meant that spectra were not always possible.

Due to the promising outcome of the preliminary $t_{\text{growth}} = 3$ h depositions, a $t_{\text{growth}} = 18$ h deposition using a CRL mould (sample **j/i**) was undertaken using the conditions tested for samples **i/i** and **i/ii**. The analysis of sample **j/i** showed the diamond layer in the trench reached $\sim 20 \mu\text{m}$ and, after $t_{\text{growth}} = 18$ h, the diamond layer on the top surface was still not continuous as seen by the lower magnification SEM image (**Figure 61**). As such, if the silicon were to be etched away to form the free-standing NCD lens, a longer deposition would be required, and, at the same time, enable an even better filling of the moulds. In the high aspect-ratio trenches there is still the problem with the cusping at the top corners of the recessed regions. For the short depositions, the growth of diamond at this position manifests

itself as a continuous line of diamond along the top edge of the mould. The positive result from this deposition is that the NCD layer is fully filling the bottom of the trench with a uniform coating, an improvement on the resist-coated method (**Section 6.2.2**) where occasionally the diamond nucleation has been less than ideal at trench corners.

A longer deposition was investigated for sample **j/ii** with $t_{\text{growth}} = 36$ h. The cross-sections (**Figure 61**) show that the top surface has now formed a continuous film and a thick diamond layer has been obtained in the mould with higher filling percentages than previous depositions ($\phi\% \sim 94\%$).

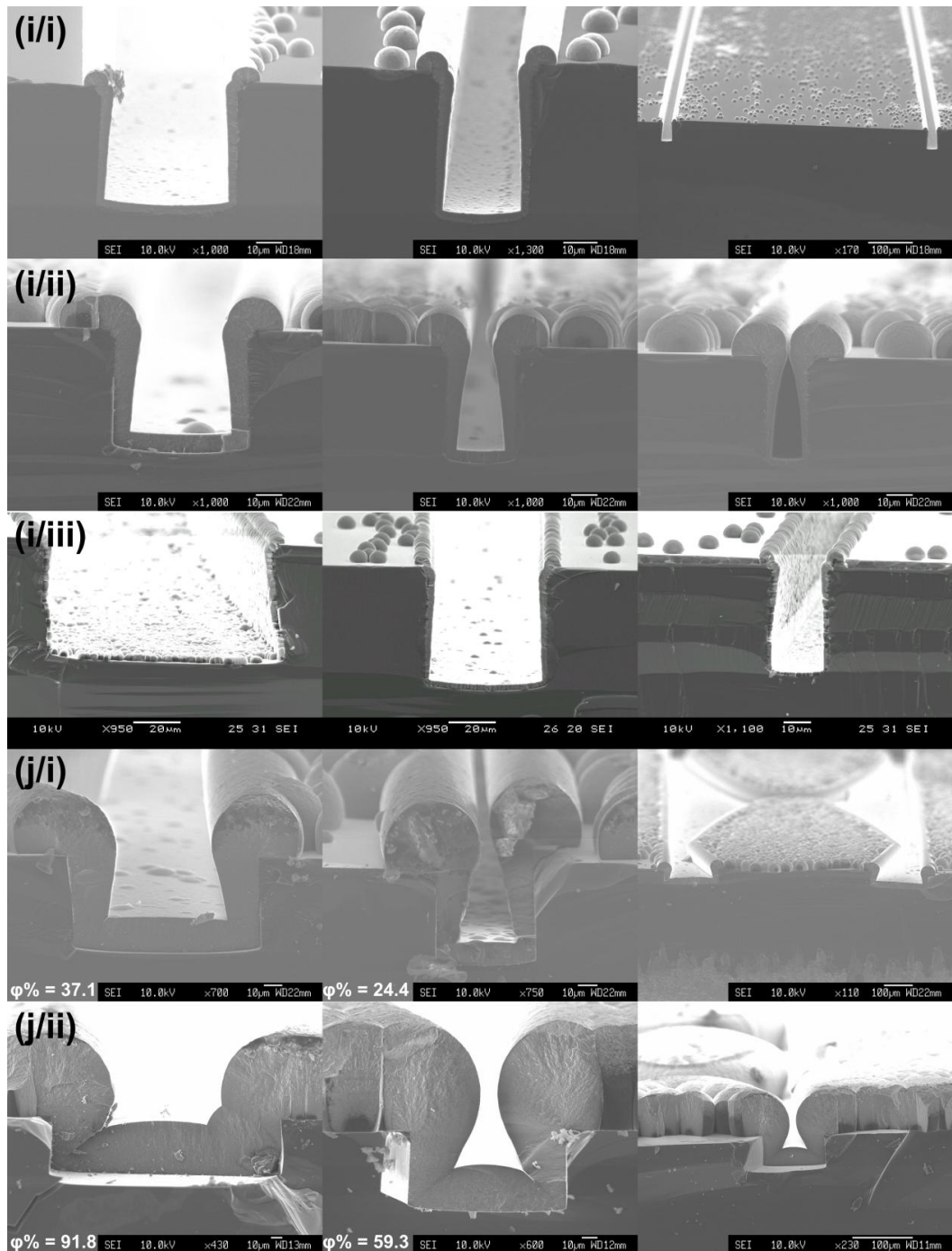


Figure 61: Cross-sectional SEM images for group **i** and **j** samples at a range of aspect ratios. Deposition conditions are summarised in **Table 8**.

6.2.5 Comparison of Successful Selective Nucleation Methods

While the cross-sectional SEMs show the success of the preferential nucleation to a certain extent, comparison of the different seeding methods is possible by looking at the percentage filling ($\phi_{\%}$) of each sample for a range of aspect ratio structures. The measurements obtained from the SEM images for group **c** and **j** samples in **Figure 50** and **Figure 61** are displayed in **Table 9**.

Table 9: Measurements of the $\phi_{\%}$ from the SEMs for group **c** and **j** samples.

Sample	Selective Seeding	Aspect ratio (μm)	$\phi_{\%}$ (%)
c/i	H_2/N_2	0.27	42.5
	$t_{\text{removal}} = 30 \text{ min}$	0.45	38.4
	$t_{\text{growth}} = 18 \text{ h}$	0.94	29.5
c/ii	H_2/N_2	0.28	52.3
	$t_{\text{removal}} = 20 \text{ min}$	0.46	43.6
	$t_{\text{growth}} = 18 \text{ h}$	0.95	24.2
j/i	Self-assembly	0.53	37.1
	$t_{\text{growth}} = 18 \text{ h}$	0.96	24.4
j/ii	Self-assembly	0.25	91.8
	$t_{\text{growth}} = 36 \text{ h}$	0.51	59.3

For $t_{\text{growth}} = 18 \text{ h}$, the highest aspect-ratio structures a $\phi_{\%}$ of 20 – 30 % was achieved, while lower aspect-ratio areas achieving $\phi_{\%} \sim 40 \%$. The $\phi_{\%}$ as a function of a wide range of aspect-ratios is plotted in **Figure 62** to allow comparison between the selective and non-selective processes. An improvement in the $\phi_{\%}$ from sample **c/i** to sample **c/ii** is apparent related to the decrease in the H_2/N_2 -plasma resist-removal time. That a 10 minute decrease in the plasma exposure time noticeably increases the filling of the mould highlights the sensitivity of this method. There is little difference in the percentage filling when comparing samples **c/ii** and **j/i**, although it appears that sample **c/ii** is slightly better. This is due to the cusping problem which tends to be more of an issue for the self-assembly method, as seen in the SEM cross-sections of these samples showing more overgrowth on the corners. As expected, the highest $\phi_{\%}$ were achieved for sample **j/ii** which had $t_{\text{growth}} = 36 \text{ h}$. For the lowest aspect-ratio structure measured a filling of $\sim 90 \%$ was achieved and this process could be used to produce a working CRL with a minimum trench thickness of $30 \mu\text{m}$ for testing at DLS.

A direct comparison of $\phi_{\%}$ for group **c** and **j** samples cannot be made with the samples grown at different $\chi_0(N_2)$ ($t_{\text{growth}} = 10$ h) due to the different t_{growth} . However **Figure 62** indicates that the selective methods are more successful because the trend in $\phi_{\%}$ for group **c** and **j** samples is increased more significantly than the expected trend from the non-selective samples. The cross-sectional SEM images are evidence that the selective seeding method is enhancing the deposition process over non-selective seeding however further work will need to address the cusping growth on the corners of the mould.

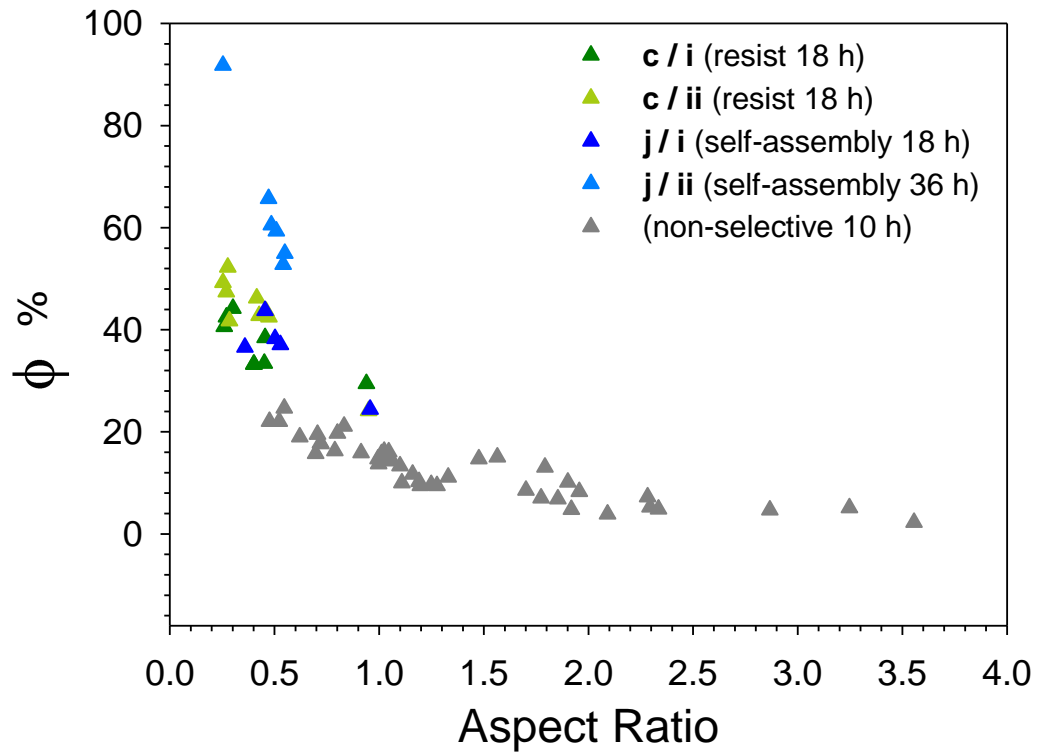


Figure 62: $\phi_{\%}$ as a function of aspect ratio for the long deposition samples (group **c** and **j**). The grey triangles represent the data from the non-selective samples grown at $\chi_0(N_2) = 0.19 - 1.83$ % ($t_{\text{growth}} = 10$ h).

7. Future and Outlook

It is believed that the limit has been reached with the variety of H_2/N_2 plasma conditions (group **b** and **c** samples) used for the resist removal and improving the filling percentage will require application of the resist to the lens sidewalls as well as the top surface. In the self-assembly method, only the acetone strip method has been used to remove the resist layer. To investigate this and extend the range of parameters used, the next stage will be to try an O_2 plasma at higher power to remove the resist/seed layer. This would indicate if this method was able to compete with either the H_2/N_2 or acetone resist-removal techniques. Since the self-assembly method produced such a uniform seed layer, three lens samples were seeded by this method and resist removal carried out at MNTC using higher O_2 plasma powers. The results from these tests have not yet been analysed.

For the oxide-coated method three kinoform lens samples were seeded using the self-assembly process and subsequently had a thin/non-continuous layer of NCD deposited under standard conditions for $t = 1.5, 3$ and 6 minutes. These have been given to MNTC to have the oxide layer removed in HF acid, before they are returned to the University of Bristol for further NCD deposition. A thinner initial diamond layer is believed to improve this method by allowing an isotropic etch of the oxide layer and complete removal of the diamond from the top and sidewall surfaces.

In all the samples that use resist on the top surface, there is always overgrowth of diamond on the top corners after deposition. Preventing this problem will require application of a resist layer to the sidewalls of the mould as well as the top surface and so various viscosity resist solutions were spin coated onto bare silicon lens moulds. The viscosity and quantity of the resist solution is crucial in applying a thin layer across the entire three-dimensional substrate and it is yet unclear whether spin coating will cause resist to enter the high aspect-ratio trenches or fill them completely. If the resist layer has covered the trench uniformly then directional reactive ion etching will be carried out to remove it from the bottom surface, leaving a resist layer on the top and sidewall surfaces. The selective nucleation methods developed for samples **c/ii** and **j/ii** will be repeated before the NCD deposition to give improved filling of the moulds.

An alternative method that will also be investigated is to polish the NCD off the top surface after a long deposition before returning the sample back in the reactor for further growth without the cusping problem blocking growth of the recessed areas.

Another preferential nucleation method that will be tested uses a hard-mask stencil to pattern the ES seeding onto only the recessed areas of the mould. The stencil is fabricated

by etching completely through a 350 μm thick Si wafer, in a design matching the top surface of the lens mould. This mask would be aligned with the top surface of the silicon mould prior to ES seeding. It would then either be removed before deposition in the MWCVD reactor, or removed after an initial growth period. If the mask is present during the initial deposition stages it should prevent any diamond depositing on the top surface. If required the sample could be re-nucleated to allow deposition on the top-surface once the recessed areas were filled.

As mentioned in **Section 6**, the samples grown at a range of $\chi_0(\text{N}_2)$ will be analysed at the DLS using SAXS, to see which $\chi_0(\text{N}_2)$ is most successful at reducing x-ray scattering, and NEXAFS to obtain quantitative concentrations for sp^2 - and sp^3 -bonded carbon for comparison with the Raman analysis.

8. Conclusions

Twelve lens samples were grown for $t_{\text{growth}} = 10$ h at a range of $\chi_0(\text{N}_2)$ (0.19 – 1.83 %) and analysed using Raman spectroscopy ($\lambda_{\text{exc}} = 325$ and 514 nm) and cross-sectional scanning electron microscopy. The Raman spectra were used to determine the morphology of the deposited diamond and showed that by increasing $\chi_0(\text{N}_2)$, the degree of sp^3 -bonded carbon decreased, while the sp^2 -bonded carbon increased. This is a result of the diamond crystallite size decreasing which increases the grain boundary surface area resulting in less sp^3 -bonded carbon present. These samples will be tested at DLS using both SAXS and NEXAFS to determine which morphology has the lowest x-ray scattering and to obtain a quantitative value of the sp^3 - to sp^2 -bonded carbon ratio for comparison with the Raman analysis respectively.

The SEM cross-sections were used to analyse the effect of $\chi_0(\text{N}_2)$ on the filling of the lens moulds. In order to improve a focusing capability of the NCD lenses, the film thickness at the bottom of the trench regions needs to be increased. It was found that changing $\chi_0(\text{N}_2)$ did not affect the filling of lens structure and that the film thickness in the recessed areas was dependent on aspect ratio only, where in high aspect-ratio structures the cusping on the top corners prevents diamond deposition into the lower regions.

In order to enable a thicker NCD film in the recessed regions, a range of selective seeding methods were trialled in order to suppress growth on the top surface to allow more NCD deposition onto the bottom surface. Three different methods were investigated: using a polymer resist coating on the top surface of the lens moulds, an oxide coating on certain regions of the lens moulds, and a self-assembly nucleation method. Successful preferential nucleation of the lower surface was achieved by each method, and long depositions ($t_{\text{growth}} \geq 18$ h) were carried out on the polymer resist coated lens samples and the self-assembly samples. Both methods were able to achieve $\phi_{\%} = 20 - 30$ % in the high aspect ratio samples, with higher values for the lower aspect ratios. The self-assembly method was more effective at removing the nucleation layer from the top surface and after 18 h was still not continuous on the top surface. A lens sample grown using the self-assembly method is being prepared for testing at DLS in order to see if a focal width of < 400 nm is achieved.

Each of the selective seeding techniques will be researched further in order to determine the most successful method for enabling a lens mould filling of > 50 μm .

References

- [1] M. D. Mills, *Third Generation Hard X-ray Synchrotron Radiation Sources*, John Wiley & Sons, Inc., New York, **2002**.
- [2] Röntgen, *American Journal of Roentgenology*. **1913**, 1, 325-325.
- [3] C. G. Schroer, O. Kurapova, J. Patommel, P. Boye, J. Feldkamp, B. Lengeler, M. Burghammer, C. Riekel, L. Vincze, A. van der Hart, M. Kuchler, *Applied Physics Letters*. **2005**, 87, 124103 1-3.
- [4] B. Nöhammer, C. David, H. Rothuizen, J. Hoszowska, A. Simionovici, *Microelectronic Engineering*. **2003**, 67-8, 453-460.
- [5] O. Hignette, G. Rostaing, P. Cloetens, A. Rommeveaux, W. Ludwig, A. Freund, *Conference on X-ray Micro- and Nano- Focusing - Applications and Techniques II*. **2001**, 4499, 105-116.
- [6] O. Hignette, P. Cloetens, G. Rostaing, P. Bernard, C. Morawe, *Review of Scientific Instruments*. **2005**, 76, 063709 1-5.
- [7] W. Yun, B. Lai, Z. Cai, J. Maser, D. Legnini, E. Gluskin, Z. Chen, A. A. Krasnoperova, Y. Vladimirovsky, F. Cerrina, E. Di Fabrizio, M. Gentili, *Review of Scientific Instruments*. **1999**, 70, 2238-2241.
- [8] H. Mimura, S. Matsuyama, H. Yumoto, H. Hara, K. Yamamura, Y. Sano, M. Shibahara, K. End, Y. Mori, Y. Nishino, K. Tamasaku, M. Yabashi, T. Ishikawa, K. Yamauchi, *Japanese Journal of Applied Physics Part 2-Letters & Express Letters*. **2005**, 44, 539-542.
- [9] S. Gorelick, J. Vila-Comamala, V. A. Guzenko, R. Barrett, M. Salome, C. David, *Journal of Synchrotron Radiation*. **2011**, 18, 442-446.
- [10] A. Stein, K. Evans-Lutterodt, A. Taylor, *Kinoform Lenses - Towards Nanometre Resolution*, SPIE Optics East, Boston, **2005**.
- [11] A. Sakdinawat, D. Attwood, *Nature Photonics*. **2010**, 4, 840-848.
- [12] K. Evans-Lutterodt, J. M. Ablett, A. Stein, C. C. Kao, D. M. Tennant, F. Klemens, A. Taylor, C. Jacobsen, P. L. Gammel, H. Huggins, S. Ustin, G. Bogart, L. Ocola, *Optics Express*. **2003**, 11, 919-926.
- [13] B. Lengeler, C. G. Schroer, M. Richwin, J. Tümmeler, M. Drakopoulos, A. Snigirev, I. Snigireva, *Applied Physics Letters*. **1999**, 74, 3924-3926.
- [14] A. Snigirev, V. Kohn, I. Snigireva, B. Lengeler, *Nature*. **1996**, 384, 49-51.
- [15] M. Young, *Optics and lasers*, Springer - Verlag, New York, **2000**.
- [16] B. X. Yang, *Nuclear Instruments & Methods in Physics Research Section A*. **1993**, 328, 578-587.
- [17] A. M. Zaitsev, *Optical Properties of Diamond*, Springer, Berlin, **2001**.
- [18] P. W. May, *Philosophical Transactions of the Royal Society of London Series A-Mathematical Physical and Engineering Sciences*. **2000**, 358, 473-495.
- [19] J. Lutz, H. Schlangenotto, U. Scheuermann, R. De Doncker, *Semiconductor Power Devices*, Springer, Heidelberg, **2011**.
- [20] E. P. Wagner, R. A. Butera, D. H. Waldeck, *Chemistry Manual 1440-Structural Characterisation of Graphite*, **2011**.
- [21] F. P. Bundy, *Journal of Geophysical Research*. **1980**, 85, 6930-6936.
- [22] H. Moissan, *The Electric Furnace*, General Books LLC, New York, **2009**.
- [23] P. W. May *Endeavour*. **1995**, 19, 101-106.
- [24] W. G. Eversole, *Synthesis of Diamond*, United States Patent Office, **1962 (filed 23 July 1958)**, Patent No. 3030188.
- [25] J. C. Angus, H. A. Will, W. S. Stanko, *Journal of Applied Physics*. **1968**, 39, 2915-2922.
- [26] D. J. Pofel, N. C. Gardner, J. C. Angus, *Journal of Applied Physics*. **1973**, 44, 1428-1434.

- [27] B. V. Deryagin, B. V. Spitsyn, L. L. Builov, A. A. Klochov, A. E. Gorodetski, A. V. Smol'yanimov, *Dokl. Akad. Nauk.* **1976**, 231, 333.
- [28] S. Matsumoto, Y. Sato, M. Tsutsumi, N. Setaka, *Journal of Materials Science.* **1982**, 17, 3106-3112.
- [29] S. Matsumoto, Y. Sato, M. Kamo, N. Setaka, *Japanese Journal of Applied Physics Part 2-Letters.* **1982**, 21, 183-185.
- [30] M. Kamo, Y. Sato, S. Matsumoto, N. Setaka, *Journal of Crystal Growth.* **1983**, 62, 642-644.
- [31] Y. Saito, S. Matsuda, S. Nogita, *Journal of Materials Science Letters.* **1986**, 5, 565-568.
- [32] R. S. Balmer, J. R. Brandon, S. L. Clewes, H. K. Dhillon, J. M. Dodson, I. Friel, P. N. Inglis, T. D. Madgwick, M. L. Markham, T. P. Mollart, N. Perkins, G. A. Scarsbrook, D. J. Twitchen, A. J. Whitehead, J. J. Wilman, S. M. Woollard, *Journal of Physics-Condensed Matter.* **2009**, 21, 1-23.
- [33] M. N. R. Ashfold, P. W. May, C. A. Rego, N. M. Everitt, *Chemical Society Reviews.* **1994**, 23, 21-30.
- [34] S. W. Reeve, W. A. Weimer, F. M. Cerio, *Journal of Applied Physics.* **1993**, 74, 7521-7530.
- [35] J. A. Smith, K. N. Rosser, H. Yagi, M. I. Wallace, P. W. May, M. N. R. Ashfold, *Diamond and Related Materials.* **2001**, 10, 370-375.
- [36] R. B. Wang, M. Sommer, F. W. Smith, *Journal of Crystal Growth.* **1992**, 119, 271-280.
- [37] P. W. Morrison, J. E. Cosgrove, P. R. Solomon, *Applied Physics Letters.* **1992**, 60, 565-567.
- [38] J. J. Gracio, Q. H. Fan, J. C. Madaleno, *Journal of Physics D-Applied Physics.* **2010**, 43.
- [39] P. W. May, N. L. Allan, M. N. R. Ashfold, J. C. Richley, Y. A. Mankelevich, *Diamond and Related Materials.* **2010**, 19, 389-396.
- [40] C. Hammond, *Introduction to Crystallography*, Oxford University Press, London, **1992**.
- [41] O. J. L. Fox, PhD Thesis, University of Bristol, **2011**.
- [42] S. T. Lee, Z. D. Lin, X. Jiang, *Materials Science & Engineering R-Reports.* **1999**, 25, 123-154.
- [43] K. Kobashi, K. Nishimura, Y. Kawate, T. Horiuchi, *Physical Review B.* **1988**, 38, 4067-4084.
- [44] J. Filik, *Spectroscopy Europe.* **2005**, 17, 10-17.
- [45] F. R. Kloss, M. Najam-Ul-Haq, M. Rainer, R. Gassner, G. Lepperdinger, C. W. Huck, G. Bonn, F. Klauser, X. Liu, N. Memmel, E. Bertel, J. A. Garrido, D. Steinmueller-Nethl, *Journal of Nanoscience and Nanotechnology.* **2007**, 7, 4581-4587.
- [46] O. A. Williams, M. Daenen, J. D'Haen, K. Haenen, J. Maes, V. V. Moshchalkov, M. Nesladek, D. M. Gruen, *Diamond and Related Materials.* **2006**, 15, 654-658.
- [47] P. W. May, M. N. R. Ashfold, Y. A. Mankelevich, *Journal of Applied Physics.* **2007**, 101, 053115 1-9.
- [48] A. F. Azevedo, M. R. Baldan, N. G. Ferreira, *International Journal of Electrochemistry.* **2011**, 2012, 1-16.
- [49] O. A. Williams, *Diamond and Related Materials.* **2011**, 20, 621-640.
- [50] W. Kulisch, C. Popov, *Physica Status Solidi a-Applications and Materials Science.* **2006**, 203, 203-219.
- [51] X. Xiao, J. Birrell, J. E. Gerbi, O. Auciello, J. A. Carlisle, *Journal of Applied Physics.* **2004**, 96, 2232-2239.
- [52] W. MullerSebert, E. Worner, F. Fuchs, C. Wild, P. Koidl, *Applied Physics Letters.* **1996**, 68, 759-760.
- [53] R. S. Sussmann, *CVD diamond for electronic devices and sensors*, John Wiley & Sons, Chichester, **2009**.

- [54] V. Aristov, M. Grigoriev, S. Kuznetsov, L. Shabelnikov, V. Yunkin, T. Weitkamp, C. Rau, I. Snigireva, A. Snigirev, M. Hoffmann, E. Voges, *Applied Physics Letters*. **2000**, 77, 4058-4060.
- [55] L. Alianelli, K. J. S. Sawhney, R. Barrett, I. Pape, A. Malik, M. C. Wilson, *Optics Express*. **2011**, 19, 11120-11127.
- [56] H. R. Beguiristain, J. T. Cremer, M. A. Piestrup, C. K. Gary, R. H. Pantell, *Optics Letters*. **2002**, 27, 778-780.
- [57] L. Alianelli, K. J. S. Sawhney, M. K. Tiwari, I. P. Dolbnya, R. Stevens, D. W. K. Jenkins, I. M. Loader, M. C. Wilson, A. Malik, *Journal of Synchrotron Radiation*. **2009**, 16, 325-329.
- [58] L. Alianelli, K. J. S. Sawhney, M. K. Tiwari, I. P. Dolbnya, R. Stevens, D. W. K. Jenkins, I. M. Loader, M. C. Wilson, A. Malik, *9th International Conference on X-Ray Microscopy*. **2009**.
- [59] B. Nöhammer, J. Hoszowska, A. Freund, A. Somogyi, A. Simionovici, C. David, *Journal De Physique Iv*. **2003**, 104, 223-226.
- [60] K. E. Spear, J. P. Dismukes, *Synthetic Diamond: Emerging CVD Science and Technology*, Wiley, New York, **1994**.
- [61] L. Alianelli, K. J. S. Sawhney, A. Malik, O. J. L. Fox, P. W. May, R. Stevens, I. M. Loader, M. C. Wilson, *Journal of Applied Physics*. **2010**, 108, 123107 1-4.
- [62] C. G. Schroer, M. Kuhlmann, U. T. Hunger, T. F. Gunzler, O. Kurapova, S. Feste, F. Frehse, B. Lengeler, M. Drakopoulos, A. Somogyi, A. S. Simionovici, A. Snigirev, I. Snigireva, C. Schug, W. H. Schröder, *Applied Physics Letters*. **2003**, 82, 1485-1487.
- [63] C. G. Schroer, B. Lengeler, *Physical Review Letters*. **2005**, 94, 054802 1-4.
- [64] R. Linares, P. Doering, *Diamond and Related Materials*. **1999**, 8, 909-915.
- [65] B. Nöhammer, J. Hoszowska, A. K. Freund, C. David, *Journal of Synchrotron Radiation*. **2003**, 10, 168-171.
- [66] O. L. J. Fox, J. O. P. Holloway, G. M. Fuge, P. W. May, M. N. R. Ashfold, *Diamond Electronics and Bioelectronics - Fundamentals to Applications III*. **2010**, 1203, 17-27.
- [67] S. M. Leeds, T. J. Davis, P. W. May, C. D. O. Pickard, M. N. R. Ashfold, *Diamond and Related Materials*. **1998**, 7, 233-237.
- [68] A. C. Ferrari, J. Robertson, *Philosophical Transactions of the Royal Society A-Mathematical Physical and Engineering Sciences*. **2004**, 362, 2477-2512.
- [69] C. D. Clark, C. B. Dickerson, *Journal of Physics-Condensed Matter*. **1992**, 4, 869-878.
- [70] J. Wagner, M. Ramsteiner, C. Wild, P. Koidl, *Physical Review B*. **1989**, 40, 1817-1824.
- [71] S. Praver, R. J. Nemanich, *Philosophical Transactions of the Royal Society of London Series A-Mathematical Physical and Engineering Sciences*. **2004**, 362, 2537-2565.
- [72] M. Wojdyr, *Journal of Applied Crystallography*. **2010**, 43, 1126-1128.
- [73] H. W. Kroto, *Molecular Rotation Spectra*, Dover Publications, Inc., New York, **1992**.
- [74] R. W. B. Pearse, A. G. Gaydon, *The identification of molecular spectra*, John Wiley & Sons, Inc., New York, **1976**.
- [75] J. Luque, D. R. Crosley, *Journal of Chemical Physics*. **1996**, 104, 2146-2155.
- [76] C. H. Su, C. Y. Chang, *Materials Transactions*. **2008**, 49, 1380-1384.
- [77] G. Hong, A. S. Holmes, M. E. Heaton, *Microsystem Technologies-Micro-and Nanosystems-Information Storage and Processing Systems*. **2004**, 10, 357-359.
- [78] S. B. Kim, H. Seo, Y. Kim, H. Jeon, J. Song, H. Soh, Y. C. Kim, *Journal of the Korean Physical Society*. **2002**, 41, 247-250.
- [79] S. K. Lee, J. H. Kim, M. G. Jeong, M. J. Song, D. S. Lim, *Nanotechnology*. **2010**, 21, 1-7.

Certification of ownership of the copyright in a typescript or manuscript

Dissertation presented as part of, and in accordance with, the requirements for the Final Degree of MSci at the University of Bristol, Faculty of Engineering.

I hereby assert that I own exclusive copyright in the item named below. I give permission to the University of Bristol Library to add this item to its stock and to make it available for consultation in the library, and for inter-library lending for use in another library. It may be copied in full or in part for any *bona fide* library or research worked, on the understanding that users are made aware of their obligations under copyright legislation, i.e. that no quotation and no information derived from it may be published without the author's prior consent.

Author	Sarah Rebecca Whittaker
Title	Fabrication of Low-Absorption Diamond Lenses for Focusing Hard X-rays at Synchrotron Sources
Date of Submission	08/05/2012

Signed: S. R. Whittaker

Full Name: Sarah Rebecca Whittaker

Date: 08/05/2012

This dissertation/thesis is the property of the University of Bristol Library and may only be used with due regard to the rights of the author. Bibliographical references may be noted, but no part may be copied for use or quotation in any published work without the prior permission of the author. In addition, due acknowledgement for any use must be made.